Final Report

STUDY OF MEDIUM-RESOLUTION RADIOMETRIC DATA FROM NIMBUS II

By: PAUL A. DAVIS

Prepared for:

NATIONAL AERONAUTICS AND SPACE ADMINISTRATION
GODDARD SPACE FLIGHT CENTER
GREENBELT, MARYLAND

CONTRACT NAS5-10365

STANFORD RESEARCH INSTITUTE

MENLO PARK, CALIFORNIA

S T A N F O R D   R E S E A R C H   I N S T I T U T E

M E N L O   P A R K   C A L I F O R N I A

November 1968

Final Report

STUDY OF MEDIUM-RESOLUTION RADIOMETRIC DATA FROM NIMBUS II

By: PAUL A. DAVIS

Prepared for:

NATIONAL AERONAUTICS AND SPACE ADMINISTRATION
GODDARD SPACE FLIGHT CENTER
GREENBELT, MARYLAND

CONTRACT NAS5-10365

SRI Project 6478

Approved: R. T. H. COLLIS, DIRECTOR
Aerophysics Laboratory

RAY L. LEADABRAND, EXECUTIVE DIRECTOR
Electronics and Radio Sciences

Copy No. 2

PRECEDING PAGE BLANK NOT FILMED.

ABSTRACT

Variations of medium-resolution radiometric data from Nimbus II are compared, on a local scale, with concurrent thermodynamic properties derived from conventional meteorological data. An infrared model for computing transmissions, radiances in particular spectral intervals, or total fluxes was completely revised and improved. Applications of the model to real data yield radiances that compare favorably with satellite data.

In contrast to previous computations with data from a variety of locations at a fixed time, computations from a series of observations at a fixed location showed a high correlation between total outgoing flux and total infrared cooling for all cloud conditions. However, the correlation between radiometric measurements and the computed outgoing flux and, especially, total cooling, deteriorated as the cloudiness increased. The vertical distribution of the infrared cooling in the tropical Pacific between 7°N and 20°N showed a pronounced maximum in the upper troposphere at 7°N. Maintenance of the upper tropospheric temperature distribution demands a supply of heat at high levels there, presumably by convection and the release of latent heat (and, possibly, by eddy heat transports).

Of the four infrared channels on Nimbus II, Channel 2 (10-11 microns) generally was best correlated with computed total fluxes. Therefore, some other spectral channel, such as ozone, might be more useful than the spectrally broad Channel 4 (5-30 microns). During periods of clear sky, 12-hour changes in the Channel 2 temperature relate to changes in shelter-height temperatures, but the correspondence is influenced by the magnitude of the temperature discontinuity at the surface and by the total precipitable water. Channel 1 (6.4-6.9 microns) was most useful in the tropics where the upper-tropospheric temperature is reasonably uniform; there Channel 1 varies inversely both with upper-level moisture

and high clouds. Channel 3 (14-16 microns) was most useful north of the tropics; its response varies inversely with the base-height of the tropopause in mid-latitudes and directly with the average stratospheric temperature in polar latitudes. Channel 5 (0.2-4 microns) solar reflectances displayed a gross relationship to the solar radiation reaching the surface. However, insolation measurements and the Channel 5 data indicate that empirical estimates of atmospheric absorption for cloudy or hazy skies need improvement prior to local application.

The air-sea heat exchange, when averaged in time and averaged zonally across the ocean, shows a direct relationship to the Channel 2 temperature and an inverse relationship to the Channel 5 reflectance. On the other hand, radiometric data must be related to circulation features before the local distribution of the air-sea heat exchange can be deduced.

CONTENTS

CONTENTS (continued)

ILLUSTRATIONS

ILLUSTRATIONS (continued)

ILLUSTRATIONS (continued)

PRECEDING PAGE BLANK NOT FILMED.

TABLES

PRECEDING PAGE BLANK NOT FILMED.

ACKNOWLEDGMENTS

Of the personnel from the Aerophysics Laboratory who participated and assisted in various phases of this research, the most significant contributors were John E. Alder and Hisao Shigeishi. Mr. Alder conducted much of the analysis of satellite and meteorological data; Mr. Shigeishi performed all of the programming required in the design, evaluation, and application of the extensive infrared computations.

Special thanks are extended to Dr. Taivo Laevastu and Capt. Paul M. Wolff, Officer-In-Charge, U.S. Fleet Numerical Weather Facility, Monterey, for their immediate cooperation in supplying printouts of the air-sea heat-exchange analyses used in this study. Dr. Ehrhard Raschke, formerly with the Goddard Space Flight Center, kindly forwarded (prior to publication) printouts of zonal averages and maps of the components of his heat-budget analysis from Nimbus II data. The National Space Science Data Center at Goddard Space Flight Center provided the basic Nimbus II data.

I INTRODUCTION AND SUMMARY

A. General

The primary objective of this research is to examine the relationship, on a local scale, of medium-resolution radiometric data from Nimbus II with thermodynamic properties derived from coincident standard meteorological observations. Studies conducted on a local scale make it possible to evaluate the significance and limitations of inferences drawn directly (and linearly) from large-scale statistical summaries of satellite data. Furthermore, it is logical to compare the presently available satellite data with local atmospheric states of particular interest before proceeding, out of necessity, to more sophisticated observational schemes with more difficult data-processing and evaluation problems. A variety of comparisons are made in order to determine which potential relationships should be studied more carefully from much larger data samples.

Nimbus II was the first polar-orbiting sun-synchronous meteorological satellite to provide multichannel medium-resolution infrared data in addition to cloud photographs. Thus the earth-viewing characteristics were improved and the earth coverage was more regular than for similar data collected during the earlier TIROS series of satellites. Emphasis in this study of Nimbus II data with concurrent computations of infrared cooling is placed on the temporal variations occurring at fixed points. This was not possible to do in an orderly fashion with the previous TIROS data.

The biggest difficulty encountered during the analyses was the objective specification of local cloud cover. Although the general patterns of cloud cover usually are depicted by HRIR (nighttime) and AVCS (daytime) data, it was necessary to utilize surface observations and upper-air data to the fullest extent.

Most of the important results of the study are summarized below under four major headings. Analyses were restricted to data from the second half of June, 1966.

B. Transmission and Flux Model

The very extensive revisions of our infrared model have resulted in improved computations of radiances and fluxes. In addition to treating a semitransparent cloud layer, the model now will handle temperature discontinuities at the lower boundary. The satisfactory results of the applications indicate that with normal upper-air data it is feasible to conduct extensive computations over large areas and to maintain a link with satellite radiometric data. Applications of the model in conjunction with satellite MRIR data should include objective inferences on clouds and tropospheric structure.

C. Analysis Over Pacific

In contrast to previous studies of data from many localities at a fixed time, the time variations at fixed points showed that there was a very high correlation between computed outgoing long-wave flux at 100 mb and the total infrared cooling below that altitude, regardless of the cloud cover. On the other hand, at a fixed locality, no significant generation or destruction of total potential energy by infrared processes was found. Between 7°N and 20°N in the tropics, the cooling maximum below 500 mb occurred near 20°N as expected. However, the most pronounced cooling maximum occurred between 500 mb and 100 mb at 7°N. In order to maintain the meridional temperature gradient, considerable heat must be supplied to the upper troposphere near 7°N; convection and the release of latent heat apparently are important, but eddy heat transports could play a role also.

The Nimbus II Channel 2 (10-11 microns) temperature was closely related with the outgoing long-wave flux (inversely related with cloudiness) and, to a lesser extent, the total cooling. In the absence of significant cloudiness, Channel 2 also was correlated with the net radiation at the surface. With significant cloudiness, Channel 2 was correlated positively with the cooling in the lower troposphere and negatively with the cooling in the upper troposphere; the highest correlation did not occur between Channel 2 and cooling above the cloud top. Since Channel 4 (5-30 microns) did not provide additional information, it would have best been replaced with an ozone channel.

In the tropics, where the temperature distribution of the upper troposphere was reasonably uniform, the average Channel 1 (6.4-6.9 microns) temperature varied inversely with the average upper-level precipitable water. Since the occurrence of high clouds in the region varied meridionally with the high-level moisture, the inverse relationship between Channel 1 and the upper-level moisture was enhanced.

D. Analysis Over United States

With the aid of insolation measurements at the surface by the U.S. Solar Radiation Network, it was possible to utilize Channel 5 (0.2-4 microns) reflectance data to infer the atmospheric solar absorptance in conjunction with the transmittance. It appeared that low-level haze may be an important absorbent. It may be possible to obtain useful estimates of transmittance from reflectance data, and to infer the amount of solar radiation reaching the surface. Furthermore, results indicated that with an extended analysis it should be possible to formulate a useful empirical model for solar absorption as a function of the cloudiness on the basis of satellite and surface measurements. Present empirical models appear to be inadequate.

In conjunction with estimates of the available solar energy at the surface, observations of the diurnal range of surface temperature should improve estimates of latent-plus-sensible-heat exchange over land. Twice-daily Channel 2 temperatures in clear areas were related to the diurnal change, but the relationship was affected by temperature discontinuities at the surface and by the total precipitable water. Variations in cirrus cloudiness, which are not always detected, have a pronounced effect on the Channel 2 temperature range.

The response characteristics of Channel 3 (14-16 microns) on Nimbus II were such that they provided a measure of the spatial variation in the height of the tropopause base, in addition to responding to the mean temperature of the stratosphere. Because of the importance of information relating to the tropopause base, especially where spatial variations are rapid, radiometric measurements that respond to atmospheric contributions from this critical region should be obtained in the future.

For small data samples over the United States, the Channel 1 temperature was related only in a general way to the upper-tropospheric precipitable water when the observations with cirrus (the coldest Channel 1 temperatures) were removed.

E. Air-Sea Heat Exchange

On a local scale the Channel 2 temperature and the Channel 5 reflectance must be combined with a synoptic scale analysis before they can be used to identify the relative distribution of the latent-plus-sensible-heat exchange at the sea surface. Once a distribution is identified, movements and persistence of the system can be followed with MRIR data.

The time-averaged (15-day) distribution of heat exchange still is dependent on features of the general circulation not provided by the MRIR data alone, but if the time averages are also averaged zonally, then a direct relationship emerges between the latent-plus-sensible-heat exchange and the corresponding averages of Channel 2 and Channel 5 data.

II DATA

A. Medium-Resolution Radiometric Measurements

The five-channel medium-resolution radiometer aboard Nimbus II has been described thoroughly[1]*; the nominal spectral limits of the channels are reviewed in Table I for quick reference.

Table I

NOMINAL DESCRIPTORS OF FIVE-CHANNEL RADIOMETER ON NIMBUS II

Channel	Wavelength Interval (μ)	Nature
1	6.4 - 6.9	Water-vapor absorption
2	10 - 11	Infrared window
3	14 - 16	Carbon dioxide absorption
4	5 - 30	Total infrared radiance
5	0.2 - 4.0	Solar reflectance

The diameter of the area viewed by the medium-resolution radiometer at the subpoint of the satellite is about 30 nmi. During the scans of any orbital swath the viewed area increases as the nadir angle increases. As a rough guide for analysis, data samples from areas up to five times larger than the minimum might still be considered to be equally representative of background conditions.

Essential characteristics of the radiometric view include the following:

H = Height of satellite (1140 km)

R = Radius of earth (6371 km)

---

* References are listed at the end of the report.

ψ = Half-angle of radiometric field of view (1.3 deg)

α = Nadir angle to viewed spot

β = Zenith angle

γ = Geocentric angle between viewed spot and subpoint = $\beta - \alpha$

The viewed area on the spherical earth can be expressed as

$$A = 2R^2 \int_{\cos \gamma_{max}}^{\cos \gamma_{min}} \lambda \, d(\cos \gamma) \qquad (1)$$

where λ (a function of γ) is one-half of the symmetrical lateral range of the viewed area. At the subpoint, where λ is not a function of γ,

$$A_o = 2\pi R^2 \, (1 - \cos \gamma_\psi) \qquad (2)$$

A good approximation to Eq. (1) over most of the pertinent view angles is achieved by treating the viewed area as a polar area on a sphere, with an effective polar angle, $\bar{\theta}$, defined as

$$\bar{\theta} = 1/2 \left\{ \sin^{-1} \left(\frac{\sin \bar{\gamma} \tan \psi}{\sin \alpha} \right) + \gamma_{max} - \gamma_{min} \right\} \qquad (3)$$

where $\bar{\gamma}$ is midway between γ_{max} and γ_{min} and α is everywhere greater than ψ. With this approximation the ratio of the viewed area at any central nadir angle to the viewed area at the subpoint is given by

$$\frac{A}{A_o} \approx \frac{1 - \cos \bar{\theta}}{1 - \cos \gamma_\psi} = \left[\frac{\sin(\bar{\theta}/2)}{\sin(\gamma_\psi/2} \right]^2 \quad . \qquad (4)$$

Results from Eq. (4) are plotted in Fig. 1; the ratio reaches a magnitude of five by nadir angle 45°, the acceptable limit for this study.

Figure 2 shows the distribution of the satellite nadir angle and the solar zenith angle about the sub-satellite track as the orbital swath progresses from the equator to about 60°N latitude at about the time of the summer solstice. Figure 3 shows the corresponding distribution of the scattering angle. It is apparent from Fig. 3 that the anisotropy of the solar radiation reflected from a uniform surface does not play a significant role in the relative distribution of the solar

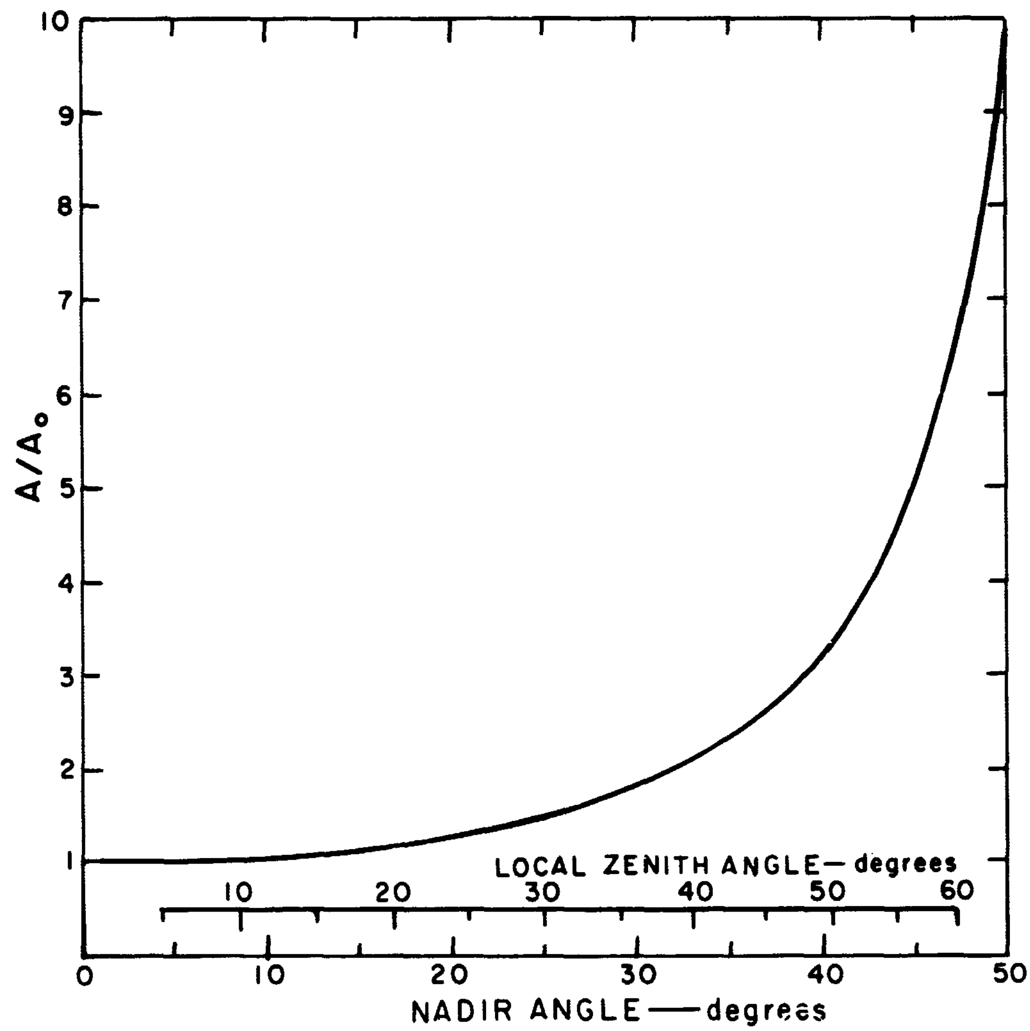

FIG. 1 RATIO OF AREA (A) VIEWED AT ARBITRARY CENTRAL NADIR ANGLE TO AREA (A_o) VIEWED AT SUBPOINT FOR NIMBUS II MEDIUM-RESOLUTION RADIOMETER

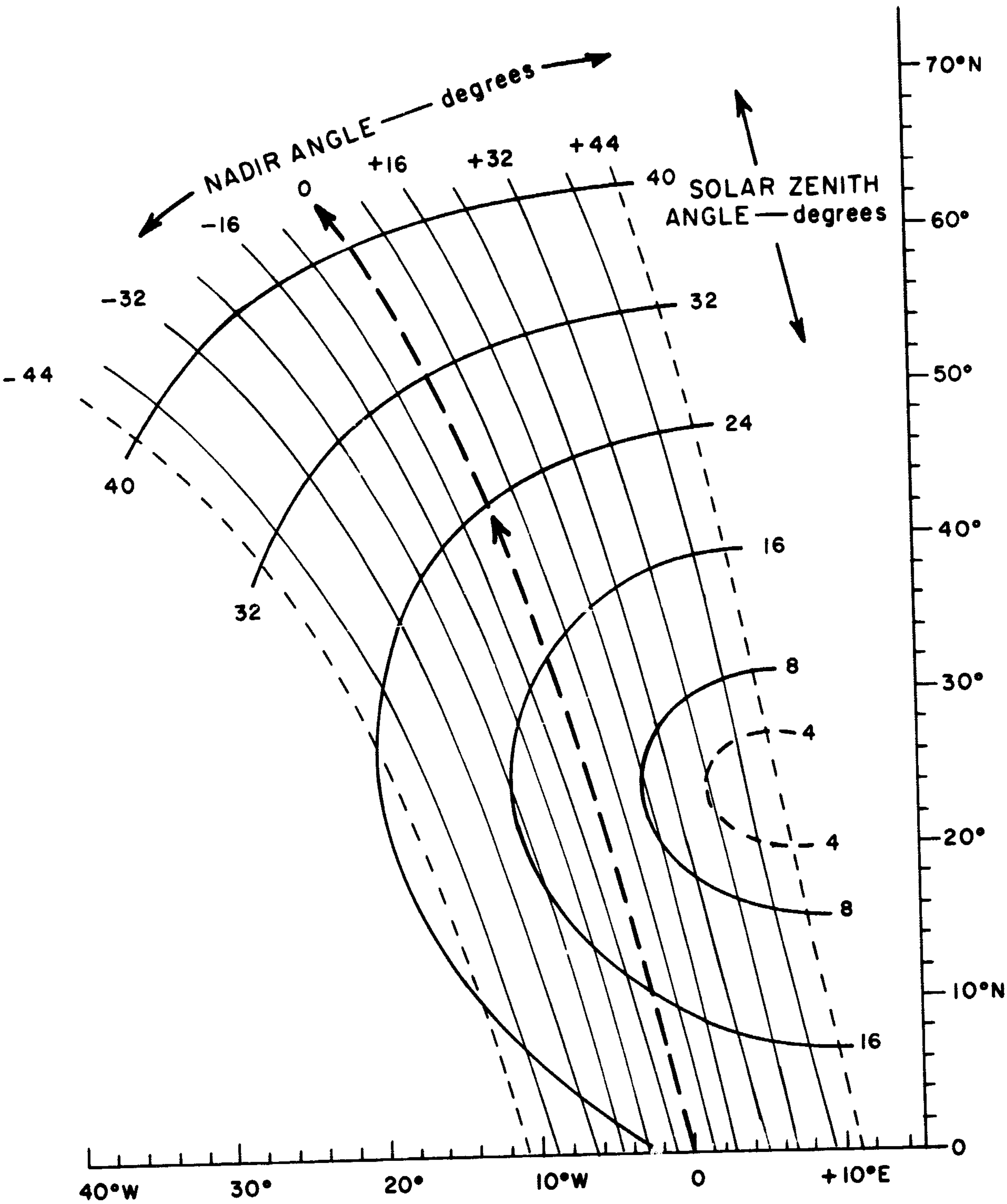

FIG. 2 DISTRIBUTION OF NADIR ANGLE AND SOLAR ZENITH ANGLE, NIMBUS II, 26 JUNE 1966

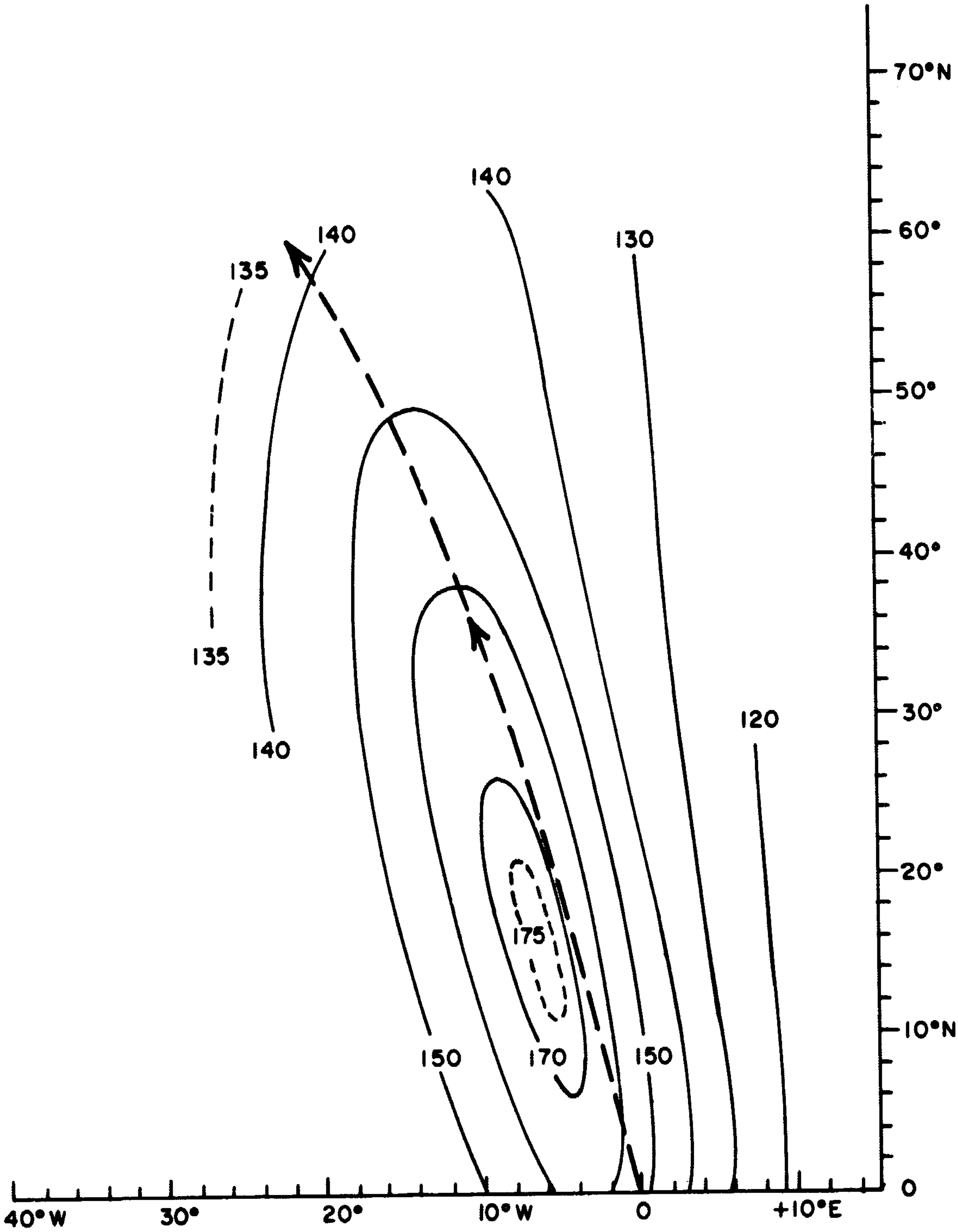

FIG. 3 DISTRIBUTION OF SCATTERING ANGLE (degrees), NIMBUS II, 26 JUNE 1966

reflectances. However, in order to arrive at a proper estimate of the albedo it is necessary to take into account the scattering angles that were not encountered in the viewing sample. Furthermore, anisotropy does arise from fields of scattered clouds within the viewed areas.

Measurements in the infrared channels are influenced by the anisotropy (limb darkening) of the emerging radiance between our nadir angle limits of ±45 degrees. The degree of limb darkening is dependent on the amount of absorption and the temperature distribution. The limb darkening for Channel 3 is almost negligible out to 45 degrees because part of the response (in low and moderate latitudes) comes from below the tropopause and part above. Thus, as the slant path is increased and the contributing portion of the atmosphere is raised, little change in the effective temperature results. Channel 1, on the other hand, receives contributions from the upper troposphere so that as the slant path (nadir angle) increases, the effective temperature is lowered. Channel 4 and, to a lesser extent, Channel 2 also respond with lower effective temperatures as the nadir angle increases; for these channels the amount of limb darkening over a uniform background is largest for a deep, moist atmosphere, whereas for a mid-tropospheric undercast the limb darkening is negligible. Normally, the window channel (Channel 2 of Nimbus II) would not display a "darkening" of more than two degrees out to a 45-degree nadir angle, but scattered clouds (especially cumulus) greatly increase the darkening by effectively screening out the warmer surface as the nadir angle increases.

The normalization of radiometric data from an arbitrary angle to eliminate the effect of limb darkening is a difficult task for real atmospheric conditions. The nonhomogeneous background conditions are difficult to treat theoretically, and statistical summaries of large quantities of satellite data do not necessarily provide the best estimate of limb variation for the viewed local state. Consequently, small portions of several Nimbus II swaths over the Pacific Ocean during June were selected for further study on the basis of apparent uniformity in cloudiness over nadir angles between 0 and 45 degrees. Several successive scan lines for each channel were plotted and examined for the average limb variation. For significant amounts of high clouds it was not possible to find a uniform undercast, and no limb curves could be determined empirically for that condition. Apparently, the cirrus cloudiness is too irregular in concentration and transparency to provide a definable background for the 45-degree range in nadir angles; what is needed is a variety of nadir-angle views of the same local spot.

For uniform undercast conditions with cloud tops at or below the midtroposphere, a condition common to the Gulf of Alaska, it was noted that the limb darkening both for Channel 2 and Channel 4 was small enough to be neglected (out to 45-degree nadir angle) in comparison to other uncertainties. However, the observed limb darkening for Channel 1 was very similar to the limb darkening that is theoretically predictable for Channel 1 in clear skies. Thus, in the absence of significant high cloudiness, a single limb-darkening curve can be associated with Channel 1. The curve derived empirically for Channel 1 is illustrated in Fig. 4.

Scattered clouds with considerable vertical extent can produce the largest limb darkening on Channel 2 measurements. Examples of this effect were derived from scan lines over scattered cumulus clouds south of Wake Island; results for Channels 2 and 4 are illustrated in Fig. 4. These curves were used to derive limb corrections when the Channel 2 or Channel 4 data were known to come from views of similar cloud conditions.

B. Processed Satellite Data Records

The limited scope of this investigation dictated that only a small fraction of available satellite data be selected for study. Attention was confined to satellite data within the 15-day period extending from 16 June to 30 June 1966.

Inasmuch as radiosonde observations normally are obtained twice daily (at 12-hour intervals) there were only two meridional strips that contained upper-air data coincident, or nearly coincident, with Nimbus II overflights. One of these strips is approximately the 180-degree longitude in the Pacific. Therefore, for the last half of June multi-

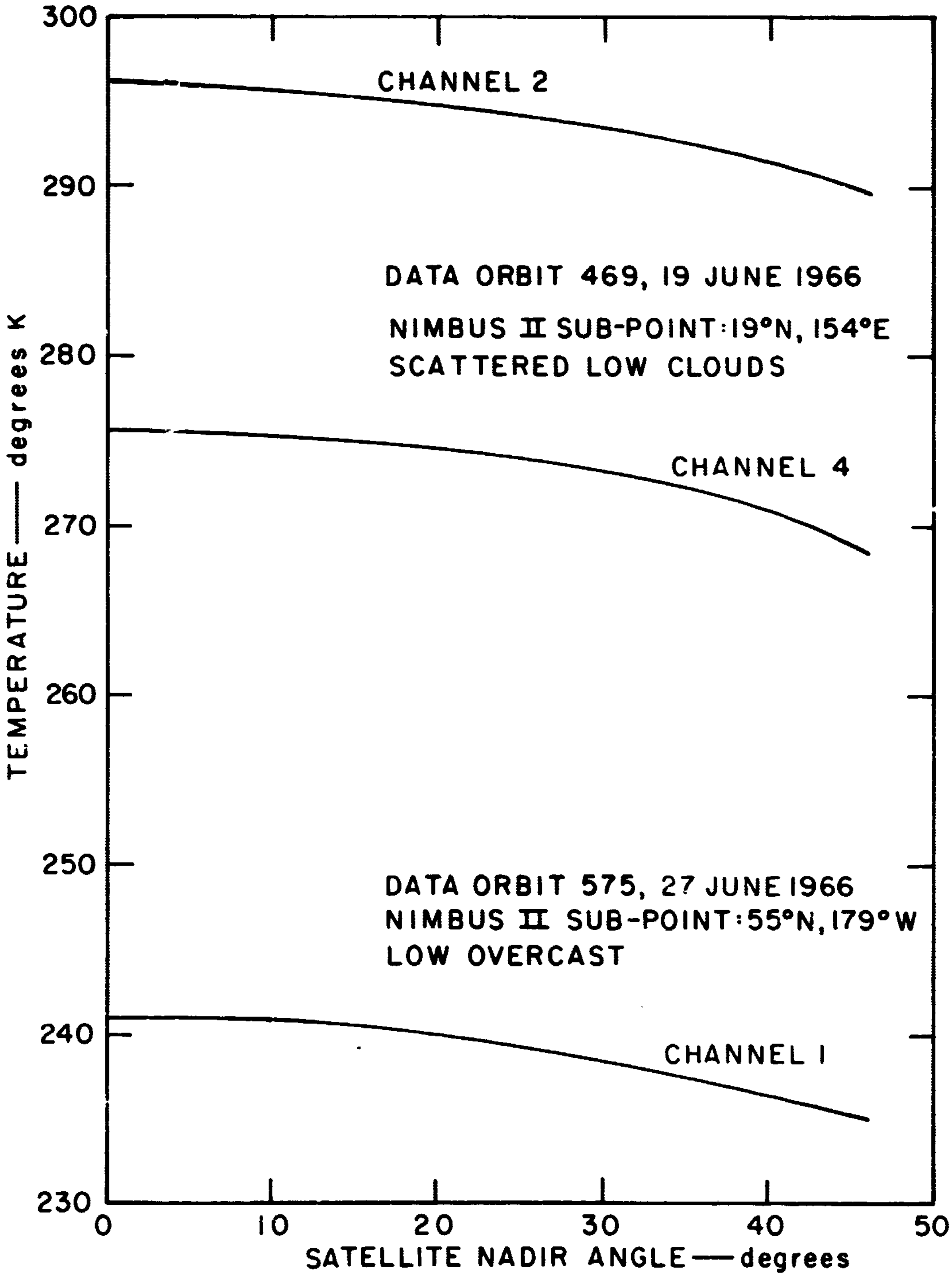

FIG. 4 OBSERVED NADIR-ANGLE VARIATIONS IN RADIOMETRIC RESPONSE FOR SELECT BOUNDARY CONDITIONS

channel listings of the MRIR data were obtained in short segments selected to provide daily coverage over about six rawinsonde stations. A number of stations in the United States obtain rawinsonde measurements every 6 hours; those stations, located near 95°W longitude, provided upper-air data nearly coincident with Nimbus II passes over the area. Therefore, for two days in June, grid print maps for each channel on pertinent Nimbus II passes were obtained instead of the voluminous data listings. Other radiometric data orders included two days of composite grid print mappings of Channel 1 and Channel 5 (daytime only) over the eastern Pacific and 5-day and 15-day averages* of radiative fluxes derived from the Nimbus II radiometric data over the Atlantic and Pacific Oceans. The latter data[2] included corrections for the average limb variations in the data, thereby enabling the generation of fluxes from measurements at specific angles.

In conjunction with the 15 days of partial listings of radiometric data over selected Pacific stations, near midnight, concurrent film strips of HRIR data were obtained to provide assistance in specifying local cloudiness. Film negatives of pertinent AVCS cloud photographs were obtained with the daytime radiometric data over the United States; subsequently, positive prints were assembled into mosaics.

C. Conventional Meteorological Data

For the Pacific-station atmospheric soundings taken concurrently with Nimbus II passes, the prime upper-air data source was punched cards (Card Deck 645, National Weather Records Center, Asheville, North Carolina), but microfiche records of the data also were checked to determine moist-layer boundaries. Hemispheric surface charts and microfiche records of surface observations were used to define surface conditions, including sea-surface temperatures, and local cloudiness. Fifteen-day average sea-level isobaric charts also were obtained for the hemisphere.

---

* Courtesy of Dr. E. Raschke at Goddard Space Flight Center.

For the U.S. stations that provided soundings with the Nimbus II passes, upper-air data were taken from teletype records and supplemented with microfiche records of soundings taken 6 hours earlier and 6 hours later. Surface data were taken from 3-hourly synoptic charts. In addition, detailed distributions of maximum and minimum temperatures were derived from the National Climatological Summaries.*

D. Other Data

Copies* of hemispheric analyses by the U.S. Fleet Numerical Weather Facility, Monterey, California, of the sensible-plus-latent heat exchange and of the total heat exchange over the ocean surfaces were obtained for each day during the second half of June. Fifteen-day average charts of the heat exchanges were obtained also. Emphasis was given to the sensible-plus-latent-heat exchanges because they were computed and analyzed independently of cloud or satellite data.

Finally, listings of hourly and daily totals of insolation measured at U.S. stations in June were obtained from records of the U.S. Solar Radiation Network. Hourly totals of incoming solar fluxes at the surface were extracted at pertinent stations for the hour centered at the time of the appropriate Nimbus II pass.

---

* Personal communication with Dr. Taivo Laevastu and Capt. Paul M. Wolff, Officer in Charge.

III INFRARED TRANSMISSION AND FLUX MODEL

A. General

In order to study radiometric data and to relate atmospheric infrared characteristics to energetics, it is necessary to have an efficient, reliable program for computing total infrared fluxes and flux divergences directly from actual observed upper-air data for clear or cloudy skies. The procedure must be reproducible and practicable for routine application yet flexible enough to allow adaptations to new data or revised limits. Input must include the "bulk" parameters of reflectance and transmittance for clouds; output must yield the flux over the entire infrared spectrum, integrated over all angles, as well as an optional output for particular spectral intervals for view angles. Results should be compatible with experimental data, including medium-resolution radiometric data from satellites.

Relative merits of different flux programs are difficult to assess unless comparisons are made with reliable experimental data. Some recent evaluations[4,5] have shown that for idealized profiles small differences in total fluxes at particular levels were found. However, in some situations the small differences are important, and if improvements are desired it will be necessary to evaluate specific techniques (such as the method of angular integration) in isolation from other factors. More critical is the possibility that even when total fluxes are in general agreement there may be significant differences in particular spectral intervals. Since a link with medium-resolution satellite data is desired here and in future general-circulation studies, satisfactory results must be obtained in all spectral intervals. When interest is centered on spectral intervals narrower than about 5 cm^{-1}, then it is advisable to adopt a more rigorous theoretical approach to the computations in the narrow intervals without attempting to cover the entire infrared spectrum with the same model.

In previous studies [6] we have constructed the type of infrared computational model that conforms to the objectives above. Revisions have been made and more are contemplated for the future. However, during the course of this study some major revisions were enacted in conformance with the following aims:

(1) To institute more acceptable theoretical techniques for replacing nonhomogeneous optical paths with equivalent homogeneous paths

(2) To reduce the number of spectral intervals without loss of accuracy or loss of applicability to data with medium spectral resolution

(3) To incorporate desirable improvements in the analytical transmission expressions and in the integration techniques

(4) To allow for a temperature discontinuity at the lower boundary

(5) To provide a source program in FORTRAN language.

Actual upper-air data did not include ozone observations. Rather than to introduce climatological estimates of the ozone distribution, ozone was excluded from the present computational procedure even though ozone transmittance was formulated. This omission did not affect any conclusions drawn from the computations, but did restrict our computations of flux divergence to layers below the 100-mb level. Previously,[7] it was shown that fluxes computed with ozone are generally proportional to the fluxes computed without ozone.

Salient features of the revised numerical model are discussed below and some additional information is given in Appendices A, B, and C. A sizable portion of the design and testing of the revised model was performed on SRI funds. It is not possible to present a thorough exposition of the extensive analyses inherent to the model design or the details of the lengthy program within the limits of this investigation and report.

B. Spectral Limits and Definitions

Analytical expressions that were developed for the transmission in each of 25 (instead of the previous 85) spectral intervals are valid only for those intervals; if the spectral limits are altered, parameters in the transmission functions must be altered also. Table II lists the spectral intervals used in this study.

Table II

SPECTRAL INTERVALS USED IN INFRARED MODEL

Water Vapor (Rotational		Carbon Dioxide ($15-\mu$ Band)		"Window" Region		Water Vapor ($6.3-\mu$ Band)	
No.	Limits (cm^{-1})	No.	Limits (cm^{-1})	No.	Limits (cm^{-1})	No.	(Limits cm^{-1})
1	20-80	7	545-617	12	800-850	19	1250-1350
2	80-160	8	617-667	13	850-890	20	1350-1450
3	160-260	9	667-720	14	890-930	21	1450-1600
4	260-360	10	720-750	15	930-980*	22	1600-1750
5	360-460	11	750-800	16	980-1120*	23	1750-1900
6	460-545			17	1120-1190*	24	1900-2050
				18	1190-1250	25	2050-2200

* Subsequently changed to 930-970, 970-1080, and 1080-1190, respectively.

The spectral limits were determined largely on the basis of available laboratory data, but other considerations included the variation in the Planckian intensity function, gross trends in transmission, uncertainties in some spectral regions, and the potential usefulness of some regions for applications.

Table III lists definitions pertinent to the discussion of methods for computing transmission and flux; additional parameters are introduced in the discussion. The notation "ctm" refers to cm depth of an absorber reduced to standard conditions (for water vapor, ctm refers to precipitable centimeters of water). Standard conditions will be denoted by the subscript "o". With the acceleration of gravity denoted by g, the absorber depth for each of the principal molecular absorbers is defined below:

Water vapor: $W = g^{-1} \int q \, dp$

Carbon dioxide: $W = .248 \int dp$

Ozone: $W = 4.7631 \times 10^{-4} \int r \, dp.$

Table III

DEFINITIONS OF TRANSMISSION AND FLUX TERMINOLOGY
FOR AN ARBITRARY SPECTRAL INTERVAL

A = Absorption coefficient (ctm^{-1})	x,y = Dummy variables for base and top of layer
C = Transmission coefficient (ctm)	$\tau(x,y)$ = Transmittance between levels x and y (≡1 when x and y equal)
D = Transmission parameter	B_ν = Planckian intensity (cal cm^{-1} min^{-1} $strd^{-1}$)
θ = Angular departure from vertical	B_z = Black-body flux (cal $cm^{-2}min^{-1}$) for temperature at level z ($B_z = \pi \int B_\nu d\nu$)
W = Absorber depth (ctm)	S = Subscript distinguishing boundary surface from bottom of atmosphere
W_θ= Absorber path (ctm) = $W \sec \theta$	R = Reference level
$\tilde{W}$ = Equivalent homogeneous depth (ctm)	G = Lower boundary for given reference
p = Pressure (mb); p_o= 1013.2 mb	H = Upper boundary for given reference
P = Pressure (atmos) = p/p_o	L = Level of semitransparent layer
$\tilde{P}$ = Effective pressure (atmos)	ρ_z = Effective reflectance at boundary z
T = Temperature (deg k); T_o = 300°K	α_z = Effective absorptivity of boundary z
q = Specific humidity (gm/kgm)	β_θ = Effective transmittance of semitransparent layer at angle θ
u,v = Temperature-dependent weighting factors	

For carbon dioxide a constant mixing ratio has been assumed. The mixing ration, r, for ozone is given in micrograms per gram.

C. Transmission

The application of the transmission expressions to the nonhomogeneous atmosphere with nonstandard temperatures requires the introduction of equivalent homogeneous paths and effective pressures. Although there are different techniques for introducing the modifications, including the use of an effective temperature as done previously, a form of the "Curtis-Godson" approximation for water vapor and carbon dioxide is most widely accepted. One of the advantages of the Curtis-Godson approximation is that its errors[8] are, in a sense, predictable. Therefore, in spite of some loss in computing speed, the technique was introduced everywhere except in the window region. In essence, the method requires two weighting factors u and v, defined by

$$u = \sum_i S_i(T) / \sum_i S_i(T_o) \tag{5}$$

$$v = \left[\sum_i \sqrt{S_i(T)\alpha_i(P_o,T)} / \Sigma \sqrt{S_i(T_o)\alpha_i(P_o,T_o)} \right]^2 \tag{6}$$

where S is the line intensity, α is the line half-width, and the summations are performed over all lines in the given interval. As a good approximation the half-width in Eq. (6) can be factored and replaced with the quantity $(T_o/T)^{\hbar}$ as a multiplier of the squared, bracketed residual. For the 15-micron band of carbon dioxide, $\hbar$ was chosen as 0.5 and line intensities were taken from Young.[9] For the 6.3-micron band of water vapor, 0.62 was used for $\hbar$ and the summations over line intensities were determined from data presented by Wyatt et al.[10] For the rotational band of water vapor, appropriate summations were taken from Goody.[11] The u and v definitions are inadequate in the window region because of the effects of distant strong lines well outside the intervals. Curves of the u and v factors as functions of temperature are illustrated in Appendix A. All of the illustrated curves can be reproduced efficiently by polynomials of the form

$$u,v = 1 + c_1(T-T_o) + c_2(T-T_o)^2 .$$

Constants for the u and v in each spectral interval outside the window also are listed in Appendix A. In the window region u and v are treated as unity; the assumption probably is justified in view of the high transmissions and the combination of weak lines with the wing effects of distant strong lines.

The weighting factors are used to compute equivalent homogeneous absorber depths and effective pressures in the atmosphere from

$$\widetilde{W} = \int u \; dW \tag{7}$$

$$\widetilde{WP} = \int v \; P \; dW \quad . \tag{8}$$

A rational basis for the analytical representation of the transmission in an arbitrary spectral interval was established by adopting a technique suggested by Godson[12] for treating laboratory data. The first step is to form the function ψ_n from

$$\psi_n = [\Phi^{-1} (1 - \tau)]^n [-\ell n \; \tau]^{1-n} \tag{9}$$

where Φ^{-1} is the inverse error function with argument $(1 - \tau)$. The exponent n is determined by successive approximations until a universal plot of ψ_n/W is achieved in terms of W/P on a log-log graph. The resulting universal curve can be described with a polynomial, but also can be expressed in the form

$$\psi_n/W = A[(W/P) + C]^D \tag{10}$$

by determining the coefficient C (through additional successive approximations) such that ψ_n/W and $[W/P) + C]$ plot as a straight line on a log-log graph. Then, A and D are specified by the intercept and slope of the line, respectively. The form of Eq. (10), in conjunction with Eq. (9), is flexible enough to include a wide variety of transmission representations. The random model of Goody[13] is represented by $n = 0$ and $D = -0.5$; the regular error-function model of Elsasser[14] in reduced form is obtained with $n = 1$, $D = -0.5$, and $C = 0$. For water vapor and carbon dioxide the coefficient C can be approximated as a constant in a given spectral interval. However, for the 9.6-micron band of ozone, agreement with the data of Walshaw[16] was obtained with $C = \exp[AW]$, along with $n = 0$ and $D = -0.5$. (With P as the mean pressure and W as the total ozone path, A was found to be 2.6 for the band as a whole.)

As an example of the procedure for fitting data to the desired format of Eq. (10), Fig. 5 illustrates three stages of analysis of laboratory data[16] (homogeneous path) for carbon dioxide in the 617- to 667-cm^{-1} interval. The upper portion of Fig. 5 shows the initial plot of selected data points with $n = 0$ (i.e., $\psi_n = -\ln \tau$). A separation of data according to pressure is obvious. After successive trials with n, a universal fit for all ranges was found for $n = -0.9$ (middle curve). Finally, after additional trials, a value of 0.8 for C was found to produce the straight-line fit (lower curve). Thus, the parameters for Eq. (10) are determined from the fit as $A = 1.02$, $C = 0.8$, and $D = -0.46$.

Available data indicated that only for carbon dioxide was it mandatory to retain a nonzero value for n. Thus, while ψ_n could be replaced with $-\ln \tau$ for water-vapor bands, the recovery of τ from ψ_n for carbon dioxide presented a computational problem [see Eq. (9)]. The procedure adopted was to compute $\ln \psi_n$ with the aid of Eq. (10), then to extract $-\ln \tau$ for each application from second-degree interpolation with $\ln \psi_n$ in a computer-stored table generated from Eq. (9). Points in the table were carefully selected to ensure that the polynomial interpolation could never introduce a change in sign of the first derivative of τ or $\ln \tau$.

It was concluded that the form of the Goody random model ($\psi = -\ln \tau$, $D = -1/2$) was an adequate representation for transmission in the rotational and 6.3-micron bands of water vapor. If δ, $\bar{S}$, and $\bar{\alpha}$ refer to the mean line spacing, intensity, and half-width, respectively, in an interval, then the Goody model can be described by

$$-\ln \tau = \frac{\bar{S}W}{\delta\sqrt{1 + \bar{S}W/\pi\bar{\alpha}}} . \tag{11}$$

This expression can be linked directly to the Curtis-Godson approximation with the definitions

$$\bar{S}W = \bar{S}_o \int u \, dW = \bar{S}_o \tilde{W} \tag{12}$$

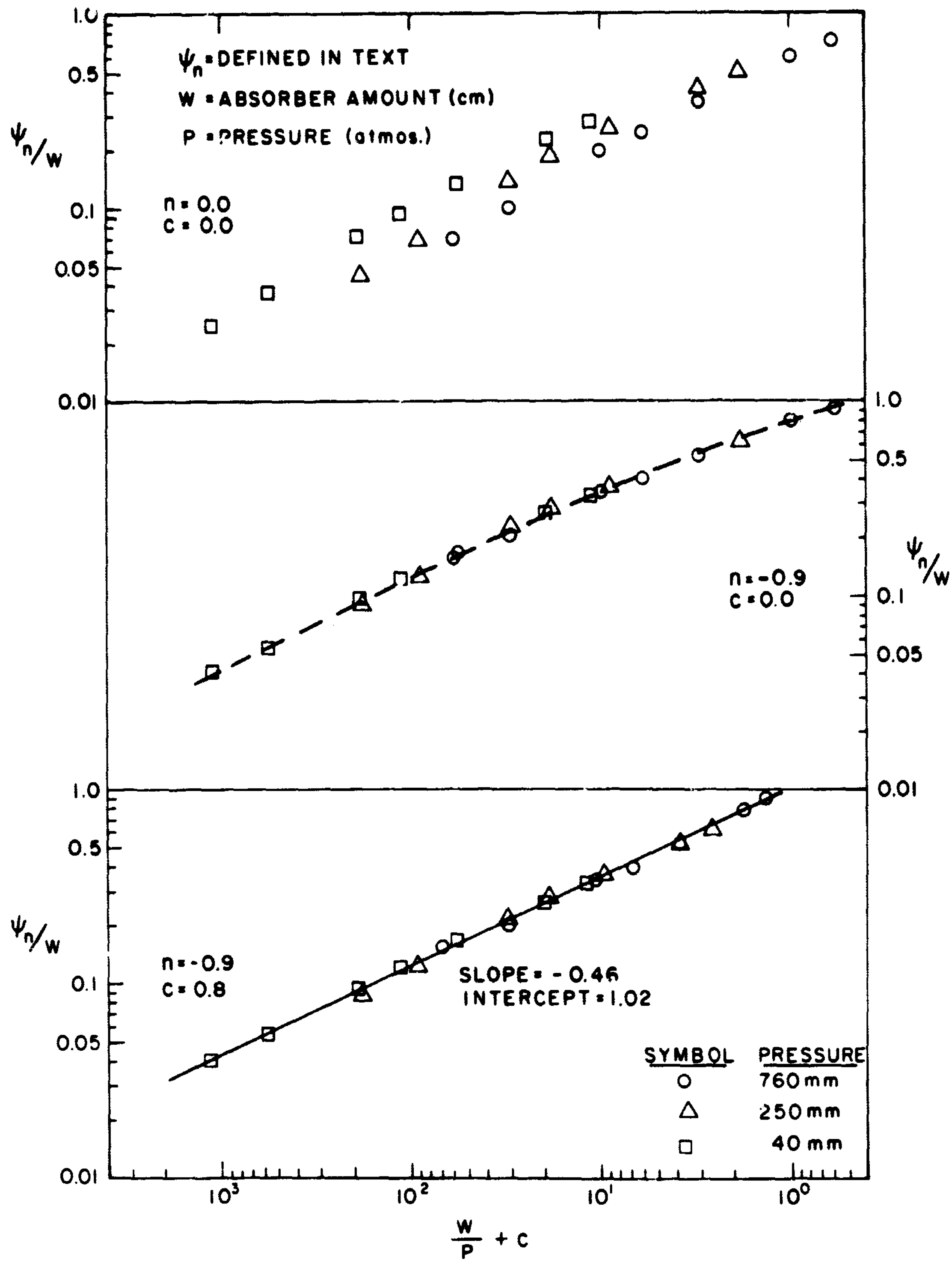

FIG. 5 EXAMPLE OF CARBON DIOXIDE TRANSMISSION REPRESENTATION BASED ON LABORATORY DATA (617-667 cm^{-1})

and

$$\bar{\alpha} = \bar{\alpha}_o \frac{\int P\ v\ dW}{\int u\ dW} = \bar{\alpha}_o\ \widetilde{WP}/\widetilde{W} \quad . \tag{13}$$

Thus, from Eqs. (11) through (13), the coefficients A and C in Eq. (10) can be defined as $A = \bar{S}_o \sqrt{C}/\delta$ and $C = \pi\bar{\alpha}_o / \bar{S}_o$. These definitions enable comparisons with other analyses[17] and are useful in the final selection of A and C to provide a desirable transmission representation.

Data available for a reliable transmission representation for the window region are so limited that an optimum empirical expression has not been specified. It is unfortunate that more attention has not been given to this spectral region because contributions from the window region dominate the outgoing flux. Since there are uncertainties associated with variable absorbers other than water vapor, it seems appropriate to allow some spectral breakdown in the window region for future readjustments of parameters. The simplest transmission representation from Eq. (10) is suggested by setting $n = 0$ ($\psi_n = -\ell n\ \tau$) and $C = 0$, leaving A and D for a two-parameter fit to data. However, in view of residual uncertainties with data, we have retained the simpler form

$$\tau = \exp\left[-(AWP)^D\right] \tag{14}$$

for all spectral intervals between 800 cm^{-1} and 1190 cm^{-1} when ozone is excluded. For the spectral interval 1190-1250 cm^{-1}, which actually can be considered the tail of the 6.3-micron band of water vapor, neither Eq. (14) nor the Goody model describes the transmission adequately. Consequently, for this one interval the transmission was expressed by

$$\tau = \exp\left[-(AW\sqrt{P})^D\right] \quad . \tag{15}$$

Constants for all of the transmission representation are listed in Appendix B. The general computational procedure for transmittance was first to compute $\ell n[-\ell n \tau]$, and then to exponentiate twice. For computations of beam transmittance at a particular angle θ, the optical depth W was divided by cos θ. The beam transmittance and the flux transmittance (i.e., the transmittance for a flux computation into the forward or backward hemisphere) are related by

$$\tau_F(W) = \int_0^1 \tau(W/\cos\theta)\, d\cos^2\theta \quad . \tag{16}$$

An accurate and convenient shortcut to the integration in Eq. (16) over all angles was devised for each spectral region. The approximation was included in the transmittance computation as a function of pertinent transmission parameters in each interval; in other words, a constant beam-to-slab conversion factor was not used. The procedure for circumventing the use of Eq. (16) at each step was devised on the basis of an analysis of computations by Armstrong[18] for the rotational and vibrational-rotational bands of water vapor. For the window region and for the 15-micron band of carbon dioxide (with superposed water-vapor absorption) the conversion to flux transmittance was based on actual integrations with Eq. (16) for typical conditions. Parameters for the computations of flux transmittance are given in Appendix C. Computations of τ over successive increases in path are continued until τ becomes smaller than 0.00005, at which point τ is treated as zero.

D. Flux Computations

The general flux expressions for computing the downward or upward flux at a reference level R can be described separately for R above or below an allowable semitransparent layer, L, with infinitesimal thickness. Basically, the derivation of the expressions is identical to that used previously. The critical assumption is that the intensity of radiation from a boundary surface is isotropic; the diffuse radiation scattered into the backward hemisphere is associated with the average incident intensity in the spectral interval from all hemispheric angles. Since the effective absorptance and reflectance were invariant with angle, the source intensity I at a boundary was described as $I = \alpha B_\nu + \rho F/\pi\Delta\nu$. For a nontransparent boundary, $\alpha = 1 - \rho$, whereas for a semitransparent layer, $\alpha = 1-\rho-\beta$. Due to a lack of empirical data, estimates of the effective transmittance (β) were "rational" guesses based on the cloud and humidity conditions. For a radiance computation, β is input with the specified angle in order to allow for limb darkening. In specific applications a maximum darkening was allowed for an average transmittance of 0.5; as the average transmittance approached 0 or 1 the darkening was eliminated. For flux computations a single effective β was specified (without angular dependence).

For the selected wave-number intervals it was assumed that no significant correlation existed between the Planckian intensity, or its derivative, and the transmittance. Local horizontal homogeneity in the atmosphere was assumed. This assumption dictated that, for a variable state of the sky, flux computations had to be performed separately for clear skies and for each typical cloud layer, then weighted to obtain a total flux. Finally, the assignment of infinitesimal thickness to the semitransparent layer dictated that for a realistic flux computation the reference level should be exterior to the actual semitransparent layer, although a result can be computed for R=L. Of course, it is not necessary to insert a semitransparent layer in every application.

With the above restrictions the two sets of flux expressions for any given spectral interval were put in the form

$\boxed{R \geq L}$

$$F_R\downarrow = B_R - \epsilon B_H\tau(R,H) + \int_R^H \tau(R,y)\,dB_y + \rho_H\tau(R,H)[F_H\uparrow - B_H] \tag{17}$$

$$\begin{aligned} F_R\uparrow = B_R - \int_L^R \tau(x,R)\,dB_x - \beta\int_G^L \tau(x,R)\,dB_x + \beta\tau(G,R)[(B_S-B_G)+\rho_G(F_G\downarrow-B_S)] \\ + \rho_L\tau(L,R)\left[\int_L^H \tau(L,y)\,dB_y - \epsilon B_H\tau(L,H)\right] \end{aligned} \tag{18}$$

$\boxed{R \leq L}$

$$\begin{aligned} F_R\downarrow = B_R + \int_R^L \tau(R,y)\,dB_y + \beta\left[\int_L^H \tau(R,y)\,dB_y - \epsilon B_H\tau(R,H)\right] \\ - \rho_L\tau(R,L)\left[\int_G^L \tau(x,L)\,dB_x - \tau(G,L)[B_S-B_G]\right] + \beta\rho_H\tau(R,H)[F_H\uparrow - B_H] \end{aligned} \tag{19}$$

$$F_R\!\uparrow = B_R - \int_G^R \tau(x,R)\,dB_x + \tau(G,R)\Big[(B_S - B_G) + \rho_G(F_G\!\downarrow - B_S)\Big] \tag{20}$$

where the term $(B_S - B_G)$ represents the important temperature discontinuity[18] at the lower boundary.

When the upper boundary H refers to the top of the model atmosphere, then ϵ is unity and ρ_H is zero; otherwise ϵ is zero. When no semitransparent layer is desired, the equations can be reduced (or L can be set equal to H and β to unity). If no temperature discontinuity is specified at the lower boundary, then $B_S = B_G$. Minor terms with multiple reflectances are ignored.

In all applications of the flux expressions in this study, ρ_H was taken as zero, thereby eliminating terms explicitly containing $F_H\!\uparrow$. The general computational procedure was first to compute integrals involving the limit L, then to compute all transmittances involving G as well as $F_G\!\downarrow$ from the expression for $F_R\!\downarrow(R \leq L)$ with G substituted for R. Finally, all transmittances and fluxes involving R were computed. Fluxes were output for each interval in addition to the cumulative total for all intervals. Pressure, temperature, and specific humidity at any number of data levels are provided as input, along with all desired sets of ρ, β, L, G, H, R, θ, and T_S.

Instead of computing B for every application, a matrix of B (for each spectral interval) and T was generated for equally spaced temperatures and stored in the computer. For the given temperature at each data level the corresponding B in each spectral interval was extracted directly from the matrix by interpolation. The matrix also is used in reverse fashion to extract the equivalent temperature for a computed flux by entering the matrix with F instead of B, and then finding the corresponding T.

Integrations of the transmittance with respect to B as a function of height, either upward or downward, were performed numerically over successively longer paths extending from the reference level. The paths are determined by the data levels. The simple trapezoidal integration method for unequally spaced points was found to yield quite satisfactory results except for the layers adjacent to the reference level. Here the nonlinearity can be very pronounced in regions of strong absorption. An appropriate integration technique near the reference level can be derived by specifying the general functional forms of τ and B. For example, it can be postulated that

$$\tau = \exp\left(-c\,\ln \frac{p_R}{p}\right)$$

and

$$B = B_i \exp\left(-b\,\ln \frac{p_i}{p}\right) = B_i \exp\left(-b\left[\ln \frac{p_R}{p} - \ln \frac{p_R}{p_i}\right]\right) \tag{21}$$

where b and c are arbitrary constants determined by data at the two levels p_i and p_j bounding the layer of interest. Thus the integral $\int \tau\, dB$ between the levels can be evaluated directly, instead of by trapezoidal methods, as

$$\int \tau \frac{dB}{d\ln(p_R/p)}\, d\ln(p_R/p) = \ln(B_j/B_i)\, \frac{(\tau_i B_i - \tau_j B_j)}{\ln(\tau_i B_i) - \ln(\tau_j B_j)} \tag{22}$$

where the lower and upper integration limits are $\ln(p_R/p_i)$ and $\ln(p_R/p_j)$, respectively. A simpler result can be obtained by a less accurate approximation for B between the two levels:

$$B = B_i + b\left[\ln \frac{p_R}{p} - \ln \frac{p_R}{p_i}\right] \; . \tag{23}$$

Now the integral between $\ln(p_R/p_i)$ and $\ln(p_R/p_j)$ becomes

$$\int \tau \frac{dB}{d\ln(p_R/p)}\, d\ln(p_R/p) = (B_j - B_i)\, \frac{(\tau_i - \tau_j)}{(\ln \tau_i - \ln \tau_j)} \tag{24}$$

where, as before, $\tau_i = \tau(p_R, p_i)$ and $\tau_j = \tau(p_R, p_j)$. Although Eq. (21) is a more accurate representation of B than is Eq. (23), tests showed that for typical spacings of data levels the error incurred by Eq. (23) was not significant. Therefore, in this study Eq (24) was used for each layer <u>adjacent</u> to the reference level and the trapezoidal method was used for all successive layers. Thus, for example,

$$\int_R^H \tau(R,j)\ dB_j \approx (B_{R+1} - B_R)\ \frac{[1-\tau(R,R+1)]}{-\ell n\ \tau(R,R+1)}$$

$$+\ 0.5 \sum_{j=R+1}^{H-1} (B_{j+1} - B_j)[\tau(R,j) + \tau(R,j+1)]$$

and

$$\int_G^R \tau(i,R)\ dB_i \approx (B_R - B_{R-1})\ \frac{[1-\tau(R,R-1)]}{-\ell n\ \tau(R,R-1)}$$

$$+\ 0.5 \sum_{i=2}^{B-G} (B_{k+1} - B_k)[\tau(R,k) + \tau(R,k+1)]$$

where, in the last summation, k=R-i.

E. Sample Results

Figure 6 illustrates temperature profiles and relative humidities for 1800 GMT at Great Falls and Fort Worth on 26 and 27 June 1966, respectively. Clear skies prevailed at both stations. Great Falls is under the slightly cooler and drier regime; Fort Worth is about 15 degrees of latitude southward at an elevation of 175 m, as compared to 1115 m at Great Falls. As indicated in Fig. 6, the computed outgoing long-wave flux at the top of the model atmosphere (0.1 mb) is larger at Fort Worth than at Great Falls, but the effective (net) radiation at the surface is smaller. Therefore, the largest total infrared cooling of the atmosphere also occurs over Fort Worth, although in part this results from the greater depth of atmosphere there. On the other hand, in terms of local solar time, the Great Falls observations are representative of one hour earlier in the morning--i.e., surface temperatures and the effective radiation have not yet reached their maxima.

Figure 7 shows, for each station, the computed equivalent blackbody temperatures for radiance computations in spectral intervals that are representative of the spectral responses of the four infrared channels on Nimbus II. Radiance computations were made at a variety of zenith angles in order to illustrate the limb variations. Nimbus II measurements,

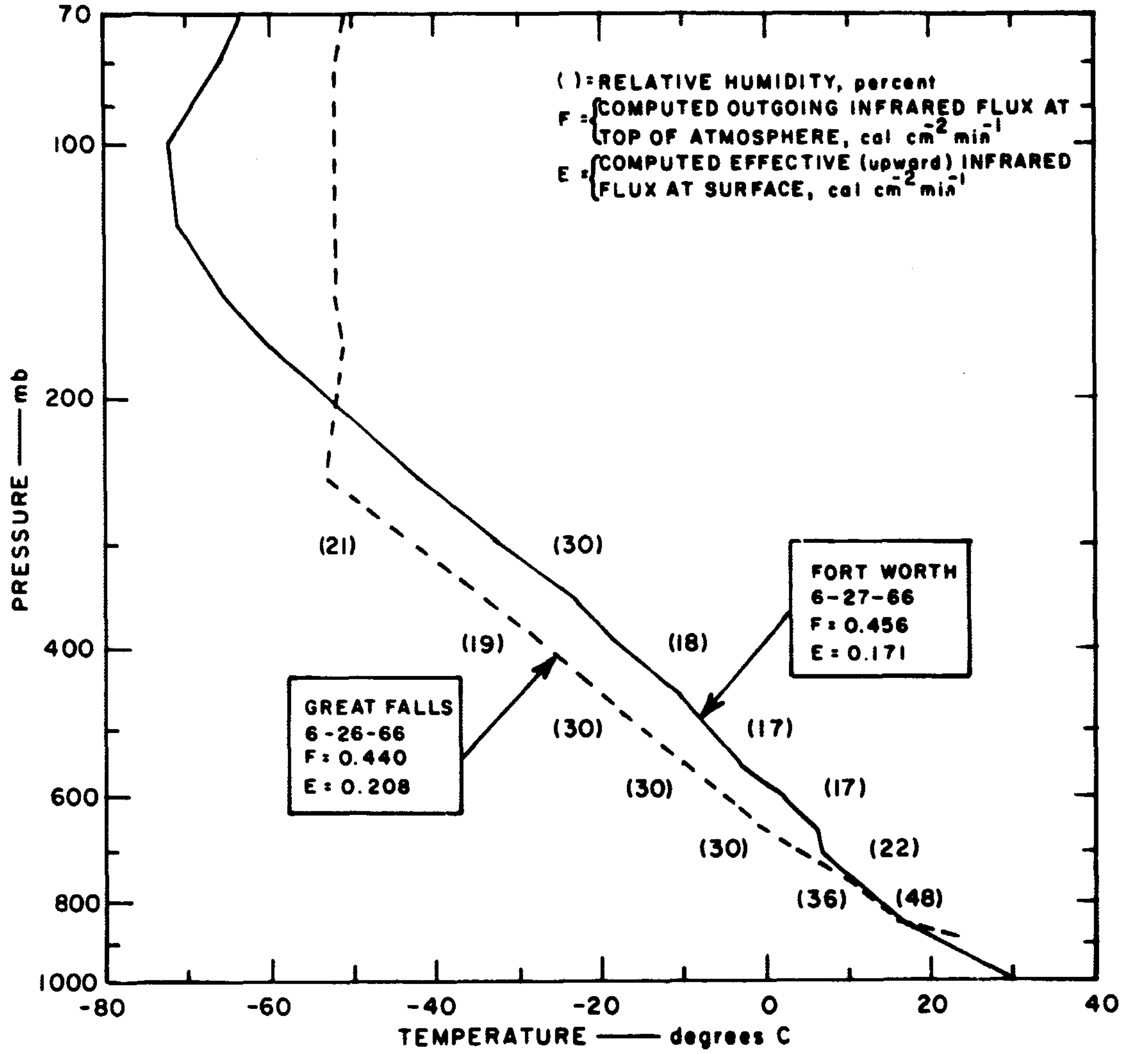

FIG. 6 EXAMPLES OF SOUNDINGS AND COMPUTED INFRARED FLUXES FOR CLEAR SKIES AT TIME OF NIMBUS II PASS (1800 GMT)

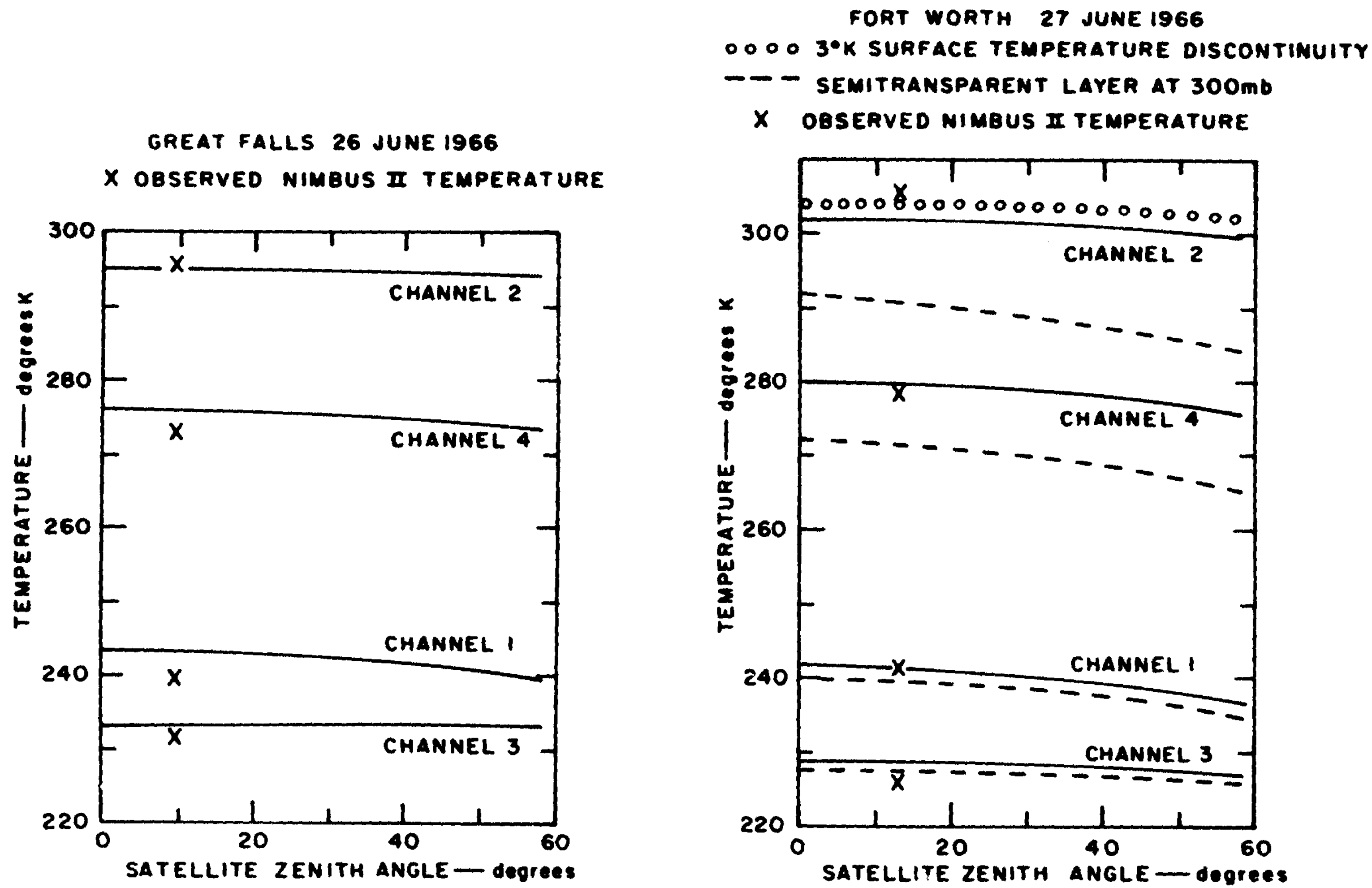

FIG. 7 COMPUTED LIMB VARIATIONS IN RADIOMETRIC RESPONSE FOR SOUNDINGS ILLUSTRATED IN FIG. 6. Additional boundary conditions assumed at Fort Worth.

in terms of equivalent temperatures from each channel, were obtained concurrently and are indicated on Fig. 7.

At both stations the observed Channel 2 temperature is higher than the computed temperature for the satellite zenith angle, especially over Fort Worth. A logical explanation is that the actual surface temperature was larger than the shelter-height temperature, with the larger discrepancy at Fort Worth since the observations there were closer to local noon. In fact, when a 3-degree temperature discontinuity was assumed at Fort Worth, the computed Channel 2 temperature was almost the same as that observed. At Great Falls the limb darkening for Channel 2 out to 58-degree zenith angle was 1°K; a 2°K darkening was computed for Fort Worth with the greater water-vapor content.

At both stations the observed Channel 4 temperature was lower than that computed. A discrepancy in this direction was expected because ozone was not included in the computations. The temperature reduction due to ozone should be larger at Great Falls because of the larger ozone amount there. Other absorbers also could have influenced the results. Limb darkening for Channel 4 was computed to be twice as large as that for Channel 2. The computed and observed Channel 1 temperatures agreed exactly at Fort Worth but at Great Falls the observed Channel 1 temperature was lower. Since less than one-tenth of scattered high clouds were observed in the area, it is tempting to conclude that the slightly lower observed Channel 1 temperature at Great Falls was due to a cirrus effect, or even to an unobserved increase in water-vapor content in the upper troposphere. Limb darkening for Channel 1 was computed to be about 4°K (out to 58-deg zenith angle) at Great Falls and 5°K at Fort Worth.

Channel 3 showed about a 1-degree limb darkening over Fort Worth but less than half a degree over Great Falls. The observed Channel 3 temperature was slightly lower than the computed temperature, primarily because the spectral region covered in the model computations was broader than that covered by the radiometer. Thus, the computed Channel 3 temperature received contributions from lower and warmer depths in the atmosphere.

The dashed lines in the plot for Fort Worth in Fig. 7 represent the results of the computations for the presence of an arbitrary semi-transparent layer (thin cirrus) with a transmittance that was allowed to vary from 0.79 at the zenith to 0.66 at a zenith angle of 60 degrees. Of course, the insertion of the layer is merely hypothetical; no corresponding alterations of moisture or temperature structure were introduced. The effect of the semitransparent layer is most pronounced on the computed Channel 2 temperature. At the zenith it reduces the Channel 2 temperature by more than 9°K, whereas at the 58-degree zenith angle the reduction is more than 15°K. Thus, the limb darkening from 0 to 58-degree zenith angle for this hypothetical Channel 2 computation is increased from 2°K to 8°K. To the extent that the computation is realistic, it suggests that the limb variation in the Channel 2 response over an apparently uniform (perhaps clear) background in an AVCS picture could be utilized to ascertain whether or not cirrus was present.

The effect of the semitransparent layer on Channel 4 is significant but less pronounced than on Channel 2. Only a very small effect on the Channel 1 response was computed, and the effect on Channel 3 was negligible.

IV INFRARED ANALYSIS AT SELECT PACIFIC STATIONS

A. Data Processing

The final analysis of data from rawinsonde locations in the Pacific was restricted to 1200 GMT (local midnight) observations at the five stations listed in Table IV. The number of days for which usable data were acquired concurrently with Nimbus II passes during the last half of June is indicated also.

Table IV

STATION DESCRIPTORS FOR LOCAL ANALYSIS IN PACIFIC, 16-30 JUNE 1966

Station	Station Height (m)	Latitude	Longitude	No. of days
Shemya	38	52.7°N	174.1°E	14
Adak	4	51.9°N	176.7°W	14
Wake	5	19.3°N	166.6°E	14
Eniwetok	5	11.3°N	162.3°E	15
Ponape	39	7.0°N	158.2°E	13

For the first two stations in Table IV, the radiometric nadir angle and the temperature data from the four infrared channels of Nimbus II were averaged for all scan spots falling within a grid size of 1 degree of latitude and 1.8 degrees of longitude at the station location. For the three tropical stations, a 1-by-1-degree grid was used. All satellite data were extracted from listings; limb corrections were applied as described earlier. Rawinsonde data were obtained in the form of punched cards with data at 50-mb intervals through the troposphere and smaller intervals in the stratosphere. Upper-air data at significant levels also were extracted from microfiche records. Each sounding was checked and, if necessary, the temperatures were extrapolated upward to the 10-mb level with the aid of interpolation from neighboring soundings. A total of 34 data levels were used for each sounding, with fixed data points for the two uppermost levels at 1.0 mb and 0.1 mb. At Shemya and Adak the temperatures assigned were 285°K and 230°K for 1.0 and 0.1 mb, respectively. At the three tropical stations corresponding temperatures of 273°K and 235°K were assigned; at all stations a fixed specific humidity of 0.025 grams per kilogram was assigned to the two uppermost levels.

Instead of assigning a fixed set of specific humidities at data levels in the stratosphere, an empirical expression (based on previous estimates for stratospheric moisture) was devised to enable an estimate of the specific humidity (q) on the basis of the observed temperature:

$$\ln q = 0.0012\ (T-198.2)^2 + 0.046\ (T-198.2) - 6.9 \qquad (25)$$

for q in grams per kilogram and T in degrees Kelvin. This expression was used for data levels near or just below the mean tropopause height up to the 10-mb level. In the troposphere, at any pressure p with observed relative humidity h, the specific humidity was determined from the approximation

$$\ln q = \ln(h/p) + [28.089 - (5418/T)]. \qquad (26)$$

A computer routine was devised to extrapolate ln q upward to, and including, the lowest level at which Eq. (25) was applied; at that level the two values of ln q were averaged arithmetically in the computer routine.

Sea-surface temperatures from ship reports in the general vicinity of each station were examined and a characteristic sea-surface temperature was assigned to the waters around each station on each day. Whenever a significant difference existed between the "surface" temperature at the station and the sea-surface temperature, then a temperature discontinuity was introduced at the lower boundary for the radiation computations. The main reason for introducing the discontinuity was to provide a proper background that corresponded more closely with the satellite view. Only at Ponape was there a persistent temperature difference.

Having completed the description of the temperature and moisture profiles for every sounding, it was necessary to specify all of the cloud boundaries at each time, including overlapping layers. From the point of view of accuracy in the computation of local infrared fluxes, the cloud specification is a most important and most difficult task. Unfortunately, no satisfactory method exists for a reliable, objective description of clouds on the local scale. Not only does the lack of an objective description make it difficult to perform radiation computations but it makes it impossible to correlate cloud data with other statistics. Although HRIR data existed for most of the Nimbus II passes, the data were insufficient for a local cloud specification in view of uncertainties in gridding accuracy and interpretation. Therefore, it was necessary to assemble all pertinent surface observations of cloudiness and compare these reports with the microfiche upper-air profiles of temperature and relative humidity. With the reported base-height of the low clouds and the humidity data, reasonable estimates of the tops and bottoms of the low clouds were obtained, even under conditions of scattered sky cover. Middle clouds are much more difficult to locate, especially when more than one layer is possible, but spiky increases in relative humidity usually are observed. For thin middle clouds a single level (infinitesimal sheet) often was assigned; total amounts were based on the cover in the unobstructed sky. All cirrus clouds were treated as infinitesimal semitransparent layers with average view-angle transmittances assigned on the basis of relative humidity, cloud amount, and Channel 2 temperature. Obviously, the specifications of cirrus cloudiness were the most difficult and least accurate. When the cirrus clouds occur entirely above the range of reported relative humidity, it is necessary to consider changes in the temperature profile, winds, evidence of precipitation, and neighboring observations (space and time) as aids in the cirrus specification. Radiometric measurements in window regions must be used, after lower clouds are specified, to indicate the presence (and in some cases, height) of potential cirrus when insufficient information is available from surface reports.

The cloud specifications probably represented the most time-consuming aspect of the data analysis. When they were completed, each was checked with the corresponding HRIR view to ensure compatibility in a gross sense. However, what is sorely needed is an objective procedure for specifying the cloudiness, even if only an "effective" cloudiness, that will yield the observed radiometric measurements in an unambiguous fashion. The biggest weakness in the cloud specifications used here is that there was no demand that the radiometric measurements be duplicated by computation, in spite of the fact that the basic computational tool was devised. Of course, the model still must be expanded to include ozone, and empirical information is needed to establish the magnitudes of some parameters, especially those concerning cloudiness. Furthermore, such a check would require that a computation be made for the view angle of the satellite against an appropriate description of the irregular cloud boundary.

In the present flux application, the reflectance of the surface (largely water) was set equal to zero, but the reflectance of the lower boundary when it was an opaque cloud top usually was set at 0.1; reflectances for cirrus clouds were set at 0.05. Transmittances assigned to the cirrus clouds ranged between 0.1 and 0.7, but it is likely that even more tenuous cirrus existed.

Each cloud, single- or multi-layered, was treated as a locally homogeneous entity in the horizontal plane during a flux computation. In this application the reference levels for computing the fluxes were selected at the surface, each opaque cloud top, 500 mb, 200 mb, and 100 mb. On some occasions a cloud layer would straddle the 500-mb level; for these clouds, upward and downward fluxes computed at the top and bottom of the cloud would be averaged and used to describe the upward and downward fluxes at 500 mb. After fluxes at all reference levels were computed for each cloud (or clear sky), each flux would be weighted by the fraction of sky covered by its sky condition. The application of the weighting factor actually allows adjustment to compensate for changes in reflectances or transmittances of clouds, if desired. The sum of the weighting fluxes then constituted the final flux at the reference level for the total sky condition. Cooling rates for layers were computed from the divergence of the final fluxes over the pressure increment of the layer.

For a variety of atmospheric depths, and for all layers over which the infrared cooling was computed, calculations were made of the total potential energy and of the precipitable water. Totals of the precipitable water, Q, were obtained by simple trapezoidal integration of the specific humidity with respect to pressure and sion by the acceleration of gravity. The total potential energy, $E_{i,j}$ (a measure of average temperature), between levels p_i and p_j is given by

$$E_{i,j} = p_i Z_i - p_j Z_j + \frac{c_p}{g} \int_{p_j}^{p_i} T^* \, dp \tag{27}$$

where Z is the height of the pressure surface and T^* is the virtual temperature;at the bottom of the atmosphere, $p_i Z_i$ becomes $p_G Z_G$. In practice, the total potential energy was computed from the surface (p_G) to an arbitrary level (p_j) with the expression

$$E_{G,j} = \frac{c_p}{g} \int_{p_j}^{p_G} T \, dp - p_j \left[(Z_j - Z_G) + Z_G \right] + p_G Z_G \quad . \tag{28}$$

Instead of using the listed heights, the thickness $Z_j - Z_G$ was approximated from the relationship

$$Z_j - Z_G = g^{-1} R \, \bar{T}^* \, \ell n \, (p_G/p_j)$$

where the bar represents an average over the layer. Although the temperature generally varies linearly with the logarithm of pressure, trapezoidal integration with respect to pressure was employed in Eq. (28) with little error, and the same integral was used in the definition of $\bar{T}^*$. Finally,

$$E_{G,j} = f(p_j) \int_{p_j}^{p_G} T \, dp + p_G Z_G$$

where $f(p_j) \approx 1.02 - 0.293 \, p_j \, (\ell n \, p_G - \ell n \, p_j)/(p_G - p_j)$. Values of E for layers not bounded by the surface are obtained as the difference in $E_{G,j}$ for two values of p_j.

B. 15-Day Averages

Rather than attempt to present all of the analyzed data for each day, only the 15-day averages and standard deviations of some of the pertinent quantities are tabulated. Table V lists the definitions of symbols presented in subsequent tables.

Table V

DEFINITIONS OF SYMBOLS IN DATA SUMMARIES FOR PACIFIC STATIONS

T1, T2, T3, T4	= Radiometric response temperature (°K) from Channels 1, 2, 3, and 4, respectively, of Nimbus II
R(G,5), R(5,1), R(G,1)	= Radiative cooling (deg day^{-1}) in layer from surface to 500 mb, 500 mb to 100 mb, and surface to 100 mb, respectively
E(G,5), E(5,1), E(G,1)	= Total potential energy (kj cm^{-2}) in layer from surface to 500 mb, 500 mb to 100 mb, and surface to 100 mb, respectively
E(2,0.1)	= Total potential energy between 200 mb and 10 mb
F_N(G)	= Net upward-minus-downward infrared flux at surface (cal cm^{-2} min^{-1})
F_U(1)	= Upward infrared flux at 100 mb
Q(5,2)	= Precipitable water (ctm) between 500 mb and 200 mb
Q(G,1)	= Precipitable water (ctm) between surface and 100 mb
P_G	= Surface pressure (mb)
P_T	= Pressure (mb) at tropopause identified by USWB

Table VI lists the means and standard deviations of these variables at each of the 5 stations during the last half of June. Some of the important features are reviewed below.

To the extent that the mean temperature in the upper troposphere is constant, the Channel 1 temperature, T1, portrays the variation in

Table VI

MEANS AND STANDARD DEVIATIONS OF SELECT VARIABLES, 16-30 JUNE 1966, PACIFIC STATIONS

(Symbols defined in Table V)

	Shemya		Adak		Wake		Eniwetok		Ponape	
	Mean	S.D.	Mean	S.D.	Mean	S.D.	Mean	S.D.	Mean	S.D.
T1	235.9	3.1	234.3	3.2	242.4	7.7	238.3	9.3	232.9	10.3
T2	263.5	5.0	261.2	8.9	289.4	11.2	279.6	19.9	270.9	21.4
T3	232.3	0.6	232.2	0.7	224.9	0.8	223.6	1.6	222.7	2.1
T4	253.7	4.2	252.0	6.4	269.9	9.3	261.9	15.7	253.8	16.7
R(G,5)	2.24	0.75	2.02	0.77	2.10	0.47	1.86	0.54	1.89	0.93
R(5,1)	1.33	0.49	1.36	0.40	1.53	0.18	1.70	0.27	2.34	1.06
R(G,1)	1.71	0.26	1.66	0.20	1.85	0.22	1.77	0.29	1.55	0.39
E(G,5)	112.5	2.21	113.2	1.79	120.6	0.27	120.1	0.40	118.8	0.25
E(5,1)	104.8	0.32	104.9	0.30	108.1	0.30	108.4	0.20	108.3	0.14
E(G,1)	217.4	2.33	218.1	1.95	228.7	0.45	228.5	0.55	227.1	0.28
E(2,0.1)	64.3	0.17	64.5	0.14	62.9	0.13	62.7	0.14	62.4	0.15
$F_N(G)$	0.018	0.017	0.015	0.010	0.107	0.018	0.084	0.025	0.064	0.029
$F_U(1)$	0.303	0.036	0.293	0.032	0.406	0.048	0.367	0.066	0.313	0.067
Q(5,2)	0.056	0.030	0.067	0.030	0.145	0.077	0.250	0.117	0.310	0.112
Q(G,1)	1.081	0.236	1.237	0.234	4.209	0.468	5.173	0.838	5.517	0.312
P_G	1012.5		1014.7		1014.6		1010.5		1004.8	
P_T	273.8				135.5				106.1	

the upper level specific humidity, represented by Q(5, 2). For the three tropical stations the upper tropospheric temperature, described by E(5,1), is reasonably constant and T1 varies with Q(5,2). Channel 2 responds in an inverse manner to the cloudiness, as well as to variations in the mean surface temperature. Resultant trends for the selected data sample are dominated by the cloudiness. Variations of T2 are best described by variations in the outgoing long-wave radiation [represented here by $F_U(1)$], but appear to correspond also to variations in the effective long-wave radiation at the surface, $F_N(G)$. Variations in T3 correspond to spatial variations in the mean stratospheric temperature, represented here by E(2,0.1), and especially to spatial variations in tropopause height.

The most significant aspect of the computations of radiative cooling for the tropical stations is the implication of the destruction of zonal potential energy. In the lower troposphere, a slight increase of potential energy is observed in the poleward direction, from Ponape to Wake. The largest cooling occurs at Wake, where the heat input at the surface is largest. However, in the upper troposphere the largest average cooling at all stations occurs at Ponape, in spite of the fact that the potential energy is nearly constant. Thus, in the upper troposphere another source must supply heat to the equatorward end in order to maintain the observed temperature structure. The source could be the latent heat released in association with the increased convection and cloudiness in this region; eddy heat transports could play a role also. It may be noted that the variance in the upper-level cooling over Ponape was unusually large.

Although a truly objective description of cloudiness was not possible, the average fractional amount of the grossly-classified cloudiness (low, middle, high) is presented in Table VII. The listed fractions are not

Table VII

AVERAGE FRACTIONAL CLOUD AMOUNT BY HEIGHT
16-30 JUNE 1966, PACIFIC STATIONS

Station	Cloud Amount		
	Low	Middle	High
Shemya	0.95	0.33	0.43
Adak	0.99	0.43	0.56
Wake	0.20	0.07	0.20
Eniwetok	0.29	0.15	0.49
Ponape	0.47	0.40	0.63

exclusive--that is, overlapping of cloud layers did occur. The equatorward increase of cloudiness, especially high clouds, is obvious in the tropics as the inter-tropical convergence zone is approached. For the two stations in the Aleutians, a low overcast existed almost throughout the period. Therefore, these stations are not typical of their latitude. The slightly larger cloud cover at Adak is reflected in the slightly smaller average Channel 2 temperature.

C. Correlations and Covariances

Covariances (in time) between infrared cooling rates and total potential energy were computed; some results are given in Table VIII.

Table VIII

COVARIANCES BETWEEN INFRARED COOLING (deg/day) AND TOTAL POTENTIAL ENERGY (kj/cm^2), 16-30 JUNE 1966, PACIFIC STATIONS

(Correlation coefficients in parentheses)

	Covariances		
	Surface to 500 mb	500 mb to 100 mb	Surface to 100 mb
Shemya	0.17 (0.11)	-0.07 (-0.48)	0.30 (0.53)
Adak	0.26 (0.20)	0.05 (0.49)	0.01 (0.03)
Wake	0.02 (0.14)	-0.01 (-0.20)	0.04 (0.41)
Eniwetok	-0.10 (-0.49)	-0.01 (-0.10)	-0.07 (-0.44)
Ponape	0.05 (0.24)	-0.00 (-0.02)	-0.00 (-0.03)

The covariance provides some indication of the destruction (generation, if negative) of total potential energy by infrared radiation, but does not treat components of the potential energy separately. All of the computed covariances in Table VIII were insignificant by comparison with previous magnitudes.[7] Largest magnitudes occurred in the lower troposphere over the Aleutian stations; the sense of the covariance was positive, in contrast to substantial negative values in the earlier study for northern latitudes in summer. Of course, the Aleutian stations were not typical of the latitude.

In this study, statistics at a given station were accumulated in time; in the earlier study, statistics were accumulated in space from a number of stations at a given time. It is possible that significant covariances are found only in relation to zonal potential energy and are not revealed at a fixed point, but it is more likely that variations in station elevation contributed to the covariances computed previously. Other factors could have influenced the results, since the samples are small.

Table IX presents the linear correlation coefficients among the variables listed in Table VI. This presentation is the simplest method of portraying relationships of variables in time. Correlation coefficients that contain spurious correlation are placed in parentheses; most of the remaining coefficients are not significantly large. The one exception, and a few other features, are discussed below.

The most significant feature was the high correlation between the outgoing infrared flux at 100 mb and the infrared cooling (or flux divergence) of the entire atmosphere below that level. The correlation coefficient ranged between 0.90 and 0.97 at all stations for all cloud conditions. At first glance it may not seem so unusual since the outgoing flux is one of four components of the cooling, but in all previous computations of this type we have never achieved such high correlations. In fact, previous computations led us to believe that the high correlations measured by Sabatini and Suomi[20] with the radiometersonde were restricted in application. The present flux computations differ from our earlier ones in that the present flux model is an improved version and also we may have been more fortunate in properly modeling the clouds (at least the surface observers reported in the same way at a given station). However, it is difficult to reconcile the improvement in correlation (from around 0.5 to over 0.9) on the basis of these possibilities. It seems more likely that the change resulted from data-handling procedures; here we correlated the variables in time from a fixed location, rather than

Table IX

CORRELATIONS BETWEEN SELECT VARIABLES
16-30 JUNE 1966, PACIFIC STATIONS

(Symbols defined in Table V. Spurious correlations appear in parentheses.)

(a) Shemya

	T1	T2	T3	T4	R(G,5)	R(5,1)	R(G,1)	E(G,5)	E(5,1)	E(G,1)	E(2,.1)	F_N(G)	F_U(1)	Q(5,2)
T2	.57													
T3	.65	.29												
T4	(.75)	(.95)	(.39)											
R(G,5)	.58	.40	.33	.52										
R(5,1)	-.54	-.67	-.29	-.64	-.17									
R(G,1)	.46	.63	.16	.60	(.54)	(-.81)								
E(G,5)	-.07	.57	-.33	.40	.11	-.50	.49							
E(5,1)	.53	.35	.44	.39	.50	-.48	.50	.33						
E(G,1)	.00	.59	-.26	.43	.17	-.54	.53	(.99)	(.45)					
E(2,.1)	.55	.25	.31	.31	.43	-.48	.44	.37	.89	.47				
F_N(G)	-.08	.26	.01	.25	-.36	.19	-.46	.06	-.38	.01	-.39			
F_U(1)	.47	.83	.18	.79	.44	-.83	.91	.61	.40	.63	.34	-.06		
Q(5,2)	-.75	-.36	-.41	-.55	-.42	.61	-.50	-.04	-.32	-.08	-.36	.15	-.50	
Q(G,1)	-.02	-.47	.12	-.40	-.02	.55	-.47	-.70	-.19	-.68	-.09	-.15	-.61	(.42)

Table IX (continued)

(b) Adak

	T1	T2	T3	T4	R(G,5)	R(5,1)	R(G,1)	E(G,5)	E(5,1)	E(G,1)	E(2,.1)	F_N(G)	F_U(1)	Q(5,2)
T2	.56													
T3	.68	.08												
T4	(.69)	(.98)	(.21)											
R(G,5)	-.00	.53	-.34	.43										
R(5,1)	.16	-.52	.39	-.40	-.83									
R(G,1)	.30	.67	.13	.64	(.72)	(-.73)								
E(G,5)	-.00	.37	-.51	.35	.20	-.13	.10							
E(5,1)	.23	-.18	-.03	-.09	-.35	.49	-.39	.49						
E(G,1)	.03	.31	-.47	.31	.13	-.05	.03	(.99)	(.60)					
E(2,.1)	.32	.26	.25	.33	-.39	.37	.02	.42	.52	.46				
F_N(G)	.26	.31	-.22	.35	-.13	.14	-.20	.73	.60	.76	.46			
F_U(1)	.39	.79	.04	.77	.67	-.68	.93	.38	-.17	.32	.20	.17		
Q(5,2)	-.19	-.63	.06	-.60	-.55	.74	-.77	-.09	.48	-.01	.06	.00	-.77	
Q(G,1)	-.22	-.44	.02	-.47	-.02	.15	-.31	-.53	-.22	-.52	-.52	-.68	-.56	(.40)

(c) Wake

	T1	T2	T3	T4	R(G,5)	R(5,1)	R(G,1)	E(G,5)	E(5,1)	E(G,1)	E(2,.1)	F_N(G)	F_U(1)	Q(5,2)
T2	.86													
T3	.74	.78												
T4	(.91)	(.99)	(.77)											
R(G,5)	.90	.89	.79	.91										
R(5,1)	-.40	-.24	-.36	-.26	-.60									
R(G,1)	.91	.96	.80	.97	(.96)	(-.35)								
E(G,5)	-.07	.33	-.10	.24	.14	.09	.20							
E(5,1)	.27	.53	.47	.48	.44	-.20	.45	.26						
E(G,1)	.13	.55	.25	.46	.38	-.08	.41	(.77)	(.81)					
E(2,.1)	.38	.28	.58	.31	.41	-.29	.37	-.42	.02	-.24				
F_N(G)	.56	.71	.56	.67	.68	-.45	.64	.40	.52	.59	.25			
F_U(1)	.87	.96	.79	.95	.95	-.42	.96	.29	.52	.51	.37	.83		
Q(5,2)	-.82	-.67	-.69	-.71	-.90	.74	-.78	.19	-.45	-.18	-.50	-.58	-.79	
Q(G,1)	-.66	-.71	-.40	-.73	-.68	.39	-.66	-.27	-.39	-.42	-.35	-.77	-.76	(.64)

Table IX (concluded)

(d) Eniwetok

	T1	T2	T3	T4	R(G,5)	R(5,1)	R(G,1)	E(G,5)	E(5,1)	E(G,1)	E(2,.1)	F_N(G)	F_U(1)	Q(5,2)
T2	.89													
T3	.84	.92												
T4	(.92)	(.99)	(.92)											
R(G,5)	.86	.86	.78	.88										
R(5,1)	-.05	.04	.06	-.02	-.18									
R(G,1)	.88	.92	.83	.92	(.95)	(.04)								
E(G,5)	-.70	-.38	-.40	-.42	-.49	-.04	-.49							
E(5,1)	-.32	-.19	-.28	-.18	-.18	-.10	-.22	.61						
E(G,1)	-.63	-.35	-.40	-.38	-.42	-.07	-.44	(.96)	(.81)					
E(2,.1)	.16	.21	.07	.20	-.08	.18	.09	-.02	.02	-.01				
F_N(G)	.75	.78	.75	.79	.67	-.11	.77	-.40	-.26	-.39	.24			
F_U(1)	.88	.92	.85	.92	.90	-.01	.97	-.49	-.25	-.45	.16	.90		
Q(5,2)	-.71	-.69	-.63	-.73	-.89	.44	-.80	.40	.16	.35	.22	-.69	-.80	
Q(G,1)	-.72	-.71	-.84	-.71	-.64	.00	-.67	.51	.57	.58	.11	-.73	-.73	(.60)

(e) Ponape

	T1	T2	T3	T4	R(G,5)	R(5,1)	R(G,1)	E(G,5)	E(5,1)	E(G,1)	E(2,.1)	F_N(G)	F_U(1)	Q(5,2)
T2	.97													
T3	.92	.91												
T4	(.98)	(1.00)	(.92)											
R(G,5)	.12	.10	.09	.11										
R(5,1)	-.51	-.50	-.40	-.48	-.38									
R(G,1)	.38	.35	.19	.34	(-.28)	(-.59)								
E(G,5)	.13	.05	.15	.07	.24	-.41	-.17							
E(5,1)	.01	.08	-.16	.04	-.14	-.02	.23	-.10						
E(G,1)	.12	.09	.05	.08	.15	-.38	-.03	(.86)	(.42)					
E(2,.1)	.68	.70	.64	.69	.00	-.31	.26	.20	.47	.43				
F_N(G)	.65	.67	.68	.69	-.05	-.16	-.01	.08	-.37	-.11	.10			
F_U(1)	.63	.61	.47	.60	-.28	-.61	.90	-.11	.05	-.07	.29	.43		
Q(5,2)	-.03	-.13	.15	-.09	.35	.23	-.47	.23	-.51	-.05	-.01	-.01	-.43	
Q(G,1)	-.44	-.37	-.12	-.37	-.37	.36	-.23	-.04	-.24	-.16	-.20	-.06	-.23	(.26)

correlating in space from a number of stations at a fixed time. The latter procedure permits the introduction of errors due to boundary variability (especially height), instrumental differences, difference in solar exposure, and differences in base-line checks, all within a given data sample. The high correlation found in this study reaffirms the original contention that a remote measurement of the outgoing flux can also be used as a local estimate of the total infrared cooling.

The spectrally-broad Channel 4 includes the spectral regions covered by each of the other channels and some inter-correlation should exist. Since the bulk of the Channel 4 response arises from the same region to which Channel 2 responds, a high correlation between T2 and T4 is expected. However, the correlation is so high that Channel 2 can be construed to contain all the essential information in Channel 4; Channel 4 would serve a more useful purpose if it was replaced with an ozone channel. In fact, the computed outgoing flux at 100 mb is correlated even slightly higher with Channel 2 than with Channel 4, whereas the net flux at the surface is correlated to about the same extent with both.

T2 also is highly correlated with T1 and T3 in the tropics; however, over the Aleutians a very pronounced deterioration in the correlation between T2 and T3 occurs. Probably, this anomaly is associated with the fact that T3 (just as T2) is correlated fairly well with the outgoing flux in the tropics, but not over the low overcast conditions in the Aleutians. The implication is that the tropical cloudiness was correlated with the temperature and moisture of the upper troposphere (and lower stratosphere), but the polar stratosphere was not linked to the cloud variations. It is interesting to note that at a given station the correlation between T3 and E (2, 0.1) is generally not marked, but in a meridional sense the relationship is clear.

The negative correlation between T1 and Q(5,2) in the tropics is clearly related to the amount of high cloud, with the smallest absolute correlation occurring with the maximum amount of cirrus. Generally, Q(5,2) shows a better correlation with the radiative cooling terms and the outgoing flux than does Q(G,1), the total precipitable water. The relationship between Channel 2 and the radiative cooling depends on the cloudiness. At the clearest stations, Wake and Eniwetok, the correlation between T2 and R(G,1), for example, is high. The correlation deteriorates over the cloudier Ponape; the negative correlation in the upper troposphere becomes more dominant as the surface is screened (reduced cooling below clouds, more above). Over the cloudy Aleutians, the reversal in sign of the correlation coefficient from the lower to the upper troposphere is apparent, just as it was in the earlier study. When days with low overcast only were examined, it was found that the highest absolute correlation did not occur with the lower boundary at the top of the cloud. The correlation of T2 with the total infrared cooling always was positive and largest when the correlation between T2 and the outgoing flux was largest.

V ANALYSES FOR CENTRAL UNITED STATES

A. Solar Absorption

Atmospheric radiation computations in this study were restricted to infrared raidation, although solar absorption had been estimated in an earlier study.[20] Instead of computing the atmospheric solar absorption, a brief study was made of concurrent surface and satellite measurements of solar radiation. Fortunately, the relative distribution of reflectance measurements from Channel 5 at the time of Nimbus II passage was not subject to pronounced anisotropy (note the scattering angles in Fig. 3). Of course, uncertainty existed with respect to the representativeness of a single daytime measurement as an indicator of events for the entire sunlit day. The exploratory study of data was directed toward a preliminary determination on whether or not reflectance measurements from Nimbus II could be used to:

(1) Draw remote inferences on atmospheric solar absorption or the amount of solar radiation available for heating the surface

(2) Assist in the design of a satisfactory empirical technique for computing solar absorption

(3) Assist in the inference of total precipitable water.

The amount of solar radiation available for heating the surface is an important component of the surface heat budget, especially because of the difficulty in inferring the surface heat budget itself from remote measurements alone.

Although Channel 5, unlike the infrared channels, did not have an onboard calibration check, the results of Raschke[8] suggest that serious degradation problems did not exist. Past analyses of albedo, based on reflectance measurements from TIROS satellites, usually appeared to be low even after corrections for apparent degradation. However, the estimates also could have been lowered as a result of sampling bias (anisotropy) and an overestimate of the solar constant. On the other hand, the original expectations of the albedo might have been somewhat excessive by virtue of an underestimate of solar absorption, including absorption by aerosols. Therefore, it is important to determine the absorption empirically for real atmospheric states.

The following definitions were adopted for parameters arising in the solar analysis:

t = time

Z = Solar zenith angle

Φ = Latitude

δ = Solar declination

H_s = Hour angle at sunrise or sunset = $\cos^{-1}$ [$-\tan \Phi \tan \delta$]

R_5 = Channel 5 reflectance

A_E = Albedo of earth and atmosphere

a = Surface albedo

F_I = Solar flux normal to the sun at the top of the atmosphere (taken here as 116.4 cal cm^{-2} hr^{-1})

Q_I = Incoming solar radiation at top of atmosphere = $F_I \int \cos Z \, dt$

Q_R = Reflected solar radiation at top of atmosphere = $A_E Q_I$

Q_G = Downward solar radiation measured at the ground

Q_A = Solar radiation absorbed by atmosphere = $Q_I - Q_R - (1-a)Q_G$

q_A = Fractional absorption of atmosphere = Q_A/Q_I

q_T = Fractional transmittance of atmosphere = Q_G/Q_I.

For each U.S. station with insolation measurements taken concurrently with the Nimbus II swaths near 1800 GMT on 26 and 27 June 1966, tabulations were made of R_5, of Q_G for the hour centered at the time of the Nimbus pass, and of Q_G for the entire day. In addition Q_I was computed both for the hour centered at the Nimbus passage and for the entire day. The latter quantity is given by

$$Q_I(\text{day}) = F_I \frac{24}{\pi} [\sin \varphi \sin \delta H_s + \cos \Phi \cos \delta \sin H_s] .$$

Estimates of Q_A were obtained by setting $A_E = R_5$ and by assuming a value of 0.13 for a. Relative magnitudes of Q_A were not affected by the assumption on A_E, but could have been adversely affected by assuming a constant surface albedo (actually, three surface albedos were used but are not included in the listings). The surface albedo of 0.13 probably is a little low for the average value, but such an underestimate is compensated in part by a probable underestimate of A_E. In any case, the absolute magnitudes of Q_A cannot be verified. All of the results are tabulated in Table X. It was not possible to determine the total precipitable water, W, between the surface and 300 mb at 1800 GMT for all stations in this list.

Figure 8 compares the fractional transmittance q_T at time of satellite transit with the Channel 5 reflectance. A general quasi-linear relationship is evident, but most of the points cluster and scatter near the higher transmittance and lower reflectance. Nevertheless, Fig. 8 suggests that it might be possible to estimate q_T from satellite-observed reflectance. Figure 9 compares the fractional transmittance at the time of Nimbus II overflight with the average fractional transmittance for the entire sunlit day. In general, the relationship is good; the average transmittance at satellite time (near local noon) is somewhat larger than the daily transmittance because of the smaller solar slant path. Scatter in Fig. 9 was not clearly related to the zenith angle at satellite passage.

For comparison with satellite measurements, the total precipitable water between the surface and 300 mb was divided by the cosine of the solar zenith angle to give U, the slant path of precipitable water. In addition, for each station with an 1800 GMT measure of precipitable water, an abbreviated code was adopted to describe the sky cover at 1800 GMT. Figure 10 is a plot of Channel 5 reflectance and the slant path of precipitable water. A non-linear relationship is evident. However, a perplexing aspect of the plot is the clustering of relatively low values of Channel 5 reflectance for a wide range of sky covers. The tempting conclusion is that there is some error in the reflectance measurements. Although mosaics of satellite photographs of cloud cover were assembled, their quality was too poor for reproduction here. Nevertheless, local checks indicated compatibility between the cloud pictures and the surface observations of cloudiness.

Table X

SUMMARIES OF INCOMING, REFLECTED, TRANSMITTED, AND ABSORBED (ATMOSPHERIC) SOLAR RADIATION, 26-27 JUNE 1966

(Symbols defined in text)

(a) 26 June 1966

Station	Cos Z	R_5	Q_I	Q_G	Q_I(Day)	Q_G(Day)	Q_A	Precip. Water (ctm)	1800 GMT Clouds (Amounts: types)
Laramie	0.9205	22.2	107.2	60.1	1020	420	31.1		
Salt Lake City	0.8988	18.5	104.7	84.9	1019	798	11.4	1.538	Clear
Stillwater,Okla.	0.9659	22.9	112.7	50.4	1016	475	43.1		
Ames,Ia.	0.9455	19.0	109.4	69.1	1019	612	28.5		
Ruston,La.	0.9833	17.8	114.1	75.8	1008	556	27.9		
Madison,Wisc.	0.9397	23.0	108.7	66.7	1021	592	25.7		
Fort Worth	0.9763	18.0	114.0	83.4	1008	694	20.9	2.529	0.8: Sml Cu,Ci,Cs
El Paso	0.9511	52.0	111.2	16.5	1009	209	39.0	3.327	1.0: Sc,Ns,Rain
Brownsville	0.9877	18.1	115.4	82.5	989	569	22.7		
Bismarck	0.9063	15.0	103.5	77.4	1018	718	20.7	1.472	0.1: Sc
Albuquerque	0.9397	24.0	110.2	88.8	1016	692	6.5	1.748	0.3: Sml Cu,Ac,Ci
North Omaha	0.9455	17.5	109.8	89.2	1019	692	13.0	3.077	0.4: Ci
Great Falls	0.8660	17.0	100.5	71.6	1018	668	21.1	1.120	0.1: Sc,Ci
Columbia, Mo.	0.9613	28.2	111.2	77.8	1019	525	12.1	3.858	0.9: Ac, As
Lake Charles,La.	0.9890	12.8	114.7	81.4	1003	647	29.2	2.634	Clear: haze
Dodge City	0.9537	23.3	109.0	76.0	1018	590	17.5	2.997	0.8: Sml Cu,Ac,Ci
Page, Ariz.	0.9135	26.2	106.5	69.2	1018	504	18.4		
Tucson	0.9272	20.5	108.1	79.1	1010	696	17.1	2.607	0.1: Sml Cu
Ely	0.8870	23.8	105.5	80.9	1020	763	10.0	0.863	Clear
Phoenix	0.9205	20.5	107.7	69.1	1013	615	25.5		

Table X (concluded)

(b) 27 June 1966

Station	Cos Z	R_5	Q_I	Q_G	Q_I(Day)	Q_G(Day)	Q_A	Precip. Water (ctm)	1800 GMT Clouds (Amounts: types)
Laramie	0.8829	19.0	104.4	73.4	1020	685	20.7		
Salt Lake City	0.8480	20.0	99.4	80.0	1019	800	9.9	1.210	Clear
Stillwater,Okla.	0.9397	20.8	109.8	69.2	1016	648	26.8		
Ames, Ia.	0.9272	23.8	106.8	61.3	1019	492	28.1		
Ruston, La	0.9833	17.8	114.1	75.8	1008	556	27.9		
Madison,Wisc.	0.9336	18.3	108.7	82.5	1021	704	17.0		
Fort Worth	0.9511	18.7	111.0	85.1	1008	624	16.2	2.720	Clear
El Paso	0.9063	48.0	108.1	48.5	1009	468	14.0	3.765	1.0: Sc,Ns,Rain
Bismarck	0.8788	22.0	101.0	73.2	1018	546	15.1	2.174	0.3: Cb,Ac
Albequerque	0.8988	26.5	107.2	87.7	1015	762	2.5	2.509	0.3: T Cu,Ci
North Omaha	0.9239	40.0	107.1	56.3	1019	404	15.3	3.908	1.0: Sml Cu, Cs
Great Falls	0.8241	17.2	95.8	65.9	1018	598	22.0	1.137	0.4: Sc,Ci
Columbia, Mo.	0.9455	24.3	108.4	69.5	1019	534	21.6	3.722	1.0: T Cu,Ac
Lake Charles,La.	0.9703	15.0	111.6	75.7	1003	625	29.0	3.233	0.1: Sml Cu
Dodge City	0.9239	20.1	106.1	77.5	1018	649	17.4	3.183	0.8: T Cu, Ac
Nashville	0.9703	18.3	112.7	75.6	1016	585	26.3	2.993	0.5: Sml Cu,Haze

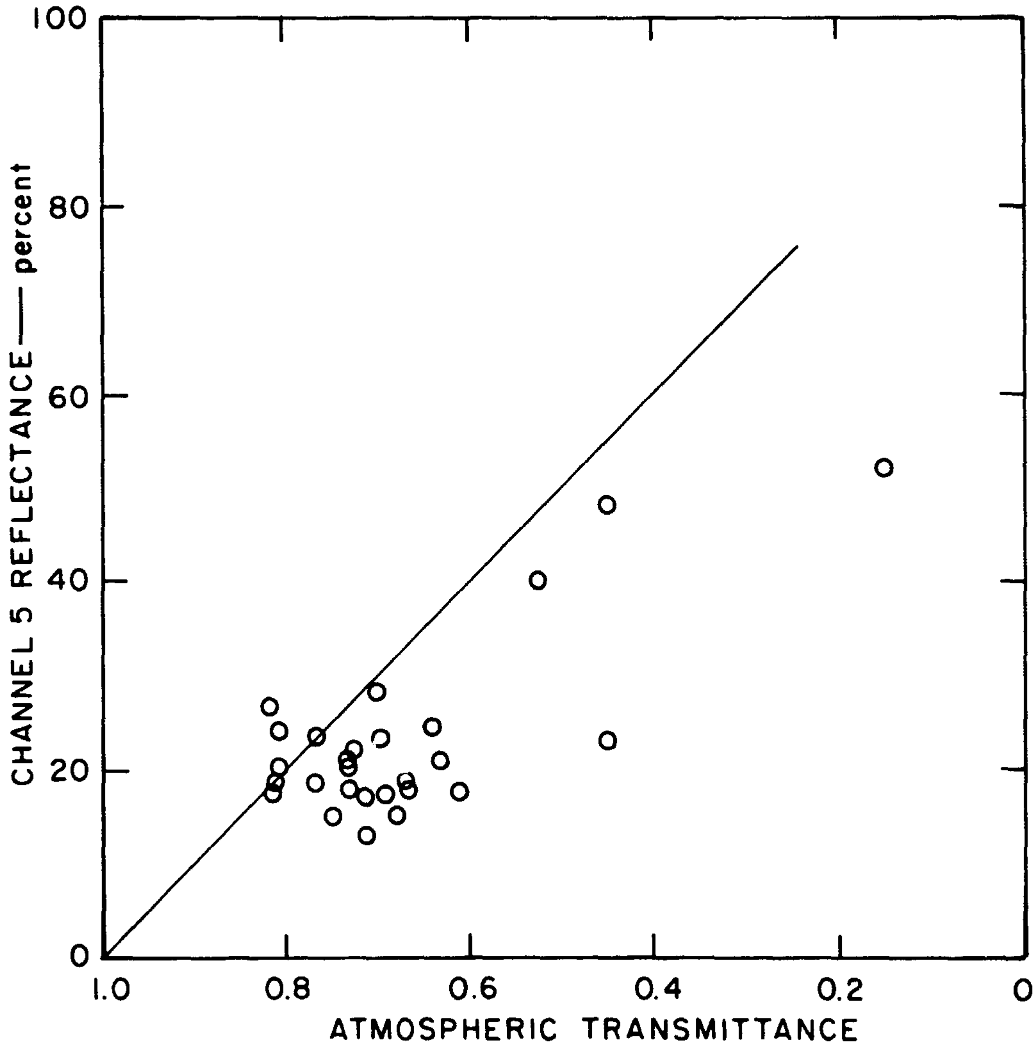

FIG. 8 ATMOSPHERIC SOLAR TRANSMITTANCES AND CHANNEL 5 (Nimbus II) REFLECTANCES AT SELECT U.S. STATIONS, 26-27 JUNE 1966

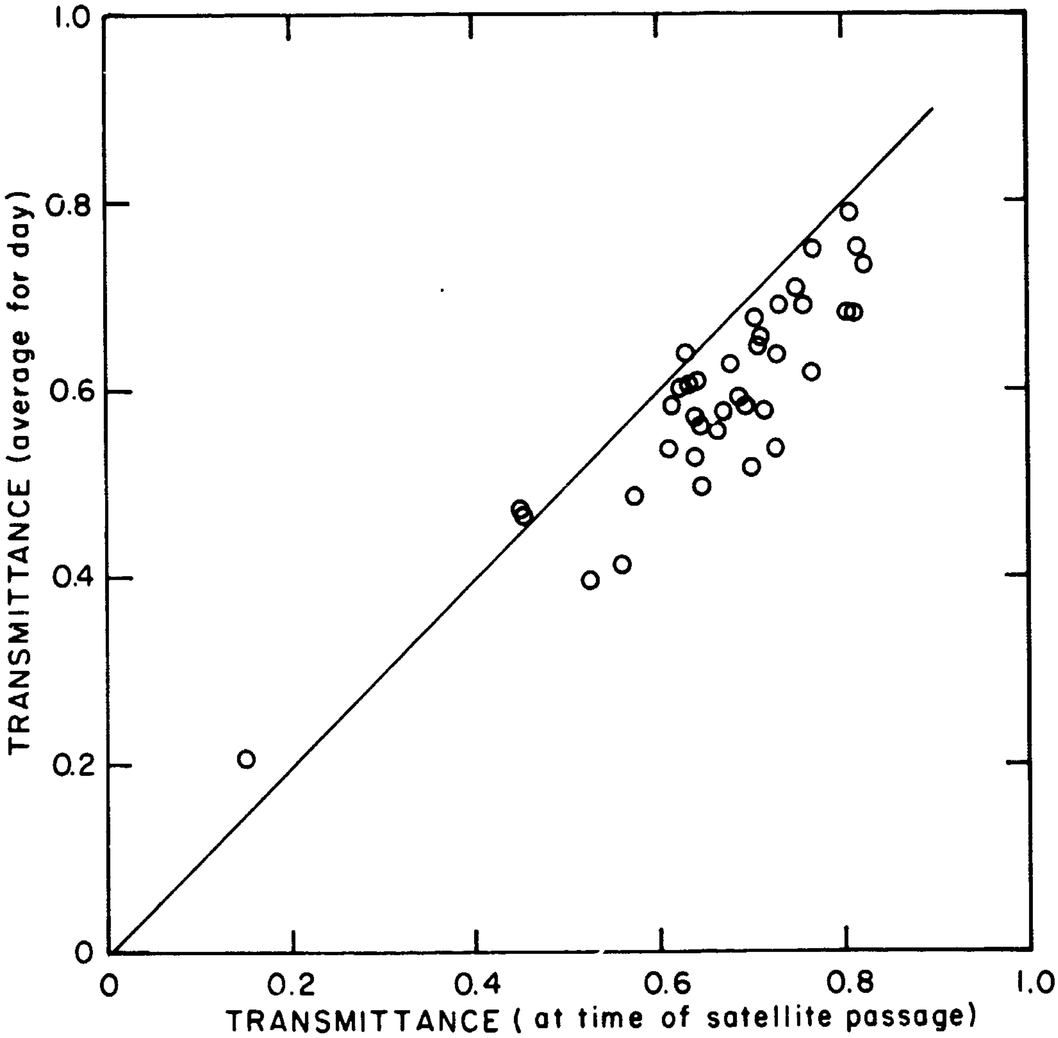

FIG. 9 COMPARISON OF HOURLY (at time of Nimbus II Pass) AND DAILY SOLAR TRANSMITTANCES AT SELECT U.S. STATIONS, 26-27 JUNE 1966

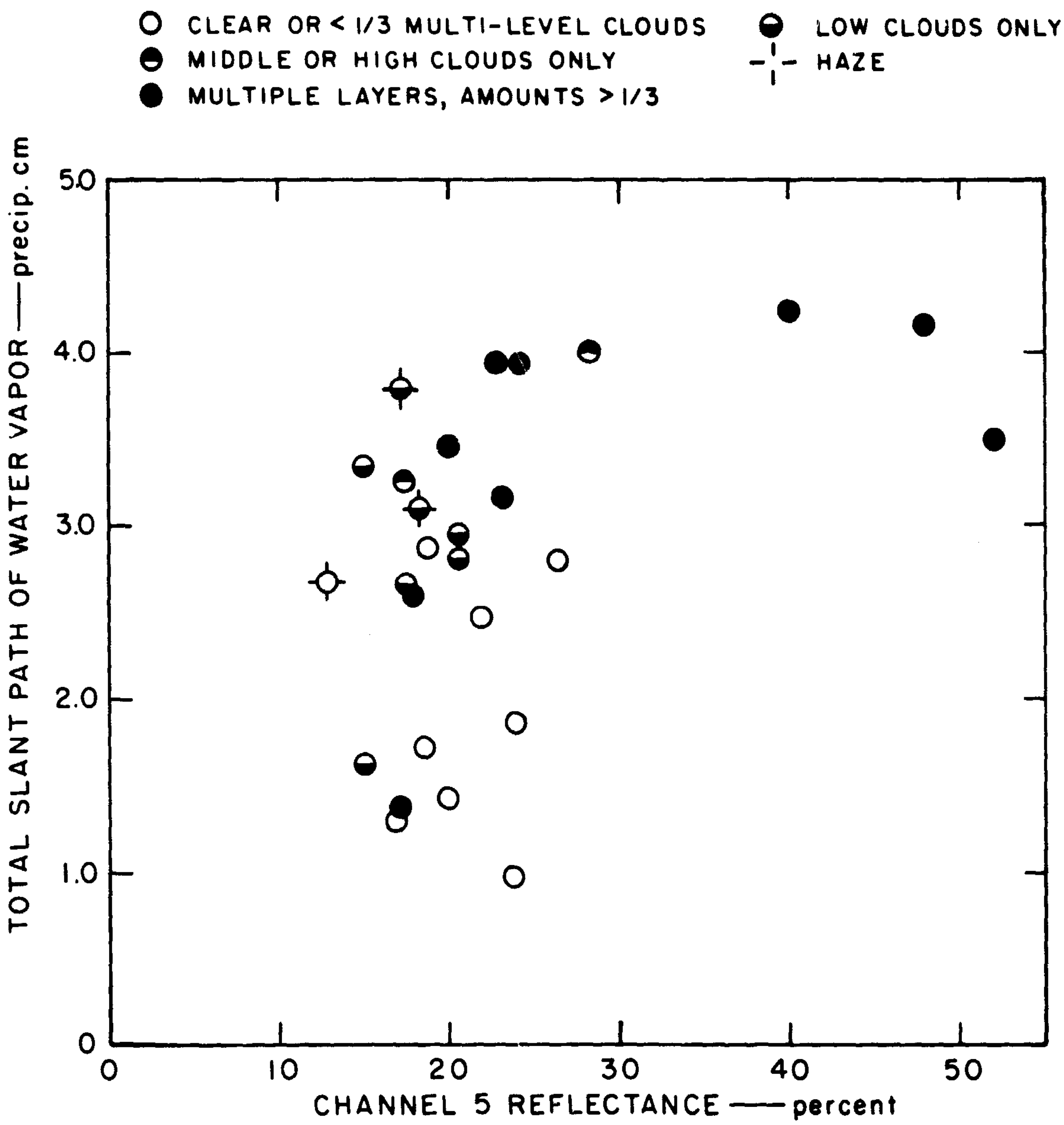

FIG. 10 CHANNEL 5 REFLECTANCES (Nimbus II) AND SLANT PATHS (Solar) OF PRECIPITABLE WATER AT SELECT U.S. LOCALITIES, 26-27 JUNE 1966

For the same stations in Fig. 10, the fractional absorption of solar radiation by the atmosphere was determined empirically from the observed solar data as described earlier. In addition, the total precipitable water was used to compute the solar absorption by two empirical formulas. The first formula, taken from Hanson et al.,[21] was devised statistically from other satellite data for all sky conditions:

$$q_a = 0.096 + 0.045 \sqrt{U} \ln U \quad .$$

The fractional absorption so computed is compared with the "observed" absorptance in the upper portion of Fig. 11. Because of the large scatter exhibited it is apparent that the statistical expression given above does not apply accurately on a local scale.

The fractional absorptance for clear skies was computed from a formula used previously:[22]

$$q_A \text{ (CLEAR)} = \exp \left\{ -2.39 + 0.775 \log U - 0.078 (\log U)^2 - 0.022 (\log U)^3 \right\} .$$

Although computations in the earlier study were extended to include cloudiness, it was decided here merely to compare the clear-sky computations with the observed absorptance (lower portion of Fig. 11).

Results of the comparison show that the computed absorptance for clear skies agrees with observation only for clear skies or high clouds. The two clear-sky computations that appear to be over-estimates are probably correct; the "observed" absorptance in these cases (Albuquerque) is underestimated because of the low surface albedo used. It is likely that the surface albedo should have been doubled. The one pronounced under-estimate of the computed absorptance for clear skies without haze actually was associated with a locality in which a significant increase in cloudiness was being observed in spite of the single-station report of clear at observation time. With low clouds only or with low and middle clouds the total solar absorption within the atmosphere increased significantly over the clear-sky absorption. Some uncertainty exists for multi-layered overcasts that include high clouds; there may even

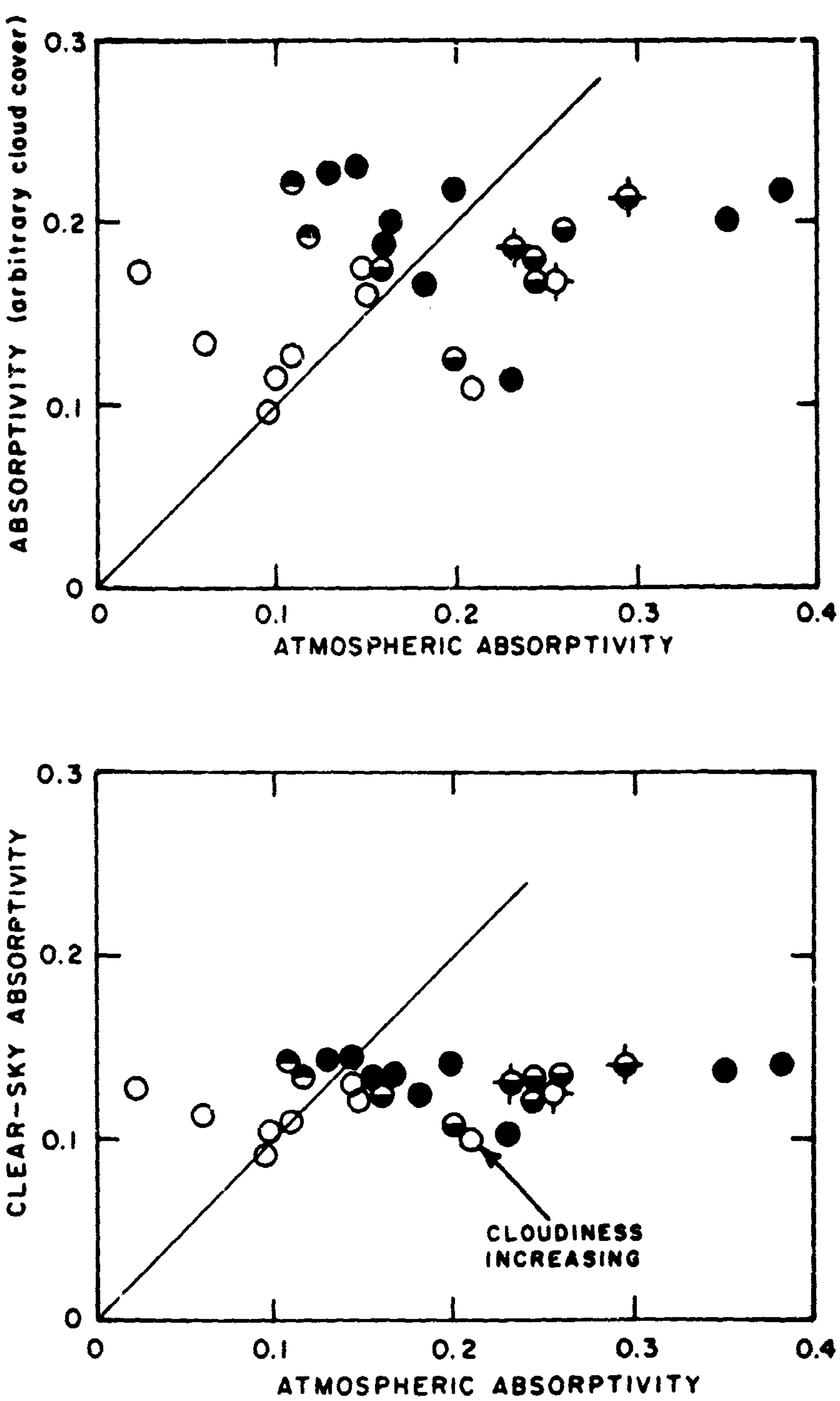

FIG. 11 COMPARISON OF ATMOSPHERIC SOLAR ABSORPTIVITY DEDUCED FROM SATELLITE AND SURFACE MEASUREMENTS WITH EMPIRICAL-ANALYTICAL ESTIMATES BASED ON PRECIPITABLE WATER FOR ARBITRARY CLOUD COVER (upper) AND FOR CLEAR SKIES (lower)

be a slight reduction in absorption if the high clouds are dense and extensive. In summary, if the general cloud conditions are known it appears that it should be possible to adjust a clear-sky computation empirically to yield the appropriate fractional absorptance. Furthermore, an expanded study of satellite and surface observations should produce good empirical estimates of the adjustment. Of course, it would be most helpful if the surface observations included both insolation and the surface albedo.

The few stations at which haze was reported had a significantly larger absorptance than that computed for clear skies. The implication of significant solar absorption by haze must be examined more extensively with new data.

B. Diurnal Temperature Change

On June 26 the northern plains were generally clear for almost 24 hours, and from noon of June 27 through the morning of June 28 the Eastern Texas-Louisiana area was clear. Although both areas appeared clear on satellite photographs, there were some surface reports of scattered cirrus, and scattered daytime cumulus were observed in the latter area. For both areas it was possible to obtain nighttime (midnight) and daytime (noon) distributions of Channel 2 temperatures. Also, for both areas it was possible to document the distribution of maximum and minimum temperatures for the appropriate periods from the many observations provided by cooperative observers. Maximum-minimum temperature ranges were analyzed over a 1.25-by-1.25-degree grid network because this grid size appeared to render a smoothed distribution that was spatially compatible with the mapped satellite data. Finally, standard surface observations of temperature at synoptic stations were summarized, in spite of the much poorer spatial coverage. A purpose of this study was to compare the Nimbus II Channel 2 temperature changes with the observed temperature changes at shelter height.

Statistics of radiometric measurements are affected by diurnal variations at or near the surface, and these variations are most pronounced during clear skies. Furthermore, maximum heat and water vapor exchanges at the surface usually are associated with relatively clear skies or with areas containing considerable convective activity. The potentially large diurnal range of surface temperature over land may be a useful parameter in conjunction with the available solar energy for analyses of the surface heat budget. Or, for statistical summaries of radiation data, the range of surface temperature provides some information on the bias that can result by summarizing radiometric data collected only once a day over land.

Figure 12(a) shows the distribution of the midnight-noon range of Channel 2 temperatures and the max-min temperature ranges over the northern plains. Except for southeastern South Dakota, where some cloudiness prevailed, there is generally good agreement between the two distributions. In some areas the range of radiometric temperature exceeded the observed max-min range; it is possible that the instrument shelters could have been situated in spots that do not experience the extreme temperature ranges. Channel 2 of Nimbus II was a relatively "clear" window channel, and thus responded largely to the actual surface temperature rather than the shelter-height temperature, but with some moderation due to water-vapor absorption. Since the range of surface temperature exceeds the range of shelter-height temperature, the good agreement in the distributions might be attributed to the fact that the satellite did not actually view the surface under the extreme conditions. When the much more sparsely populated temperature ranges corresponding to the times of satellite overflight [see Fig. 12(b)] are examined, it is apparent that the radiometric temperature range always exceeded the corresponding shelter-height temperature range, but with a similar relative distribution.

Figure 13 shows the midnight and noon surface observations of cloudiness over the northern plains. The principal difference between the surface reports is the increased number of observations of scattered cirrus in the daytime. Intermediate observations indicated that the sudden increase in cirrus was merely the result of improved viewing conditions during the sunlit day.

Figure 14 shows the distributions of observed temperature ranges for the Texas-Louisiana area, a region both warmer and more moist than

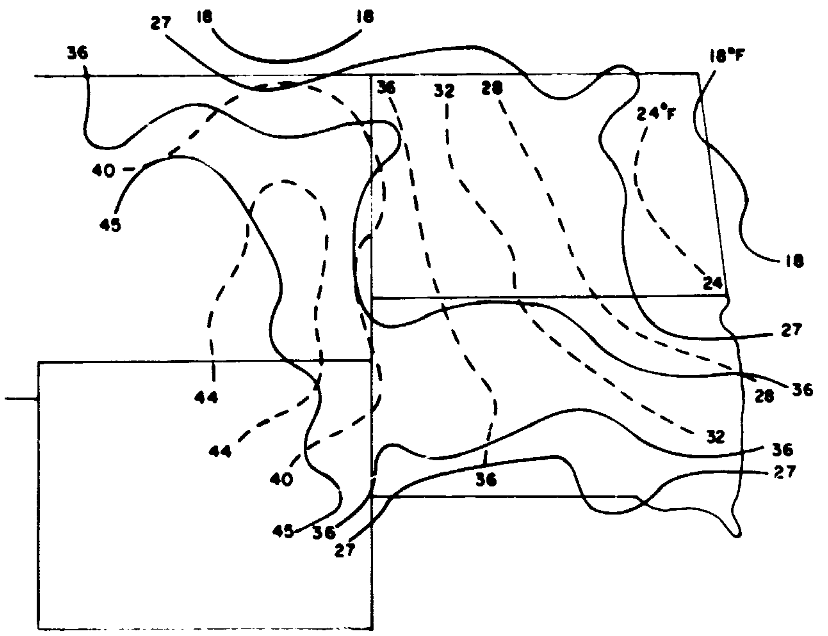

(a) CHANNEL 2 TEMPERATURE RANGE (solid) FOR NIMBUS II PASSES AT 0135CST AND 1155CST AND MAX-MIN TEMPERATURE RANGE AT SURFACE (dashed)

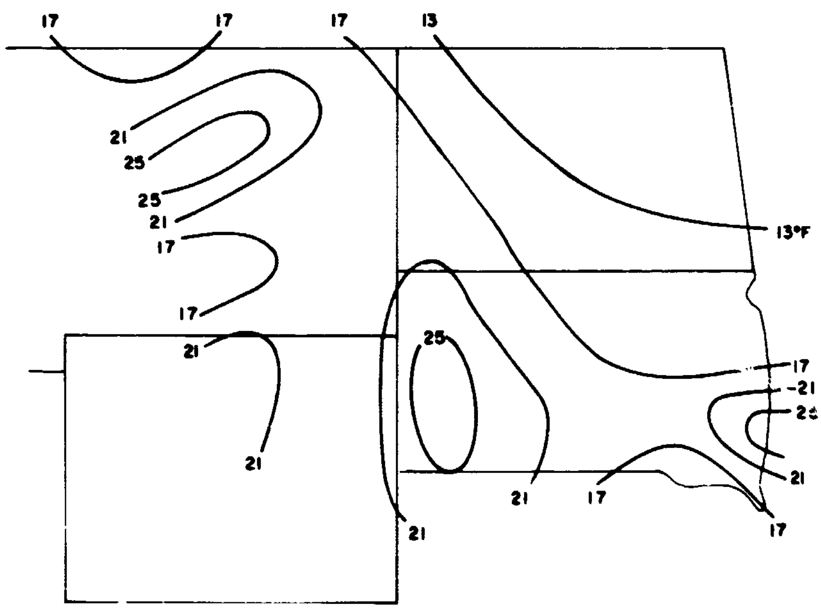

(b) OBSERVED TEMPERATURE RANGE AT SHELTER HEIGHT, 0000 CST TO 1200 CST

FIG. 12 OBSERVED TEMPERATURE RANGES AT SURFACE AND FROM CHANNEL 2 (Nimbus II) OVER THE NORTHERN PLAINS, 26 JUNE 1966

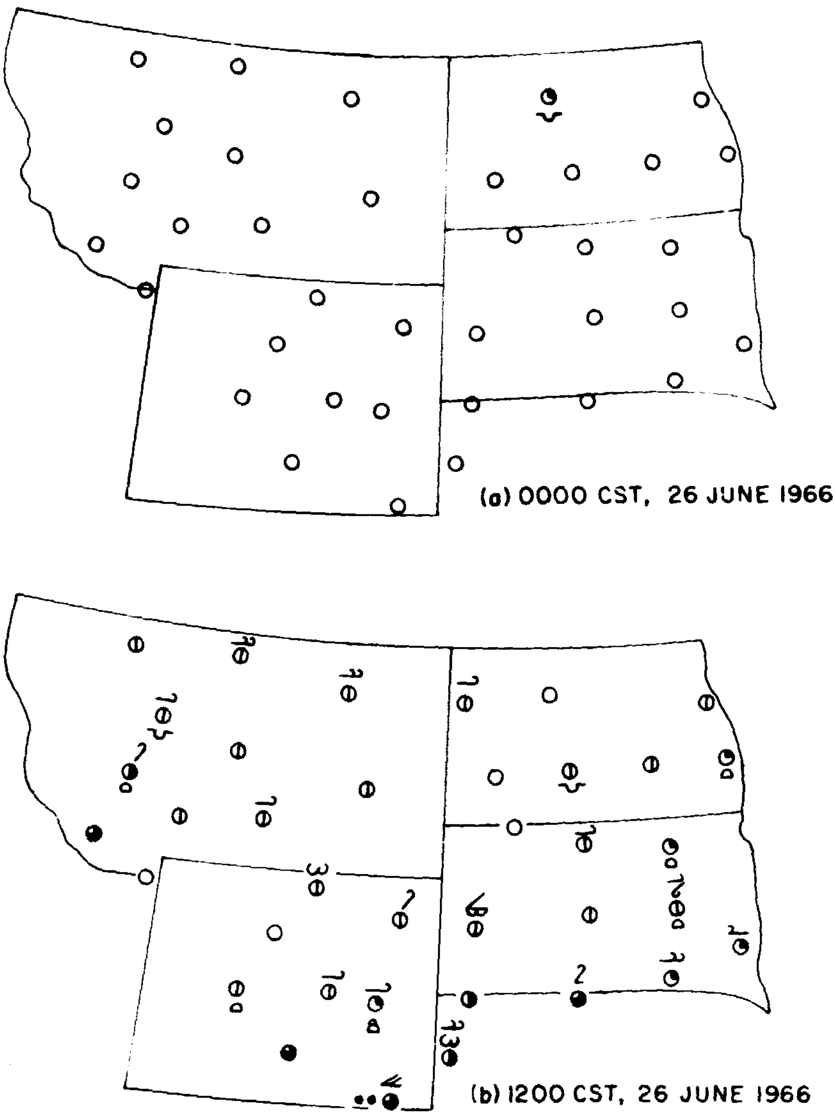

FIG. 13 SURFACE OBSERVATIONS OF SKY CONDITIONS FOR NIMBUS II PASSES OVER THE NORTHERN PLAINS

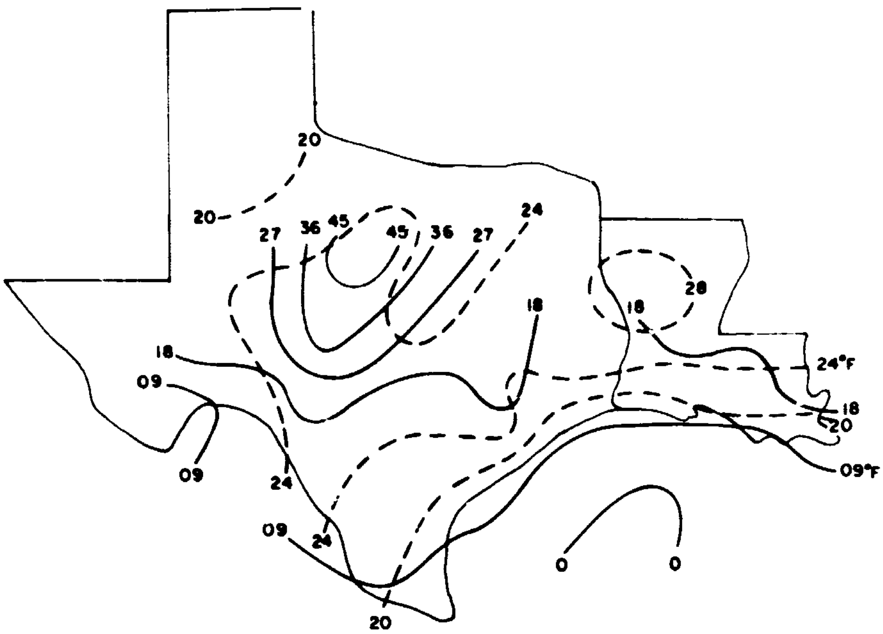

(a) CHANNEL 2 TEMPERATURE RANGE (solid) FOR NIMBUS II PASSES AT 1120 CST AND 0035 CST AND MAX-MIN TEMPERATURE RANGE AT SURFACE (dashed)

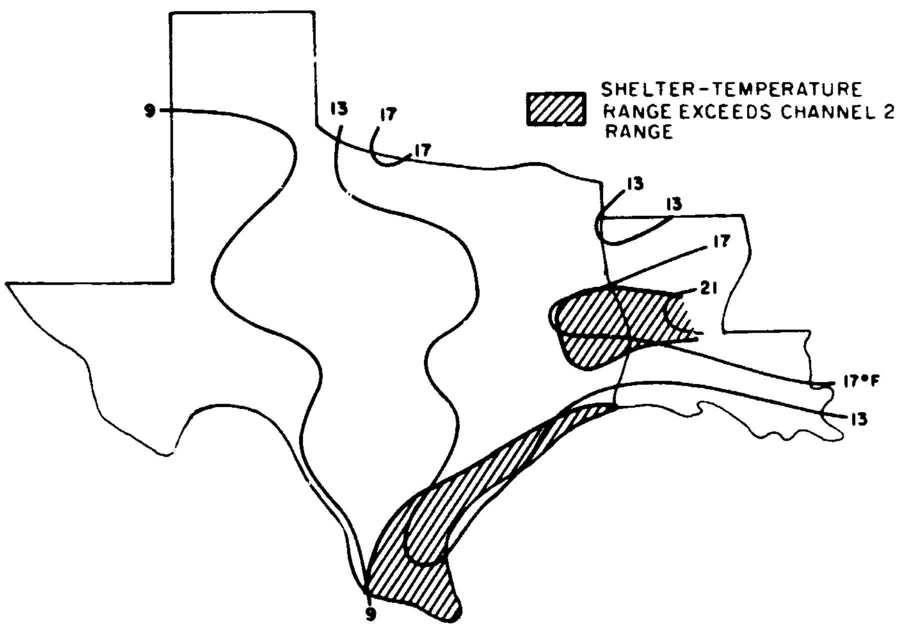

(b) OBSERVED TEMPERATURE RANGE AT SHELTER HEIGHT, 1200 CST TO 0000 CST

FIG. 14 OBSERVED TEMPERATURE RANGES AT SURFACE AND FROM CHANNEL 2 (Nimbus II) OVER TEXAS AND LOUISIANA, 27-28 JUNE 1966 the northern plains. Figure 15 shows the noon and midnight surface reports of cloudiness. Several important differences in results are evident. The analysis of temperature ranges was extended into the north-central area of Texas in spite of the existence of some cloudiness. In north-central Texas the observed range of radiometric temperature exceeds the observed max-min temperature range at the surface by more than three times. The explanation, on the basic of surface reports, is that the scattered daytime cirrus clouds increased to a broken cover at night. Thus, the radiometric view at night was of a considerably colder background than would have been the case if the cloud cover had remained constant (with a diurnal change in surface temperature). Obviously, the cirrus clouds had a pronounced effect on the radiometric response.

In the areas of Texas-Louisiana with daytime cumulus clouds, the range of radiometric temperature was smaller than the observed max-min range at the surface. In part, this deficit was due to the thermal screening of the surface by cumulus clouds from the satellite. However, the moist and hazy conditions in the area (even in the absence of clouds) increased the atmospheric response of Channel 2, reduced the temperature discrepancy between the actual surface and shelter height, and probably shifted the max-min phase. In fact, Fig. 14(b) shows that in some areas the range of radiometric temperatures was even less than the corresponding temperature range at shelter height. A separate study of daytime and nighttime clear-sky data showed that the Channel 2 temperature was persistently lower than the shelter temperature at night, and in the daytime was frequently larger than the shelter temperature, as anticipated. However, over the very moist conditions of the southeastern U.S. bordering the Gulf of Mexico, the daytime departures also were negative.

To summarize, the radiometric data provide a measure of surface-temperature change in clear areas, but are especially sensitive to cirrus clouds that may not be detected adequately. However, there are latitudinal (or climatic) differences in the relationship as a result of variations in atmospheric moisture and temperature discontinuities at the surface. The range of surface temperature, together with an estimate of the radiational energy available at the surface, could provide an indication of the net latent-plus-sensible-heat exchange at the surface, but it may not be possible to separate the latent heat exchange from the sensible heat exchange. Furthermore, the wind speed, convection, and advection all must be considered, as well as departures of temperature ranges from the anticipated normals. It appears that the cloud and wind information that could be inferred from an earth-synchronous satellite would be helpful.

C. Radiometric Data in Infrared Absorption Bands

To conclude the study of U.S. data, some analysis of the carbon dioxide (Channel 3) and water vapor (Channel 1) data for 26 and 27 June 1966 was conducted in order to evaluate direct interpretations in terms of atmospheric structure. Data samples were smaller than for the studies involving surface data simply because the multichannel satellite data ordered covered fewer of the localities with 1800 GMT radiosondes. The response characteristics of Channel 3 on Nimbus II were such that the principal contributing portion of the atmosphere extended from about the 300-mb level up to the 10-mb level with a peak contribution near 100 mb. Thus the mean virtual temperature (or thickness) above about 300 mb can be expected to be related to the Channel 3 temperature. This relationship is verified in the upper portion of Fig. 16.

Since the temperature of the region just above the tropopause is warmer than the same elevation just below a higher tropopause, it can be anticipated that the Channel 3 temperature will increase as the base of the tropopause lowers Of course, some difficulty may be encountered in specifying the base of the tropopause. The lower portion of Fig. 16 shows that the Channel 3 temperature is related to the pressure at the base of the tropopause and, consequently, is useful in specifying the gross temperature structure. Scatter in Fig. 16 is due in considerable part to the subjectivity in specifying the tropopause base; independent estimates showed an improved relationship with less scatter. It appears that the extreme pressures for the lowest tropopause bases were overestimated. Subsequent efforts have shown that it would be possible to specify a tropopause base objectively from a computer routine in the future.

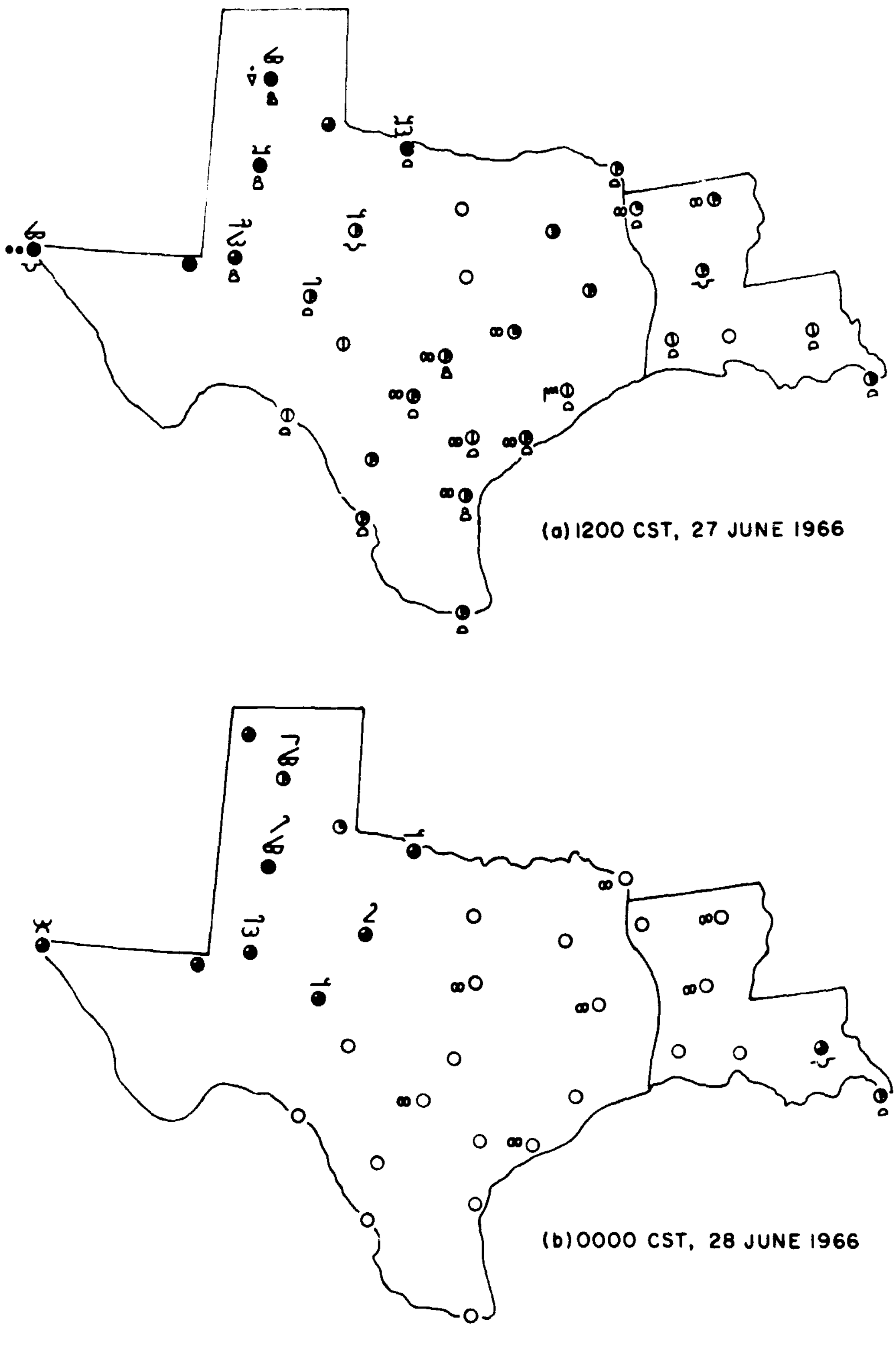

FIG. 15 SURFACE OBSERVATIONS OF SKY CONDITIONS FOR NIMBUS II PASSES OVER TEXAS AND LOUISIANA

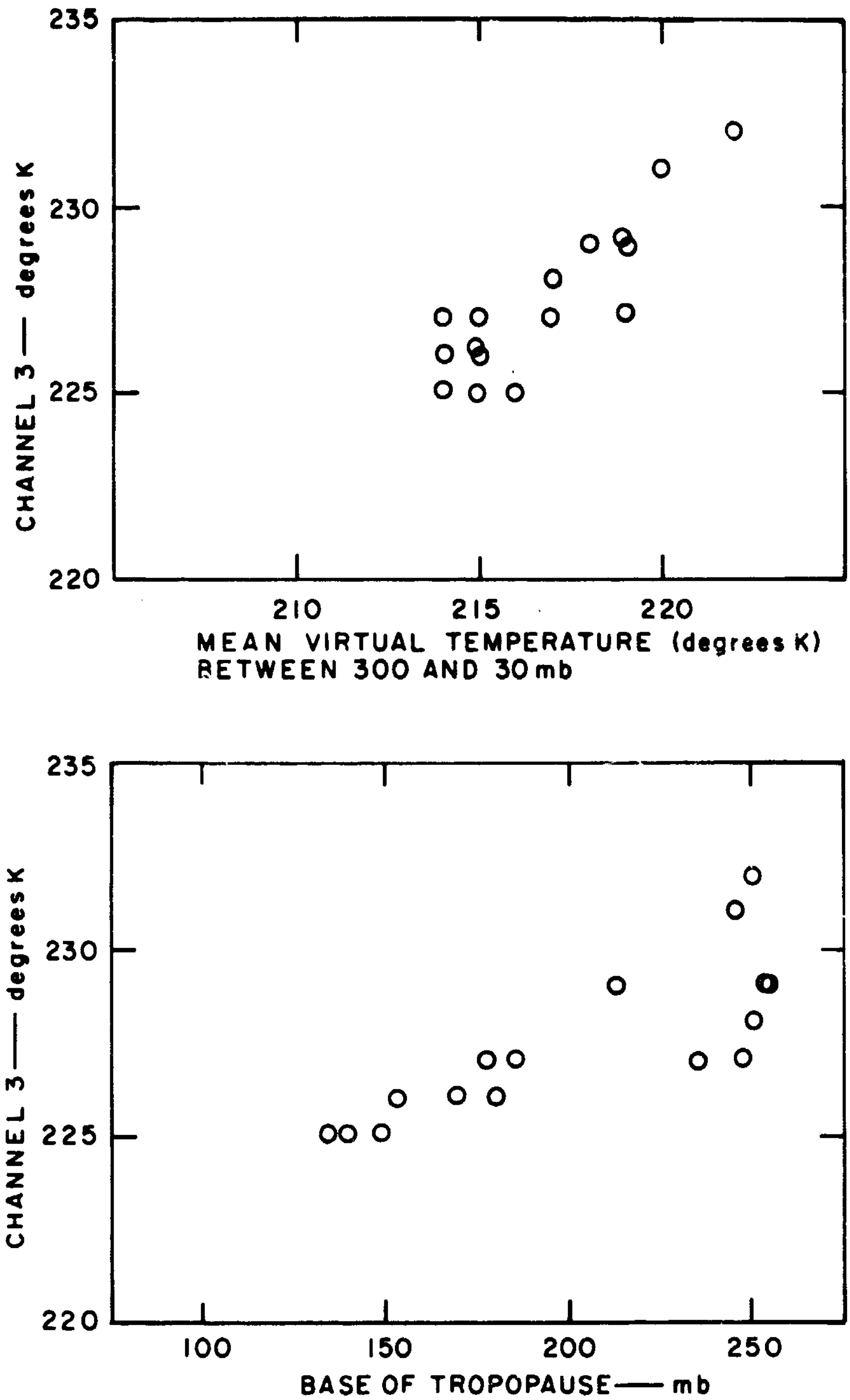

FIG. 16 COMPARISON OF NIMBUS II CHANNEL 3 TEMPERATURE WITH MEAN VIRTUAL TEMPERATURE (upper) AND BASE OF TROPOPAUSE (lower) FOR SELECT U.S. SOUNDINGS, 26-27 JUNE 1966

Contributions from water vapor to the response of Channel 1 arise primarily from the upper half of the troposphere. Since most interest is in means for specifying the water vapor density in this region, the satellite data from Channel 1 were compared with the slant path of precipitable water between 500 mb and 300 mb. In this comparison the slant path was determined as the precipitable water in the layer divided by the cosine of the radiometric zenith angle (rather than the solar zenith angle as used earlier). For the small data samples involved in the comparison, there appeared to be little difference between the use of the radiometric slant path for water vapor and the application of a limb correction to Channel 1 temperatures; therefore, the more objective slant paths were used. The upper portion of Fig. 17 compares the upper-layer slant path of water vapor with the departure of the Channel 1 temperature from the mean virtual temperature of the upper troposphere. Data points associated with significant amounts of cirrus clouds are indicated with crosses because Channel 1 responds to the cirrus particles as well as the water vapor. The relationship is poor, although a trend is discernible, especially if the cirrus cases are ignored. No significant improvement was achieved by introducing Channel 2 temperatures or the relative humidity. However, the lower portion of Fig. 17 shows that the Channel 1 temperature alone (rather than as a departure from existing average temperature) relates somewhat more directly with the water-vapor slant path when the cirrus cases are ignored. Furthermore, the lowest Channel 1 temperatures are the ones associated with cirrus and could, in fact, be used as an aid in the identification of cirrus.

An examination of Channel 4 temperatures, in response to broad spectral coverage, failed to reveal any simple direct application on a local scale. As noted earlier, Channel 2 and the other channels contain most of the information available from Channel 4, except that ozone does affect the Channel 4 response. Attempts to combine Channel 4 temperatures and Channel 2 temperatures to deduce gross changes in stability were not successful; both the stability and details of the profile of radiative cooling probably can be determined best from remotely determined temperature profiles when clouds can be handled successfully.

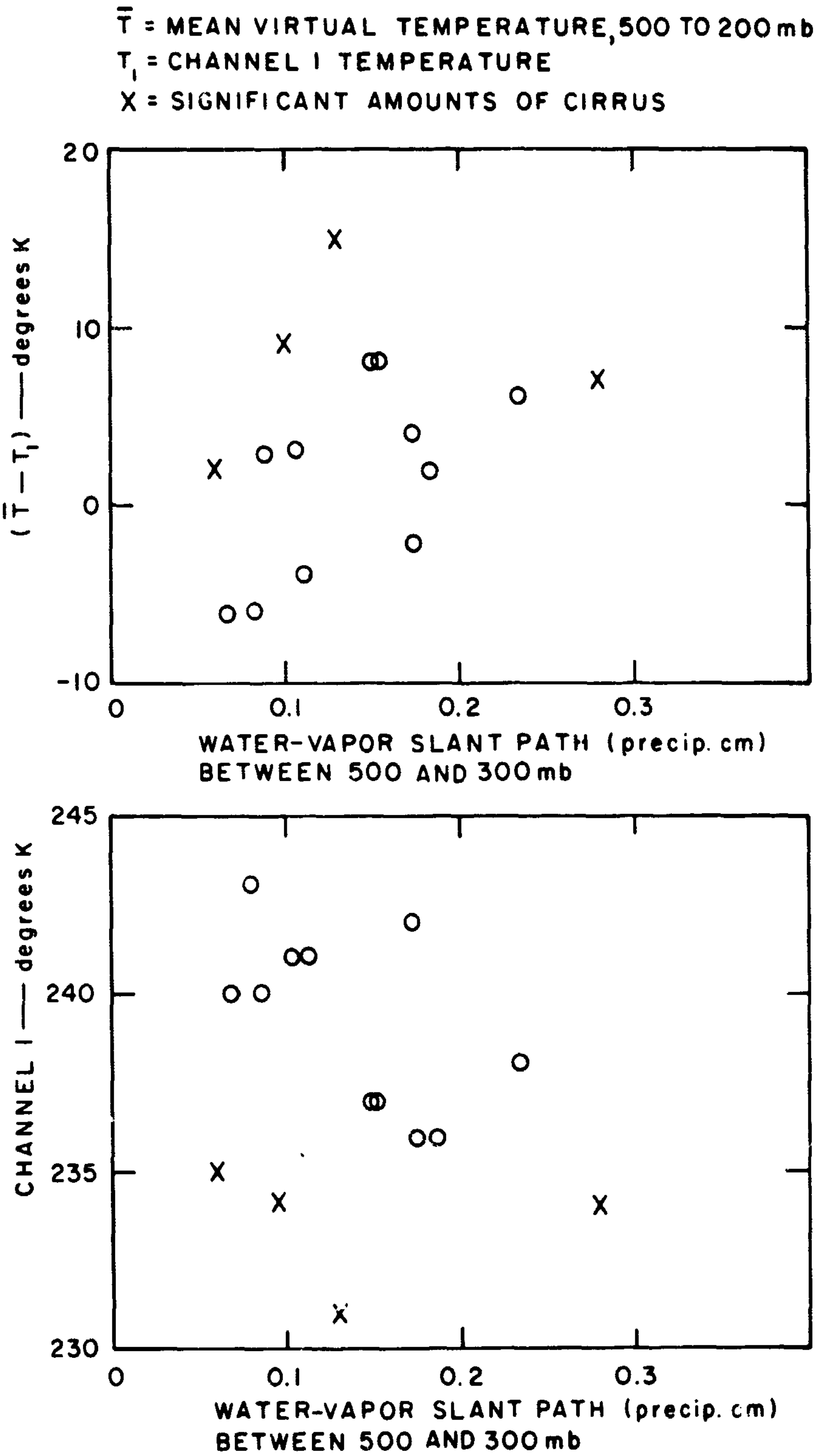

FIG. 17 COMPARISON OF WATER-VAPOR SLANT PATH FOR NIMBUS II VIEWS OF UPPER TROPOSPHERE WITH CHANNEL 1 TEMPERATURE (lower) AND DEPARTURE FROM MEAN VIRTUAL TEMPERATURE (upper)

PRECEDING PAGE BLANK NOT FILMED.

VI AIR-SEA HEAT EXCHANGE

A. Local Data

A study of Nimbus II radiometric data over the oceans was initiated by selecting multi-resolution Mercator composite mappings (1:20 million scale) over the Pacific Ocean for 16 and 17 June 1966. Preliminary objectives were:

(1) To ascertain the scale sensitivity of averages of mapped values

(2) To look for evidence of diurnal variations in cloudiness over the oceans

(3) To compare Channel 2 and Channel 5 data with independent analyses of the air-sea heat exchange on a local scale.

The mapped Channel 2 temperatures and Channel 5 reflectances were averaged in approximate 5-, 10-, and 20-degree squares centered along latitude 40°N (close to shipping lanes). These scales included 4, 24, and 80 grid point values, respectively. Figure 18 shows the variation of the averages for daytime on 16 June 1966; the anticipated negative correlation between data from the two channels is apparent. It was concluded that the 5-degree average retains most of the significant variance of local features; the smoother 10-degree average contains the significant features of synoptic variations. The still-smoother 20-degree averages may be acceptable for global summaries, but phase differences with local or synoptic features are apparent.

Figures 19 and 20 show the nighttime and daytime Channel 2 maps for 16 and 17 June, respectively. In the absence of unusual instrumental problems, local twelve-hour changes in the Channel 2 temperatures can result from gridding errors, movements of cloud systems, and the evolution or decay of cloud systems. The possibility of diurnal variations in cloudiness was examined by looking only for the repeated appearance, then disappearance, of temperature anomalies on both days. Figure 19 shows the

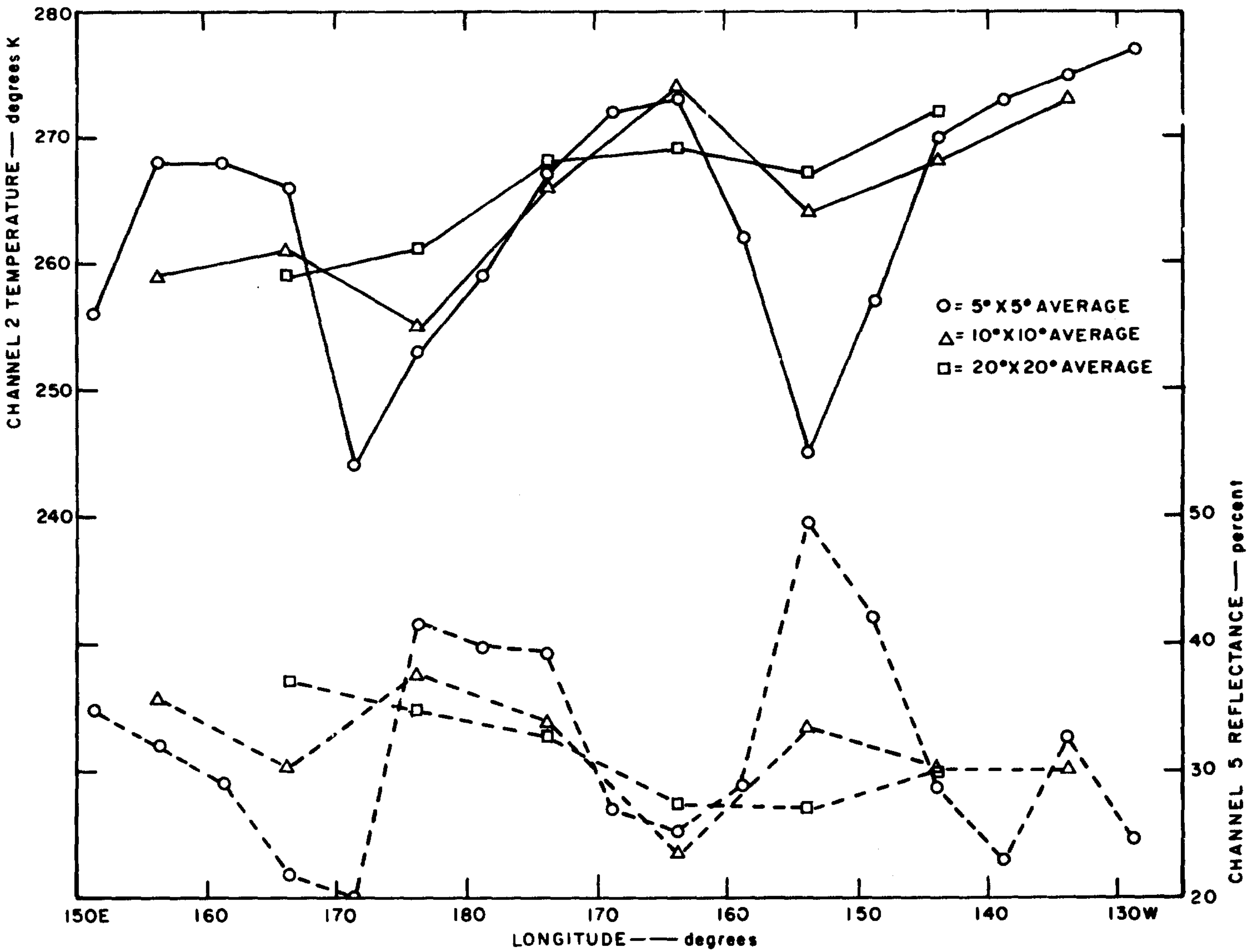

FIG. 18 INFLUENCE OF SCALE OF AVERAGING ON CHANNEL 2 (10-11 microns) EQUIVALENT TEMPERATURES AND CHANNEL 5 (0.2-4.0 microns) SOLAR REFLECTANCES ALONG 40°N LATITUDE OVER PACIFIC OCEAN. Data from 1:20 million multi-resolution Mercator mappings, Nimbus II, 16 June 1966, orbits 432 to 435.

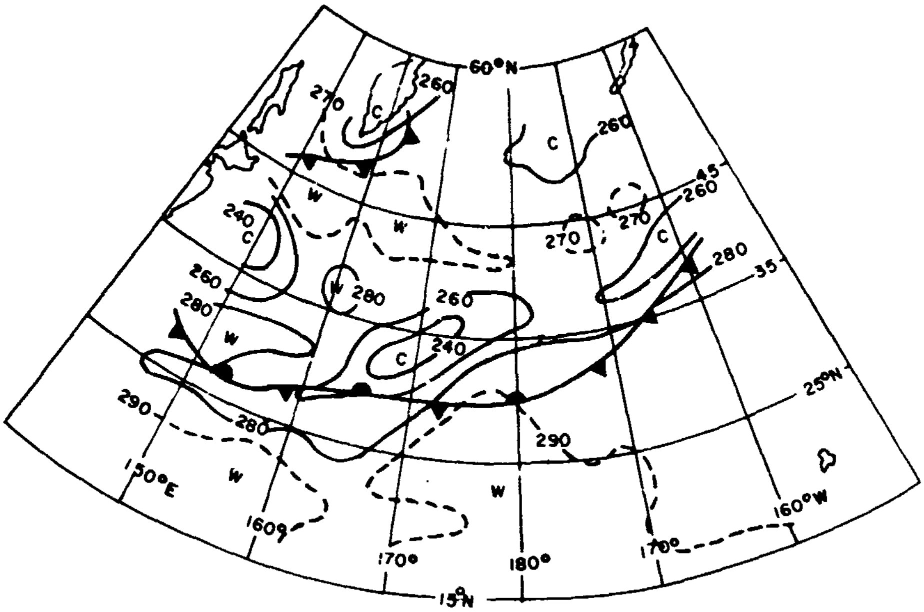

NIGHTTIME, 0940--1325 GMT

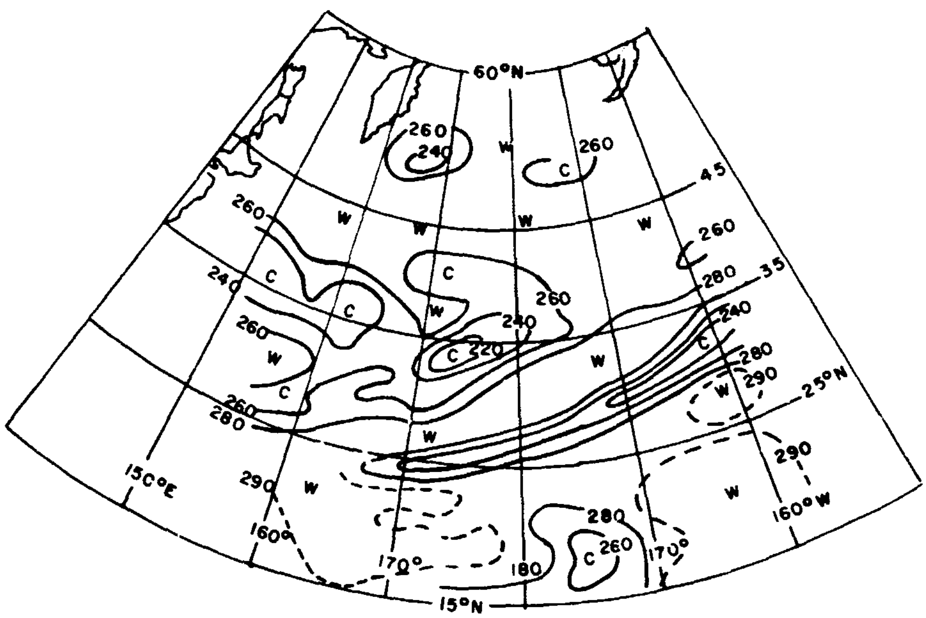

DAYTIME, 2140—2340GMT

FIG. 19 NIGHTTIME AND DAYTIME DISTRIBUTIONS OF CHANNEL 2 TEMPERATURES FROM NIMBUS II OVER THE PACIFIC OCEAN ON 16 JUNE 1966. Surface frontal positions from U.S. Weather Bureau analysis for 1200 GMT.

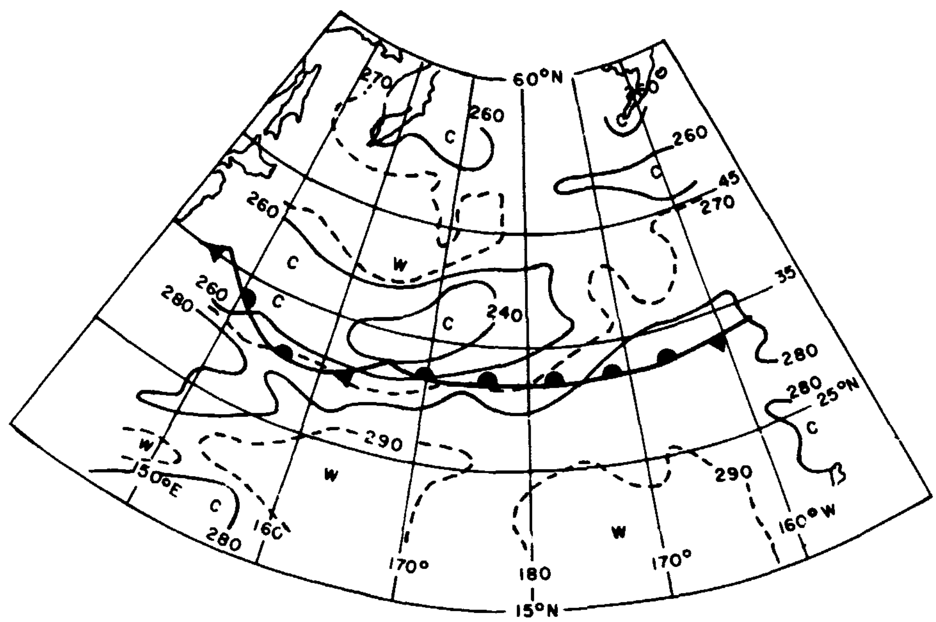

NIGHTTIME, 1050—1255GMT

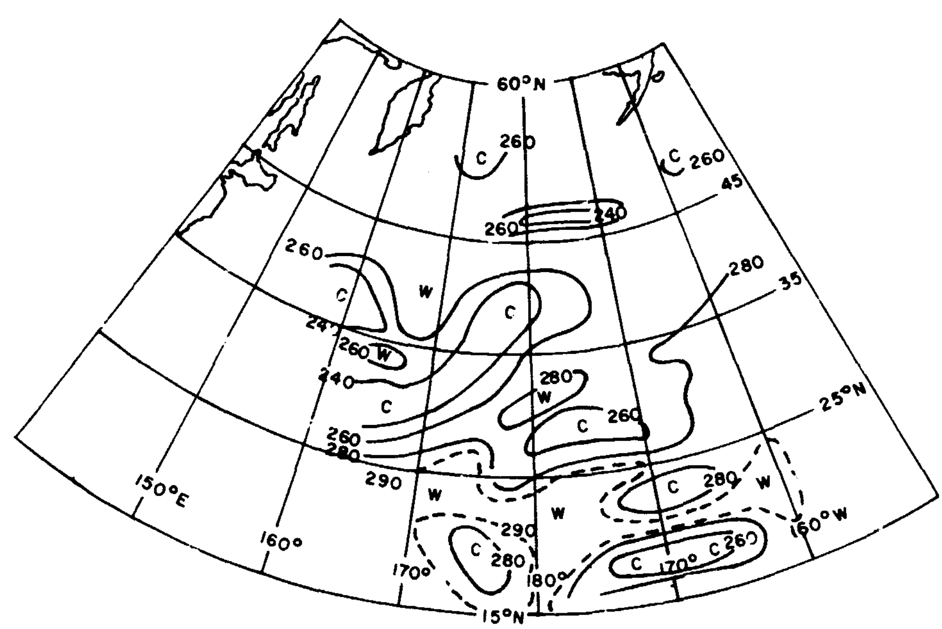

DAYTIME, 2107—2307 GMT

FIG. 20 NIGHTTIME AND DAYTIME DISTRIBUTIONS OF CHANNEL 2 TEMPERATURES FROM NIMBUS II OVER THE PACIFIC OCEAN ON 17 JUNE 1966. Surface frontal positions from U.S. Weather Bureau analysis for 1200 GMT.

daytime appearance of a band of low temperatures roughly parallel to the frontal position; on the previous and subsequent nighttime maps this anomaly is absent. On the second day a smaller area (unbanded) of lower temperatures again appears in the same region. Furthermore, several regions of slightly lower temperatures appear only in the daytime in the tropics on both days. Thus the colder regions in the daytime south of the frontal zone take on a diurnal character despite the fact that the Channel 5 reflectances are relatively low with a flat distribution.

The results suggest a daytime increase in thin or tenuous cirrus with low reflectance in the tropical air, presumably as remnants of early morning cumulonimbus buildups. Surface observations were too sparse to substantiate this. In an effort to seek substantiation some segments of Channel 1 and Channel 5 data from select swaths were assembled and are presented in Fig. 21. Although the spatial coverage was limited, the Channel 1 temperatures tend to indicate that some of the day-night changes were associated with daytime cirrus. With some exception near the cold band on 16 June, the Channel 5 reflectances were low throughout the tropics. A quick survey of the pictorial catalog of MRIR data suggests that occurrences of relatively low Channel 2 temperatures with relatively low Channel 5 radiances are rare. Furthermore, a review of hourly surface observations during June at Wake Island failed to support a predominance of daytime (near noon) cirrus occurrence. In fact, when taking obvious detection difficulties by surface observers into account, there seemed to be a slight preference for nocturnal cirrus. Therefore, it appears that the deduced diurnal variation of cirrus clouds (with daytime occurrence) was probably a coincidence descriptive only of a very-short-term sequence. Some contribution to the observed patterns could have resulted from scattered thick cumulus clouds with enhanced limb darkening for Channel 2, and perhaps some reduction of Channel 5 reflectance as a result of shadows (not likely).

In an earlier investigation,[7] spot comparisons of satellite data and ship reports suggested that simple summaries of Channel 2 and Channel 5 data for arbitrary cloud conditions showed relationships to the latent and sensible heat exchanges at the sea surface. In this study

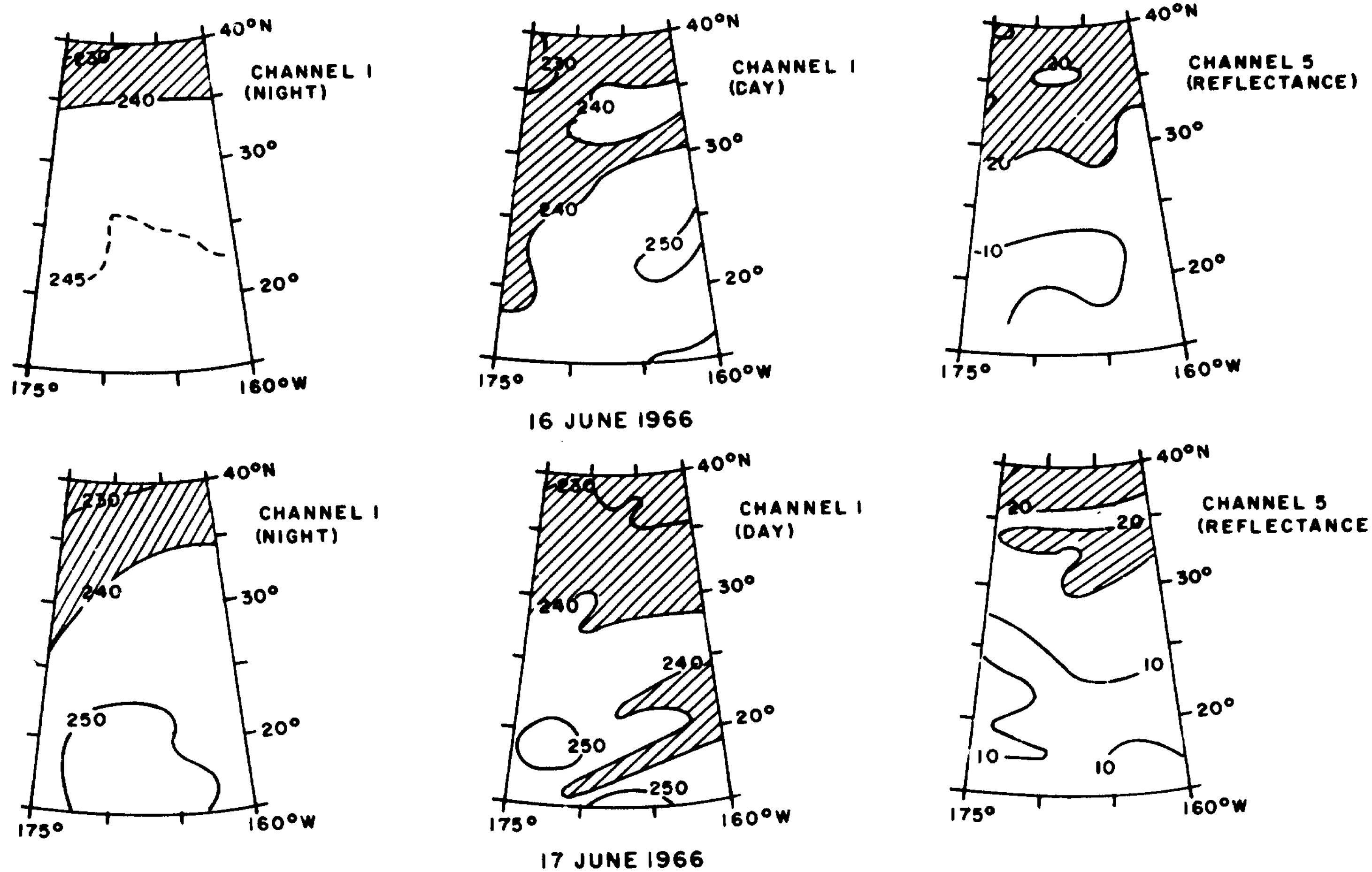

FIG. 21 NIGHTTIME AND DAYTIME CHANNEL 1 TEMPERATURES AND DAYTIME CHANNEL 5 REFLECTANCES (percent) OVER SELECT REGION OF PACIFIC OCEAN

the investigation was extended by comparing samples of Nimbus II radiometric data with independent analyses of the concurrent latent-plus-sensible-heat exchange at the sea surface. Thus a departure was made from isolated spot comparisons. Heat exchange analyses at the sea surface were extracted from maps prepared at the U.S. Fleet Numerical Weather Facility, Monterey, California. These synoptic-scale maps are based on numerical analyses of sea-surface temperature, winds, and the temperature and dew-point differences between ocean and air. Of course, there is more uncertainty in the spatial distribution of the analyzed heat exchange than in the radiometric data.

Figure 22 shows the distributions of Channel 2 temperature, Channel 5 reflectance, and the analyzed latent-plus-sensible-heat exchange along 40°N latitude on successive days (16 and 17 June 1966). All data have been normalized in order to present a more comprehensible comparison; radiometric data were extracted by 5-by-5-degree grid averages. Precipitation was not an important factor in this cross section.

It can be anticipated that attempts to establish a linear relationship between simple radiometric measurements and the surface heat exchange will encounter difficulties. With clear skies, the low Channel 5 reflectances and high Channel 2 temperatures will generally be associated with an enhanced latent-plus-sensible-heat exchange. On the other hand, with stratiform overcasts the high Channel 5 reflectances and low Channel 2 temperature will generally be associated with a reduced latent-plus-sensible-heat exchange and minimum values of the quantity "evaporation-minus-precipitation." Calm or weak winds and/or stable warm-air advection could alter the relationship for clear conditions, and strong winds or cold-air advection could alter the expected relationship for cloudy conditions. Furthermore, cellular cloud conditions, indicative of a strong exchange, may be associated with intermediate radiometric responses. Fog, and a low heat exchange, often occurs with a mixed radiometric response (substantial or moderate Channel 5 reflectance and high Channel 2 temperature) whereas cirrus clouds often occur with relatively low Channel 5 reflectance and low Channel 2 temperatures without an obvious association to the surface heat exchange. Therefore, in order to relate the surface

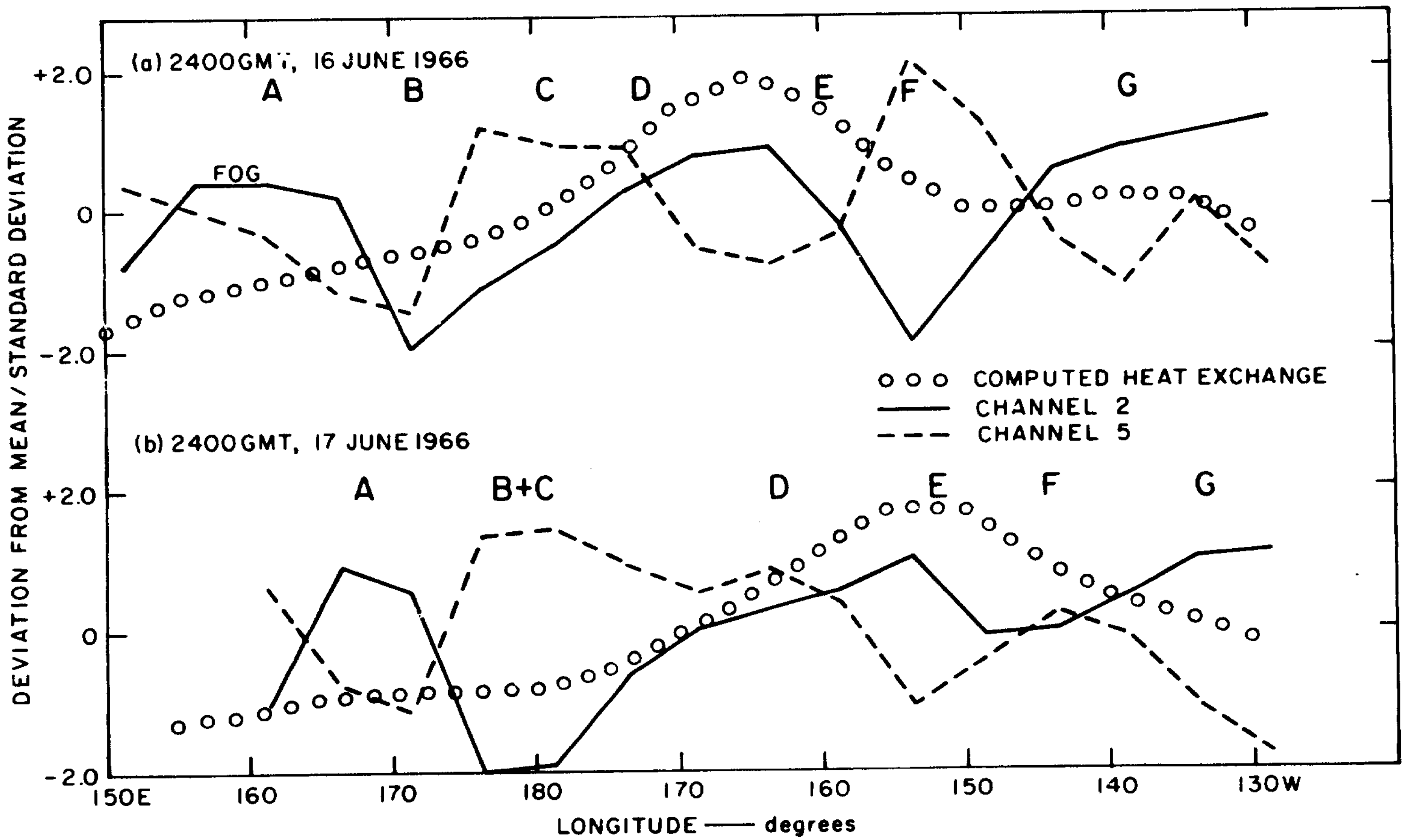

A: WEAK WINDS B: CIRRIFORM C: EXTENSIVE LOW CLOUDS D: HIGH-PRESSURE CENTER
E: POST-FRONTAL CLEARING F: FRONTAL G: MOSTLY CLEAR, WARM ADVECTION

FIG. 22 NORMALIZED DISTRIBUTIONS OF NIMBUS II RADIOMETRIC DATA AND COMPUTED SURFACE HEAT EXCHANGE ALONG 40°N LATITUDE ON SUCCESSIVE DAYS (5° x 5° resolution) heat exchange to radiometric data on a local scale, it probably is necessary to identify the gross cloud type, the average wind speed, and the synoptic-scale advection.

The normalized distribution of the heat exchange along the zonal strip in Fig. 22 shows that the maximum occurs in the generally clear, "forward" portion of an anticyclone; more specifically the maximum lies between the frontal zone and the following high-pressure center. The minimum exchange occurred in a col-like zone (near Point A) with very weak winds (generally from the south) and patches of fog or low clouds. On the eastern end of the cross section the heat exchange was intermediate in spite of clear skies because of some warm-air advection ahead of the frontal zone. On 16 June there was an occurrence of cumuliform cloudiness (Point B) without lower clouds; on 17 June the cirriform cloudiness was mixed with lower stratiform cloudiness in advance of a developing disturbance. In conjunction with synoptic intelligence it appears possible to explain the distribution of heat exchange. Perhaps the most direct local application of the radiometric data is as an aid to the identification of pertinent synoptic conditions. The plots in Fig. 22 demonstrate how well the movement of the synoptic features (or their intersections at latitude 40°N) over 24 hours can be documented. The frontal region, in addition to its eastward movement, shows a definite weakening. The region of maximum heat exchange moves at the same rate as the radiometric representation of the synoptic features.

Figure 23 shows the north-south distribution of normalized data along the 161°W meridian on 16 June 1966 and a portion of a nearly concurrent ESSA 1 nephanalysis. A pronounced meridional variation, which actually exceeds the zonal variation mentioned above, is apparent. The strong heat exchange in the generally clear tropics (presumably in the trade-wind region) drops rather sharply on the poleward side of a narrow cloud band seen on the ESSA 1 nephanalysis. The radiometric data indicate some cirriform cloudiness (not identified on the nephanalysis) near 30°N. A secondary maximum in the heat exchange extends from the frontal zone poleward to another region of overcast.

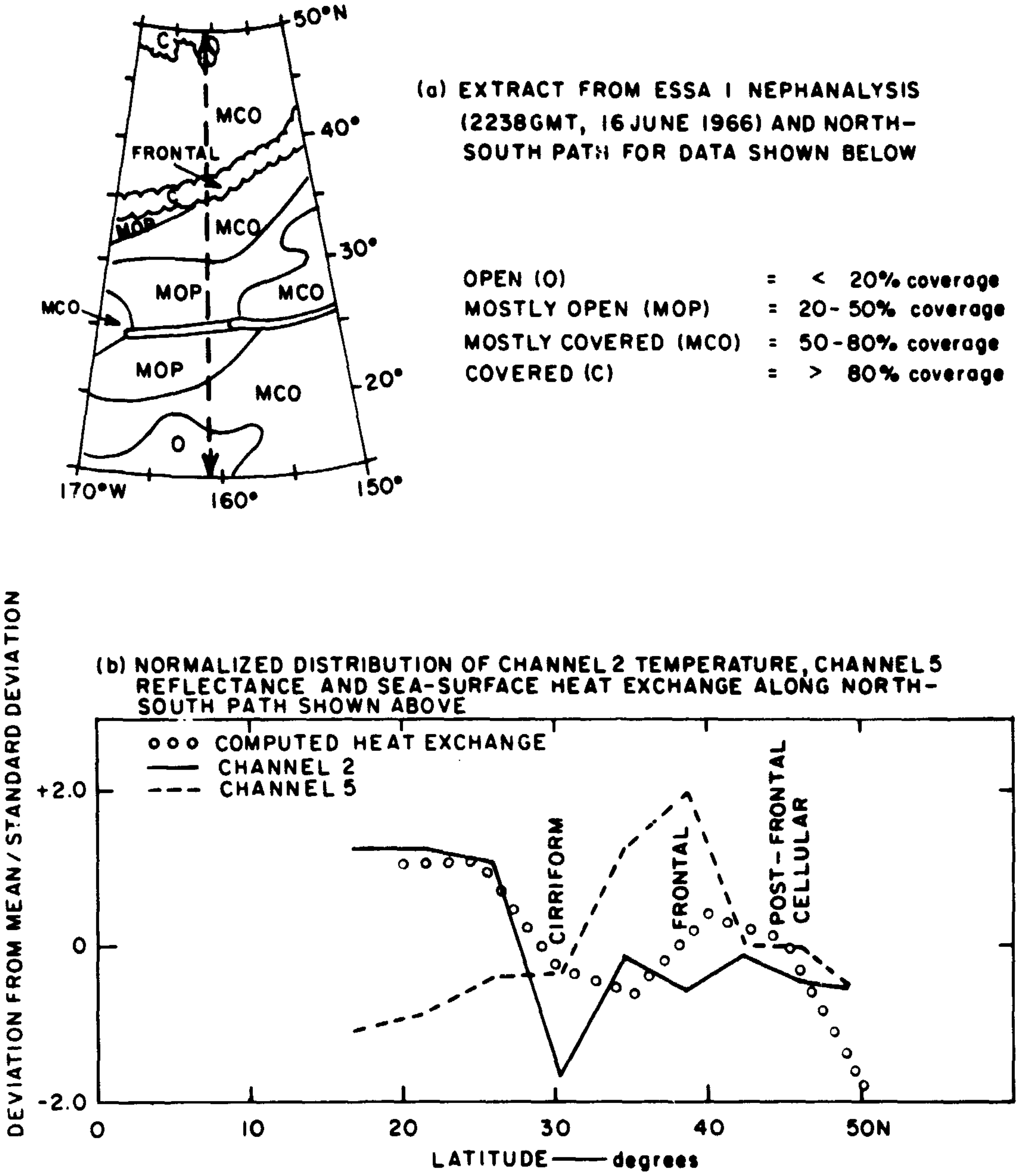

FIG. 23 ESSA 1 NEPHANALYSIS AND NORMALIZED DISTRIBUTIONS OF COMPUTED SURFACE HEAT EXCHANGE AND NIMBUS II RADIOMETRIC DATA ALONG 161°W LONGITUDE

B. 15-Day Averages

Over longer periods of time, which are important to the general circulation, it is possible to obtain relationships between averaged radiometric and heat-exchange data that are more direct than the relationships on a local scale. Averages for two weeks or longer will show smoother variations, and some of the random errors of analysis will be reduced. Over the North Pacific a comparison was made between spatial distributions of 15-day averages of radiation data and heat-exchange data. Results are illustrated in Fig. 24.

The analyzed 15-day heat-exchange chart did not have the benefit of the extensive spatial coverage of the satellite, but represents the best available estimates on a somewhat larger spatial resolution. Although some gross similarities exist between the radiation budget components and the heat exchange, no truly remarkable relationship can be claimed. Perhaps the outgoing long-wave flux (highly correlated with Channel 2) shows patterns most similar to the heat exchange.

If some degree of spatial averaging, especially zonal averaging, is combined with the time averaging, better correspondence between radiometric and heat-exchange data is achieved. Thus, in spite of local uncertainties, radiometric data summaries may be directly useful to global or climatological studies. For the 15-day period from 16-30 June 1966, radiation data, originally from 5-degree grid blocks, were obtained as averages along particular zonal segments in both the Pacific and Atlantic Oceans. The 15-day heat-exchange data were averaged along the same segments for comparison. Emphasis on data presentation was restricted to the daytime data because readouts of satellite data were complete only for the daytime over the Atlantic Ocean. However, it was noted that over both oceans the analyzed daytime heat exchange was slightly <u>smaller</u> than the day-plus-night exchange, probably because of diurnal variations in wind speed and stability over the sea surface.[23] The nocturnal wind-speed maximum is most pronounced outside the tropics, but the double diurnal oscillation in the trade-wind zone would still show a larger midnight wind speed than at noon. Presumably, a slight nocturnal decrease in

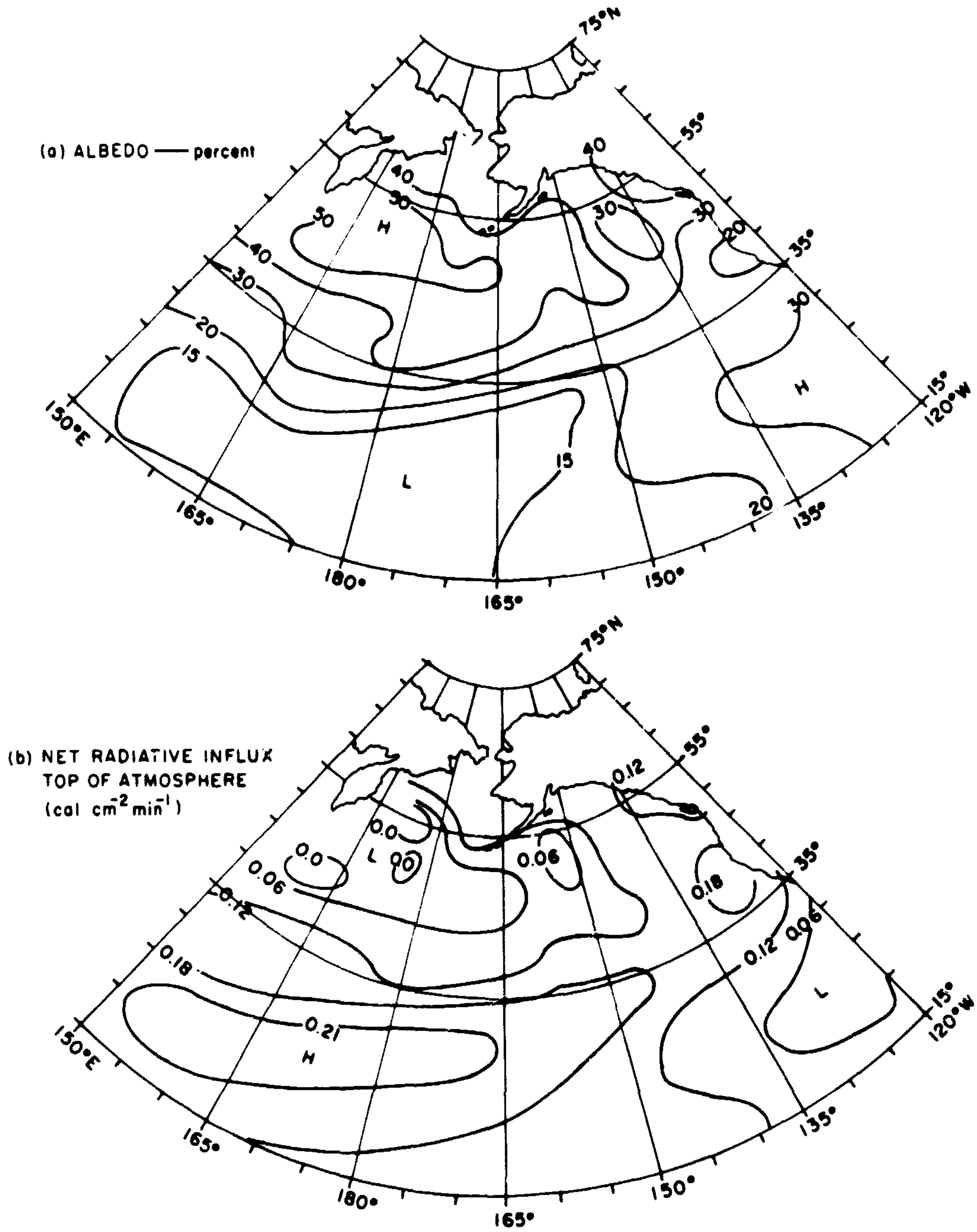

FIG. 24 15-DAY AVERAGE DISTRIBUTION OF RADIATIVE QUANTITIES INFERRED FROM NIMBUS II AND COMPUTED SURFACE HEAT EXCHANGE OVER THE NORTH PACIFIC OCEAN, 16-30 JUNE 1966

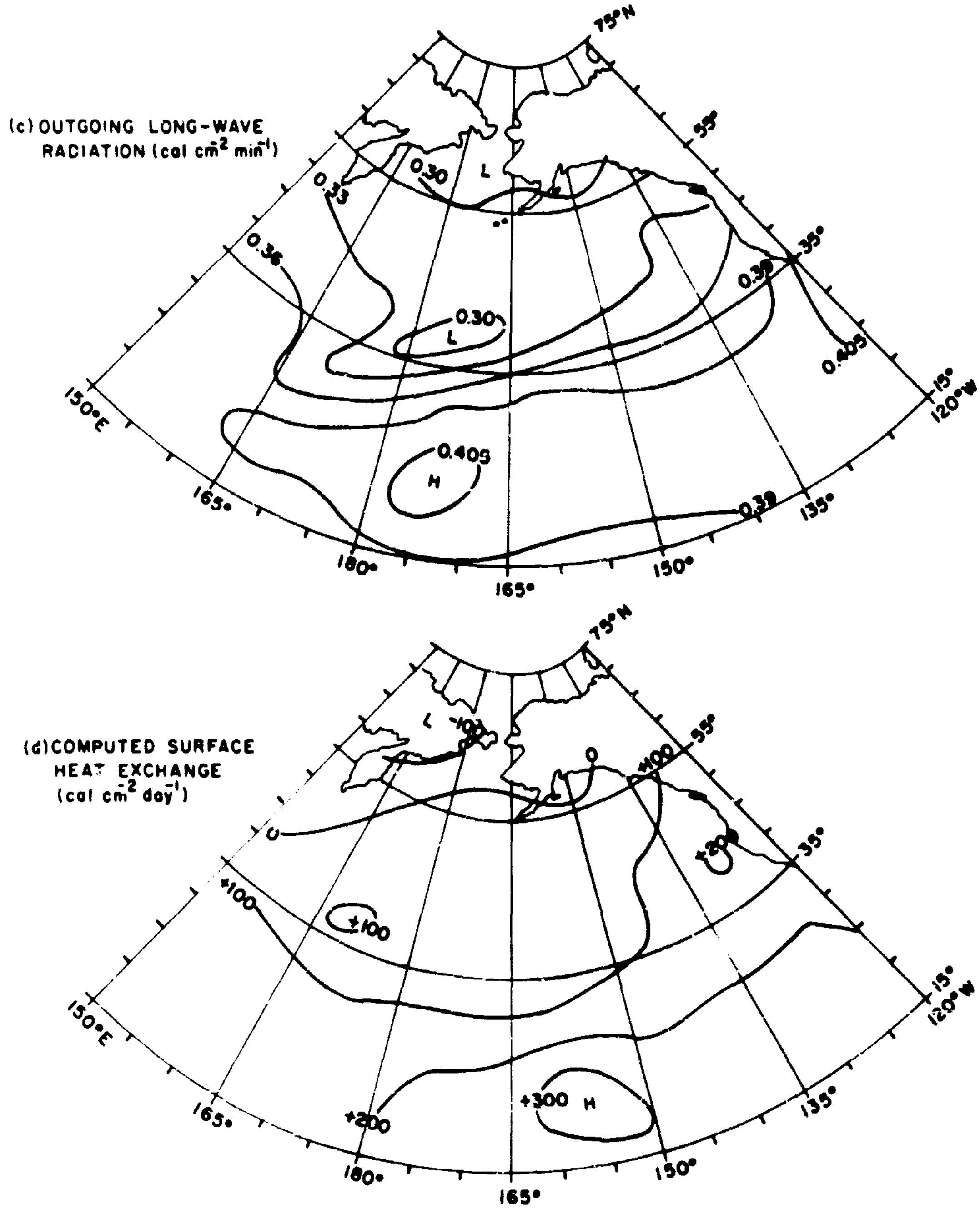

FIG. 24 Concluded

stability associated with a larger diurnal temperature range in the air than at the sea surface may be related to the low-level diurnal wind variation.

For the Pacific Ocean, data were averaged along the latitudes 20.7°N, 34.0°N, and 48.9°N between the meridians 150°E and 120°W. Table XI summarizes the results; a simple direct relationship to the outgoing longwave flux and an inverse relationship to the albedo is apparent.

Table XI

SUMMARIES OF AVERAGED NIMBUS II DATA AND AIR-SEA HEAT EXCHANGE OVER NORTH PACIFIC OCEAN, 16-30 JUNE 1966

Latitude (°N)	Latent & Sensible Heat Exchange (cal cm^{-2} day^{-1})	Albedo (percent)	Outgoing IR Flux (cal $cm^{-2}min^{-1}$)	Channel 2 Temperature (°K)
48.9	17	45.1	.322	265.6
34.0	85	24.7	.361	278.3
20.7	225	19.3	.401	287.0

For the Atlantic Ocean, data at each latitude were available in two longitudinal segments (15-45 and 45-70°W). Consequently, it was possible to summarize the results for each segment and to note differences with the average for both segments. A total of four latitudes (instead of three as over the pacific) were included in the summary; closer spacing of the latitudes served to illustrate how the simple relationships tend to weaken on the smaller scale, especially in the tropics. Table XII presents the results, and Fig. 25 shows the average sea-level pressure distributions over both oceans.

The averages for both zonal segments in Table XII show the same trends as those for the Pacific, but, partly as a result of closer spacing, the overall correspondence is somewhat less pronounced. Although the heat exchange is larger over the Atlantic, meridional gradients are slightly smaller. At 34°N the Pacific Ocean had more cloudiness than the Atlantic; the Pacific high-pressure center was displaced slightly southward.

When data from each segment are examined separately, the relationships tend to break down southward of the high-pressure center. To some extent the cloud variations (which are not independent of the exchange) are responsible. At latitude 16°N between 45 and 70°W longitude a maximum heat exchange is noted; the relatively clear skies, warm water, and a substantial trade-wind flow probably account for the maximum. In the same meridional range, the lowest heat exchange is found along 41.9°W, possibly as a result of advection of relatively warm air in addition to significant cloudiness. In the eastern Atlantic the maximum latent-plus-sensible heat exchange also occurs with the minimum albedo and the minimum exchange with the maximum albedo, superposed on a meridional gradient which shows an equatorward increase. Judging from the Channel 2 temperatures the cloud tops are lower over the eastern Atlantic (east of the high-pressure center) than over the western Atlantic. For the Atlantic as a whole, the spatial distribution of the heat exchange and radiometric data depends on the existing average circulation pattern, and implicitly on the wind speed, advection, vertical motion, and stability. However, the average for both segments show an equatorward increase in heat exchange, outgoing IR flux, and Channel 2 temperature, and a poleward increase in the albedo, just as over the Pacific.

Table XII

SUMMARIES OF AVERAGED NIMBUS II DATA AND AIR-SEA HEAT EXCHANGE OVER NORTH ATLANTIC OCEAN, 16-30 JUNE 1966

Range of Longitude	Latitude (°N)	Latent & Sensible Heat Exchange (cal $cm^{-2}day^{-1}$)	Albedo (percent)	Outgoing IR Flux (cal $cm^{-2}min^{-1}$)	Channel 2 Temperature (°K)
15-45° W	41.9	101	29.2	.364	278.8
	34.0	172	21.0	.385	283.6
	25.3	269	17.0	.399	286.7
	16.0	253	20.8	.396	286.6
45-70° W	41.9	4	33.1	.333	271.2
	34.0	168	18.3	.364	280.8
	25.3	218	21.2	.359	278.3
	16.0	347	15.7	.368	283.3
15-70° W	41.9	57(64)*	31.0	.350	275.3
	34.0	170(180)	19.8	.375	282.4
	25.3	246(248)	18.9	.380	282.9
	16.0	296(316)	18.5	.383	285.1

*( ) = Heat exchange for day and night combined

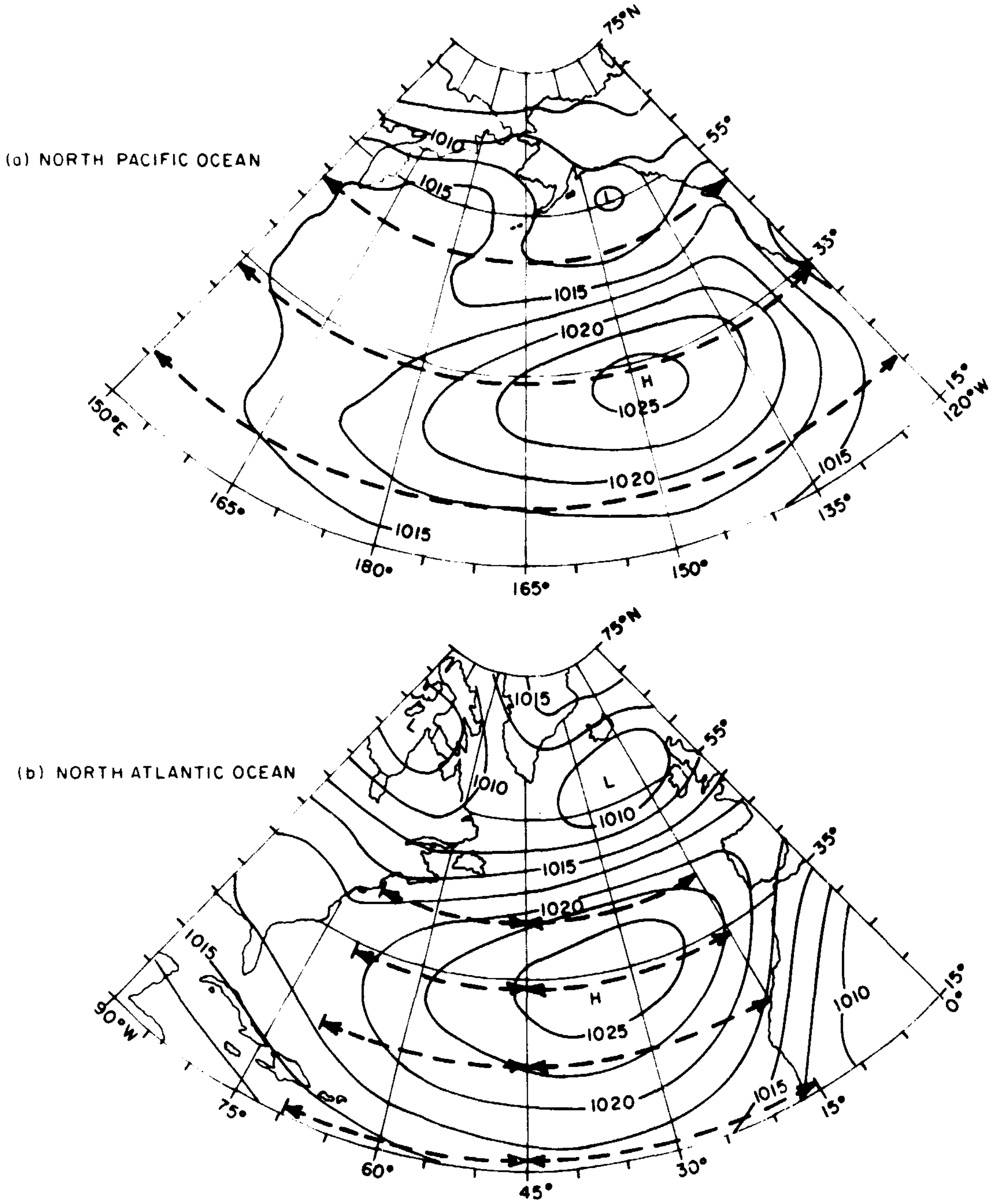

FIG. 25 15-DAY MEAN SEA-LEVEL PRESSURE DISTRIBUTIONS, 15-29 JUNE 1966, AND PARALLEL SECTIONS (dashed) ASSOCIATED WITH NIMBUS II DATA SUMMARIES

PRECEDING PAGE BLANK NOT FILMED.

VII IMPLICATIONS FOR ADDITIONAL RESEARCH

It is apparent that the IR computational model should be more fully exploited in conjunction with extended samples of multichannel radiometric data from satellites and surface data in order to devise useful methods for obtaining objective descriptions of clouds and general features of the tropospheric structure (such as tropopause-base distribution)--largely as an aid to programs for the remote inference of temperature and water-vapor profiles. Comparative studies of the infrared fluxes and cooling, both in time at fixed points and in space at fixed solar time, should be extended in conjunction with an assessment of the energetics in about three layers over a large region, perhaps in the tropics. Computations of transports of heat, water vapor, and kinetic energy should be included. When the capability to obtain objective cloud descriptions is achieved, then, with the aid of cloud photographs, water-budget studies can begin. Still to be determined is the minimum accuracy with which clouds, temperature structure, and water-vapor structure must be specified in order to describe distributions of infrared cooling or solar heating without conventional upper-air data. In connection with the solar heating, an analysis of concurrent satellite and surface measurements of solar radiation and clouds could be conducted immediately for the purpose of devising an adequate empirical model relating solar absorption in the atmosphere to clouds, haze, and total precipitable water.

With the aid of the IR model, the effects of various atmospheric and boundary conditions on the response of satellite radiometers can be examined, for both existing and future radiometric channels. However, computed radiances throughout the window region should be checked in detail against observed radiances for known background conditions. Analyses of MRIR data can profitably be pursued to deduce cloud transmittances, reflectances, and heights or amounts (one assumed known), especially for cirrus. Methods should be studied for taking advantage of limb variations in different spectral regions as a function of clouds and moisture. A satellite-borne radiometer that scans in the orbital plane would generate a wealth of data for that purpose by viewing each subsatellite spot from a variety of angles. Finally, the relationship between distributions of MRIR data and distributions of the sea-surface heat exchange, in contrast to the relationship between quasi-global zonal-time averages, should be further clarified as a function of pertinent synoptic factors from the viewpoint of obtaining the additional factors by other remote means (e.g., changes and motions deduced from ATS satellite data).

APPENDICES

PRECEDING PAGE BLANK NOT FILMED.

Appendix A

TEMPERATURE-DEPENDENT WEIGHTING FACTORS FOR TRANSMISSION COMPUTATIONS

The weighting factors, u and v, defined by Eqs. (5) and (6) and utilized in Eqs. (7) and (8) of Sec. III, are illustrated as Parts (a) and (b), respectively, of Figs. A-1, A-2, and A-3. All of the curves have been represented by second-degree polynomials of the form

$$u = 1 + a_1 (T-T_o) + a_2 (T-T_o)^2$$

$$v = 1 + b_1 (T-T_o) + b_2 (T-T_o)^2 \quad .$$

Coefficients for the polynomials are tabulated below for pertinent intervals in wave number (cm^{-1}).

Rotational Band, Water Vapor				
Interval	$10^2 a_1$	$10^5 a_2$	$10^2 b_1$	$10^5 b_2$
20-80	-0.435	2.481	-0.500	3.361
80-160	-0.249	0.441	-0.181	0.024
160-260	0.017	-1.058	0.096	-0.708
260-360	0.574	-0.509	0.564	-0.300
360-460	1.230	4.409	1.105	2.879
460-545	1.292	5.466	1.383	5.741
545-617	1.103	3.108	1.157	3.650
617-667	1.563	7.133	1.401	5.399
667-720	1.54	6.85	1.53	6.56
720-750	1.64	7.90	1.70	8.20
750-800	1.71	8.42	1.71	8.25

15-Micron Band, Carbon Dioxide				
Interval	$10^2 a_1$	$10^5 a_2$	$10^2 b_1$	$10^5 b_2$
545-617	1.169	3.527	1.563	6.648
617-667	0.093	0.126	0.580	0.743
667-720	0.030	0.055	0.418	0.268
720-750	0.921	1.587	1.158	3.470
750-800	1.841	8.965	1.996	10.410

6.3-Micron Band, Water Vapor				
Interval	$10^2 a_1$	$10^5 a_2$	$10^2 b_1$	$10^5 b_2$
1250-1350	1.09	3.35	1.03	3.03
1350-1450	0.381	-0.768	0.381	-0.534
1450-1600	-0.206	0.399	-0.127	-0.001
1600-1750	-0.282	1.590	-0.235	2.030
1750-1900	-0.002	-0.200	0.256	-0.081
1900-2050	0.406	-0.896	0.548	0.052
2050-2200	1.27	4.35	1.42	5.56

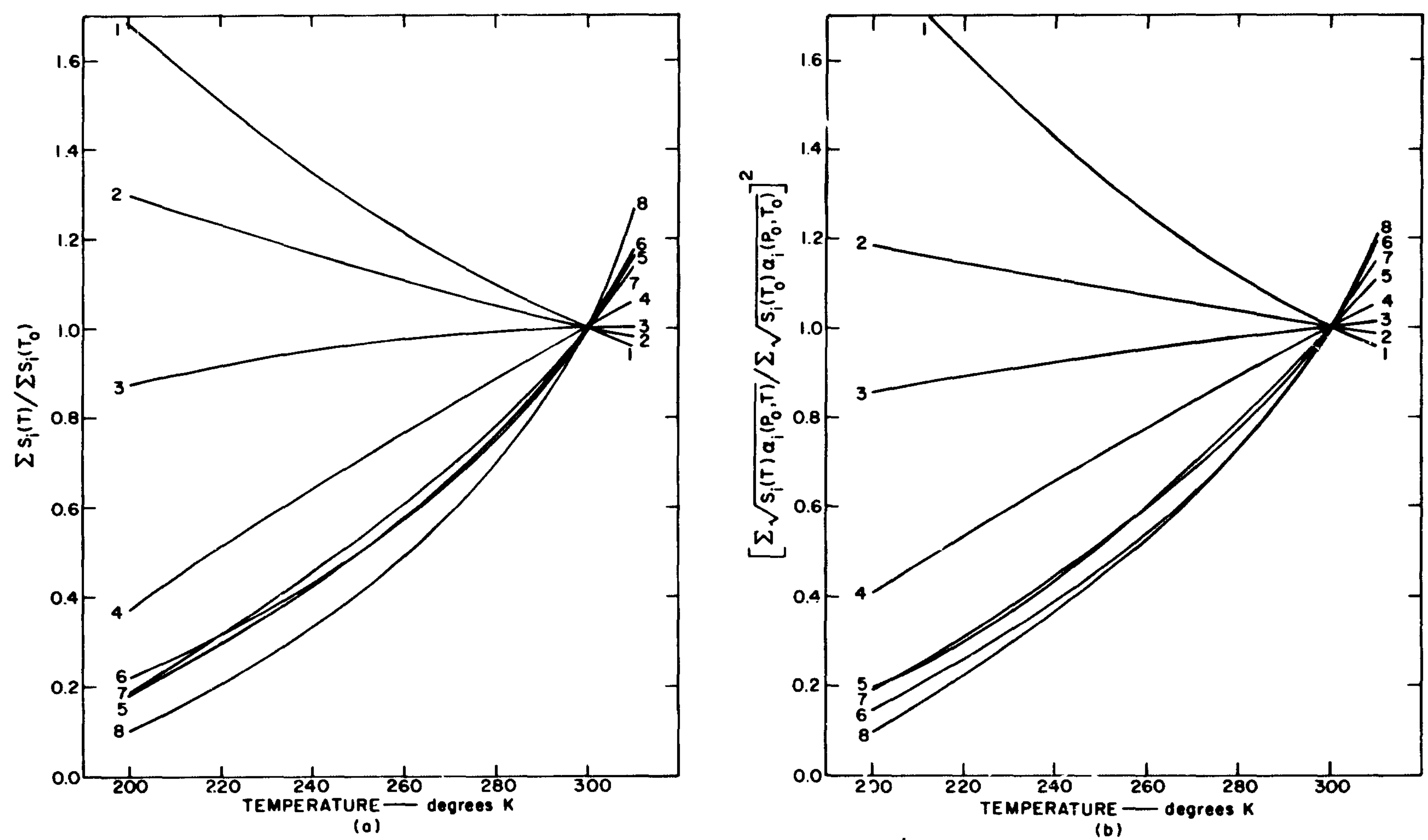

Spectral intervals in wave number (cm^{-1}) defined by

(1) 20–80 (3) 160–260 (5) 360–460 (7) 545–617

(2) 80–160 (4) 260–360 (6) 460–545 (8) 617–667

FIG. A-1 VARIATION WITH TEMPERATURE OF WEIGHTING FACTORS FOR ROTATIONAL BAND OF WATER VAPOR FOR DEFINING (a) Effective absorbing mass and (b) Effective pressure.

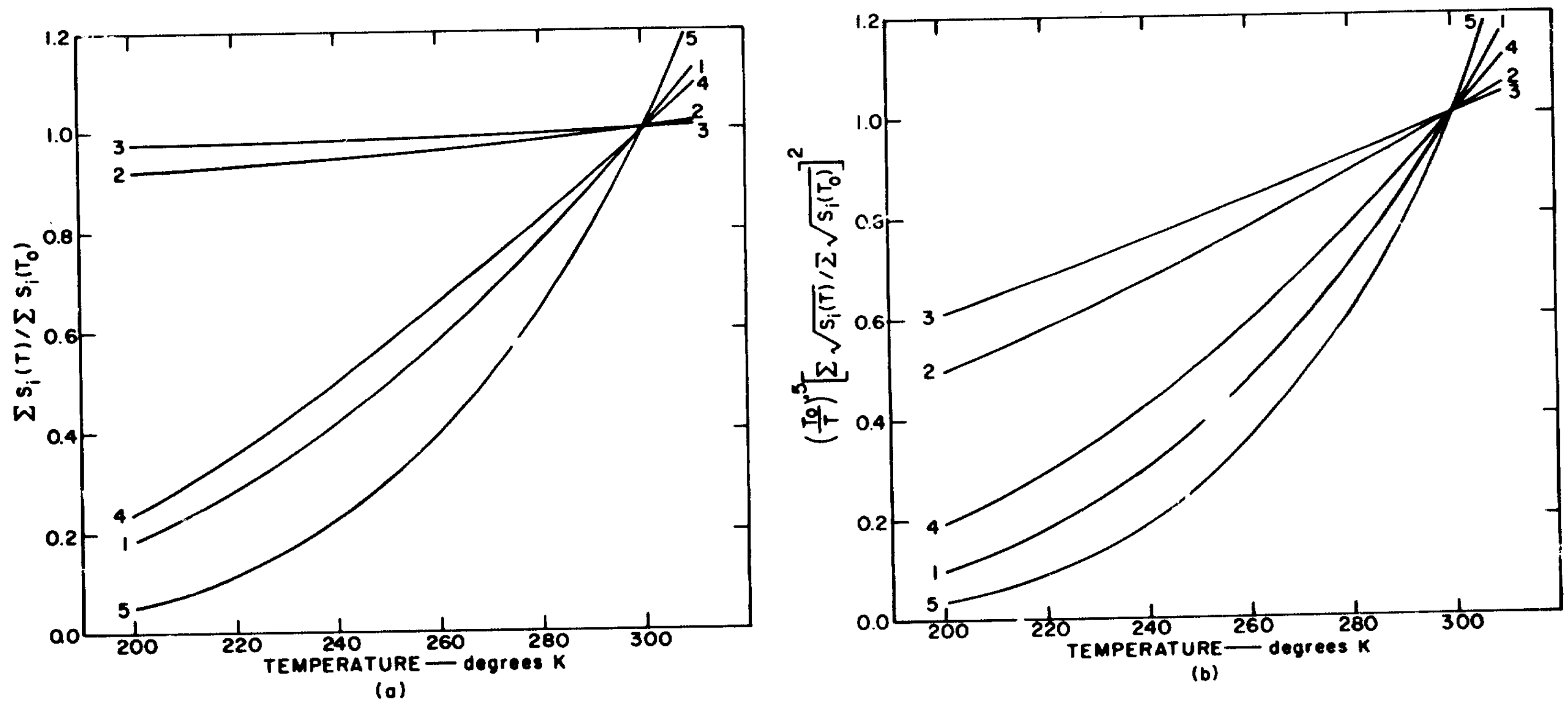

Spectral intervals in wave number (cm^{-1}) defined by

(1) 545-617 (4) 720-750
(2) 617-667 (5) 750-800
(3) 667-720

FIG. A-2 VARIATION WITH TEMPERATURE OF WEIGHTING FACTORS FOR 15-MICRON BAND OF CARBON DIOXIDE FOR DEFINING (a) Effective absorbing mass and (b) Effective Pressure.

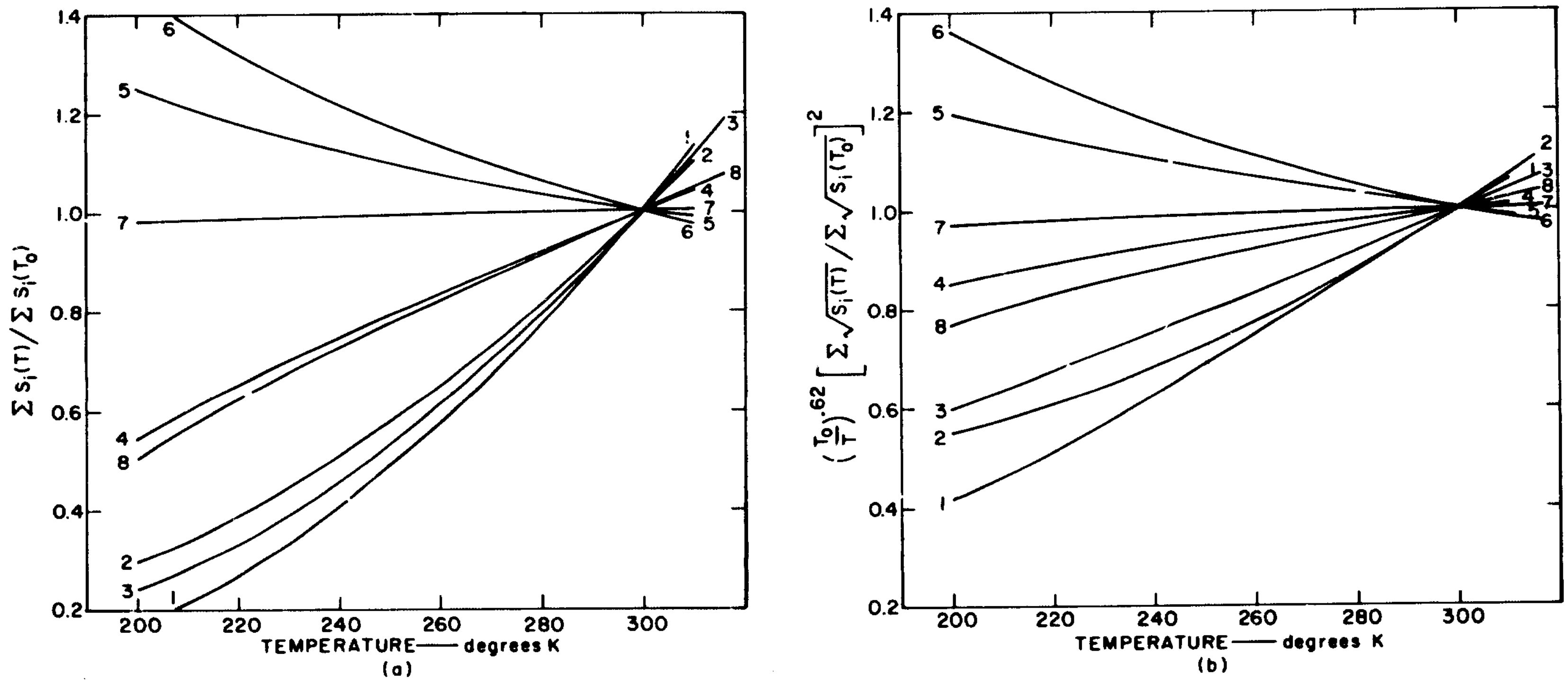

Spectral intervals in wave number (cm^{-1}) defined by

(1) 1120–1190	(4) 1350–1450	(7) 1750–1900
(2) 1190–1250	(5) 1450–1600	(8) 1900–2050
(3) 1250–1350	(6) 1600–1750	

FIG. A-3 VARIATION WITH TEMPERATURE OF WEIGHTING FACTORS FOR 6.3-MICRON BAND OF WATER VAPOR FOR DEFINING (a) Effective absorbing mass and (b) Effective pressure.

PRECEDING PAGE BLANK NOT FILMED.

Appendix B

PARAMETERS FOR TRANSMISSION REPRESENTATIONS

For each spectral interval (see Table II) the representation of the transmission requires the specification of three parameters [see Eq. (10)]: A, C, and D. These parameters are tabulated below with two omissions. In the water-vapor absorption bands D equals -0.5 throughout; in the window region [see Eqs. (14) and (15)] only the parameters A and D are used.

Water Vapor (Rotational)						Carbon Dioxide (15-μ Band)			
Interval No.	A	C	Interval No.	A	C	Interval No.	A	C	D
1	23.0	0.00025	7	1.2	0.09	7	0.076	10.0	-0.40
2	37.0	0.00008	8	0.78	0.2	8	1.02	0.8	-0.46
3	27.0	0.0002	9	0.57	0.3	9	1.05	1.0	-0.50
4	14.0	0.001	10	0.46	0.5	10	0.19	9.0	-0.47
5	5.0	0.005	11	0.40	0.9	11	0.011	27.0	-0.36
6	2.2	0.035							

Window Region			Water Vapor (6.3-μ Band)		
Interval No.	A	D	Interval No.	A	C
12	0.15	0.80	19	1.3	0.05
13	0.11	0.87	20	5.4	0.006
14	0.095	0.88	21	13.8	0.0007
15	0.091	0.885	22	13.0	0.0007
16	0.091	0.885	23	5.0	0.009
17	0.12	0.80	24	1.2	0.09
18	0.16	0.72	25	0.4	0.5

PRECEDING PAGE BLANK NOT FILMED.

Appendix C

METHOD FOR CONVERSION TO FLUX TRANSMITTANCE

The technique adopted for converting the representation of a beam transmittance to a flux transmittance is to replace terms involving the angle θ with appropriate expressions that will yield the desired final transmittance. The replacement is most conveniently described by introducing the ratio R defined by

$$R = \tilde{W}^2/\widetilde{WP} \ .$$

For the rotational and vibrational-rotational bands of water vapor an initial step in the transmission computation is to determine

$$\ell n(-\ell n \tau) = 0.5 \left\{\ell n[A^2 \ \widetilde{WP}] + \ell n[R/\cos\theta \ (R + C \cos\theta)]\right\} . \qquad \text{(C-1)}$$

If the flux transmittance is desired, the term involving $\cos\theta$ is replaced with a linear function of the first term on the right side of Eq. (C-1):

$$\ell n[R/\cos\theta \ (R + C\cos\theta)] = m_1 \ \ell n \ [A^2 \ \widetilde{WP}] + m_2$$

where the pair of parameters (m_1, m_2) were empirically determined as (0.382, 0.77011), (0.0, 0.4688), and (-0.047, 0.43178) for magnitudes of $\ell n[A^2 \ \widetilde{WP}]$ less than, equal to, or greater than -0.7886, respectively.

For the window region,

$$\ell n(-\ell n \tau) = D \left\{\ell n[AWP] + \ell n[\sec\theta]\right\} . \qquad \text{(C-2)}$$

The flux transmittance is obtained by replacing $\ell n[\sec\theta]$ by 0.66 when $\ell n[AWP]$ is equal or less than -4.0; otherwise

$$\ell n[\sec\theta] = -0.0525 \ \ell n \ [AWP] + 0.45 \ .$$

For the interval 1190-1250 cm^{-1},

$$\ell n(-\ell n\tau) = D\left\{\ell n[AW/P] + \ell n[\sec\theta]\right\} \quad . \tag{C-3}$$

Here the flux transmittance is obtained by setting $\ell n[\sec\theta]$ to 0.63 for $\ell n[AW/P]$ equal or less than -4.0; otherwise,

$$\ell n[\sec\theta] = -0.0425\ \ell n[AW/P] + 0.46$$

Through the 15-micron band of carbon dioxide the joint transmission of water vapor and carbon dioxide must be considered--that is,

$$-\ell n\tau = -\ell n\tau_w - \ell n\tau_c \tag{C-4}$$

where the subscripts w and c refer to water vapor and carbon dioxide, respectively. The $-\ell n\tau_c$ for carbon dioxide is extracted from a table that is entered with the computed $\ell n\psi$. In other words,

$$-\ell n\tau_c = \text{TABLE}\left\{\ell n\psi\right\} = \text{TABLE}\left\{\ell n[\tilde{AW}/\cos\theta] + D\ \ell n[R_c/\cos\theta) + C]\right\} \tag{C-5}$$

whereas

$$-\ell n\tau_w = (\tilde{AW}/\cos\theta)\ [(R_w/\cos\theta) + C]^{-0.5} \quad . \tag{C-6}$$

When the flux transmittance is desired, the $\cos\theta$ in Eqs. (C-5) and (C-6) is replaced by

$$\cos\theta = m_1\ \ell n[R_w R_c] + m_2 \tag{C-7}$$

prior to combination in Eq. (C-4). Values of m_1 and m_2 in Eq. (C-7) are given below for each spectral interval:

Interval	m_1	m_2
545-617	0.012	0.580
617-667	0.010	0.640
667-720	0.008	0.645
720-750	0.008	0.600
750-800	0.005	0.550

REFERENCES

1. Nimbus II Users' Guide, National Space Science Data Center, Goddard Space Flight Center, NASA, Greenbelt, Md., 229 pp (July 1966).

2. E. Raschke, "The Radiation Blanace of the Earth-Atmosphere System from Radiation Measurements of the Nimbus II Meteorological Satellite," Technical Note TN D-4589, NASA Washington, D.C., 81 pp. (July 1968).

3. United States Weather Bureau, Climatological Data, National Summaries, U.S. Department of Commerce, Government Printing Office, Washington, D.C. (1966).

4. T. Sasamori, "The Radiative Cooling Calculation for Application to General Circulation Experiments," J. Appl. Meteor., 7, pp. 721-729 (1968).

5. H. M. Stone and S. Manabe, "Comparison Among Various Numerical Models Designed for Computing Infrared Cooling," Mon. Wea. Rev., 96, pp. 735-741 (1968).

6. P. A. Davis, "The Application of Infrared Flux Models to Atmospheric Data," J. Appl. Meteorol., 4, pp. 263-271 (1965).

7. P. A. Davis, "TIROS Radiation Measurements and Variations in Atmospheric Heating," Contractor Report NASA CR-581, NASA Washington, D.C., 46 pp. (October 1966).

8. B. H. Armstrong, "Analysis of the Curtis-Godson Approximation and Radiation Transmission Through Inhomogeneous Atmospheres," J. Atmos. Sci., 25, pp. 312-322 (1968).

9. C. Young, "A Study of the Influence of Carbon Dioxide on Infrared Radiative Transfer in the Stratosphere and Mesosphere, "Technical Report 04682-1-T, University of Michigan, Ann Arbor, Michigan (March 1964), modifications (1965).

10. P. J. Wyatt, V. R. Stull, and G. N. Plass, "Infrared Transmission Studies--The Infrared Absorption of Water Vapor," Final Report, SSD-TDR-62-127-Vol. II, Aeronutronic Division, Ford Motor Company, Newport Beach, California (September 1962).

11. R. M. Goody, Atmospheric Radiation, I: Theoretical Basis (Oxford University Press, London, 1964, 436 pp.).

12. W. L. Godson, "Infrared Transmission by Water Vapor, "Archiv. Met. Geoph. Biokl., B, Bd. 12, H.2, pp. 196-223 (1963).

13. R. M. Goody, "A Statistical Model for Water-Vapor Absorption," Quart. J. Roy. Meteorol. Soc., Vol. 78, pp. 165-169 (1952).

14. W. M. Elsasser, Heat Transfer by Infrared Radiation in the Atmosphere Harvard Meteorol. Studies No. 6, Harvard University Press, Cambridge, Mass., (1942).

15. C. D. Walshaw, "Integrated Absorption by the 9.6 Micron Band of Ozone," Quart. J. Roy. Meteor. Soc., Vol. 83, pp. 315-321 (1957).

16. D. E. Burch, D. Gryvnak, E. B. Singleton, W. L. France, and D. Williams, "Infrared Absorption by Carbon Dioxide, Water Vapor, and Minor Atmospheric Constituents," Research Report AFCRL-62-698, Air Force Cambridge Research Laboratories, L. G. Hanscom Field, Massachusetts (July 1962).

17. C. D. Rodgers and C. D. Walshaw, "The Computation of Infrared Cooling Rates in Planetary Atmospheres," Quart. J. Roy. Meteorol. Soc., Vol. 92, pp. 67-92 (1966).

18. B. H. Armstrong, "Theory of the Diffusivity Factor for Atmospheric Radiation," Report 320-3226, IBM Scientific Center, Palo Alto, California (January 1968).

19. W. Zdunkowski, D. Henderson, and J. V. Hales, "The Effect of Atmospheric Haze on Infrared Radiative Cooling Rates," J. Atmos. Sci., Vol. 23, pp. 297-304 (1966).

20. R. R. Sabatini and V. E. Suomi, "On the Possibility of Atmospheric Infrared Cooling Estimates from Satellite Observations," J. Atmos. Sci., Vol. 19, pp. 349-350 (1962).

21. K. J. Hanson, T. H. Vonder Haar, and V. E. Suomi, "Reflection of Sunlight to Space and Absorption by the Earth and Atmosphere over the United States During Spring 1962," Mon. Wea. Rev., 95, pp. 354-362 (1967).

22. P. A. Davis, "Satellite Radiation Measurements and the Atmospheric Heat Balance," Final Report, Contract NAS5-2919, Stanford Research Institute, Menlo Park, California (June 1964).

23. H. U. Roll, Physics of the Marine Atmosphere (Academic Press, New York and London, 1965, 426 pp.).